Fakultät für Medizin
Klinik für Herz- und Kreislauferkrankungen
Deutsches Herzzentrum München

und

Neurologische Klinik und Poliklinik
Klinikum der Universität München
Ludwig-Maximilians-Universität München

Intravital microscopy reveals complete regression of large, established CNS lymphoma after intracerebral CAR T cell injection

Matthias Mulazzani

Vollständiger Abdruck der von der Fakultät für Medizin der Technischen Universität München zur Erlangung des akademischen Grades eines

Doctor of Philosophy (Ph.D.)

genehmigten Dissertation.

Vorsitzende/r: Prof. Dr. Arthur Konnerth

Betreuer: Prof. Dr. Steffen Massberg

Prüfer der Dissertation:

1. Prof. Dr. Thomas Misgeld

2. Prof. Dr. Helmuth Adelsberger

Die Dissertation wurde am 10.07.2017 bei der Technischen Universität München eingereicht und durch die Fakultät für Medizin am 01.09.2017 angenommen.

Acknowledgements

Research always is a team effort. None of the work presented here would be finished without the numerous contributions, big and small, that these findings consist of and build upon.

First and foremost I would like to thank Louisa von Baumgarten for a multitude of things, including her unique support throughout the years. But a special thanks goes to her for providing me with the two most valuable things a researcher could think of: the trust and freedom necessary to independently develop ideas, as well as the structure and guidance necessary to follow through until the relevant questions are answered.

Another great deal of gratitude goes out to Steffen Massberg and all of his current and former lab members, who not only shared their time, equipment, and knowledge, but also their sometimes confined lab space, their motivation, the weekends at the lab and even their chocolate with me. Thank you.

Furthermore, I would like to particularly thank Sigrid Langer, Xiaolan Zhou, Andreas Straube, Dirk Busch, Simon Fräßle, Wenlong Zhang, Thomas Misgeld, Helmuth Adelsberger, Uwe Ködel, Michael Lorenz, Christian Schulz, Katrin Offe, Desislava Zlatanova, and all the other important contributors without whose help crucial pieces of this work would still be missing.

Also a huge “thank you” is owed to the whole Forschungshaus-crew, who reliably provided me with all the coffees, the laughs, and also the right perspective whenever needed, with whom I enjoyed all the ups and downs that graduate school brings about, and all the cakes or drinks whenever a celebration was due.

A special thanks also to the *crazy scientists*, my dearest fellows with whom I enjoyed so many evenings (and yet too few), and who always reminded me of the *balance* in work-life-balance and made sure it wouldn’t tilt too much one way or the other.

I gladly thank also my long-time friends for all their support and encouragement, be it for crossing the alps or the finish line of a PhD: once more you prove that with true friends, there really is no distance too far.

A big hug as well to my whole family for their endless love, trust, and encouragement, who although somewhat far away, yet fortunately always remain so close.

To mi cariño, who always understood the necessity for late-night-experiments and microscopy sessions, while providing me with more support than I ever could have asked for. Without you, I wouldn’t even be close to where I am today.

To all of you, I would like to express my deepest gratitude: this work would never have been possible without you.

Contents

1 Abstract

Chimeric antigen receptor T cells (CAR T cells) are a promising therapeutic approach to treat systemic malignancies. The most successful CAR targets CD19, a pan-B cell antigen present in most B cell malignancies, including primary CNS lymphoma (PCNSL). Whether anti-CD19 CAR T cells are able to control PCNSL growth is currently unknown.

In cancer therapy, better understanding of the cellular microenvironment and tumor development is of great interest. Currently, no animal model exists to repeatedly assess orthotopic PCNSL growth and possible anti-tumor effects of CAR T cell therapy *in vivo* at cellular resolution. To date, most studies have relied on immunohistochemical, bioluminescent or flow cytometry based analysis of single time points, precluding in-depth analysis of the exact intratumoral CAR T cell behavior, such as their interactions with tumor cells, their migratory patterns, proliferation and persistence. Additionally, intraindividual changes of these factors over time currently cannot be assessed.

To address these issues, we injected red fluorescent lymphoma cells and longitudinally visualized orthotopically growing PCNSL lymphoma *in vivo* using a chronic cranial window and two-photon microscopy. After establishment of a large intracortical tumor, green fluorescent anti-CD19 (h1928z) CAR T cells were stereotactically injected. Combining these methods, we were able to disentangle the essential steps for successful eradication of large, established intracranial lymphomas. This novel mouse model allows repeated, durable analysis of CAR T cell behavior at single-cell level, providing evidence that intracortical injection of h1928z CAR T cells successfully inhibits PCNSL growth *in situ*. Importantly, intratumoral infiltration, movement patterns, proliferation rates, CAR T cell persistence and tumor regression can be analyzed over the course of several weeks, providing valuable information about this highly successful novel therapy.

In light of recent successful clinical trials in the treatment of other B cell malignancies, including diffuse large B cell lymphoma, our preclinical data indicate that anti-CD19 CAR T cells warrant further investigation in the treatment of patients with refractory or relapsed PCNSL.

2 Introduction

2.1 Primary CNS lymphoma (PCNSL)

Primary central nervous system lymphoma (PCNSL) is a malignant brain tumor. It is a specific type of extranodal non-Hodgkin lymphoma (NHL), which manifests exclusively in the brain, spinal cord, leptomeninges or eyes without systemic affection. PCNSL currently comprises approximately 2-4% of all primary cerebral tumors (Villano et al. 2011; Ostrom et al. 2015). PCNSL affects males and females equally, and has an incidence of 0.4 per 100,000. The median age at presentation is between 50 and 60 years of age. The most important risk factor is immunodeficiency (Schabet 1999), illustrating the importance of the immune system in this disease. About 90-95% of PCNSL are of the diffuse large B cell lymphoma (DLBCL) subtype (Braaten et al. 2003; Rubenstein, Treseler, and O'Brien 2005), and hence express the B cell markers CD19 and CD20 (Cordone et al. 2016).

Symptoms at presentation depend mostly on the location of the lesion, including focal neurological deficits, neuropsychiatric symptoms, and signs of raised intracranial pressure (Bataille et al. 2000). In 24-78% of patients, unspecific symptoms such as behavioral changes predominate, complicating definite diagnosis and thereby protracting time to treatment (Herrlinger et al. 1999; Batchelor and Loeffler 2006). If untreated, patients succumb to this disease within a few months after diagnosis. Therefore, early diagnosis of PCNSL is crucial. Although on computer tomography (CT) and magnetic resonance (MR) imaging these lesions may have characteristic findings, none of these findings is pathognomonic for PCNSL. Histologic proof via stereotactic biopsy is warranted to firmly establish the diagnosis.

In immunocompetent patients, 62-66% of patients present with a singular intracerebral PCNSL lesion on initial MR imaging (Bataille et al. 2000; Buhring et al. 2001; Kuker et al. 2005). Due to its high cellularity and its accompanying blood-brain barrier disruption, most lesions show T1-weighted hypo- to isointense, T2-weighted iso- to hyperintense signal with restricted intratumoral water diffusion (hyperintense diffusion-weighted images (DWI) and low signal intensity in apparent diffusion coefficient (ADC) maps) and marked enhancement after intravenous (i.v.) application of contrast agent (Figure 1) (Haldorsen, Espeland, and Larsson 2011; Fitzsimmons, Upchurch, and Batchelor 2005). Often, these lesions are in direct contact with the subarachnoid space. For example, in one study evaluating 100 patients with biopsy-proven PCNSL, 95% had at least one lesion adjacent

to the subarachnoid space (Kuker et al. 2005). However, MRI often underestimates tumor burden, as diffuse tumor cell infiltration can often be found throughout the brain (Lai, Rosenblum, and DeAngelis 2002).

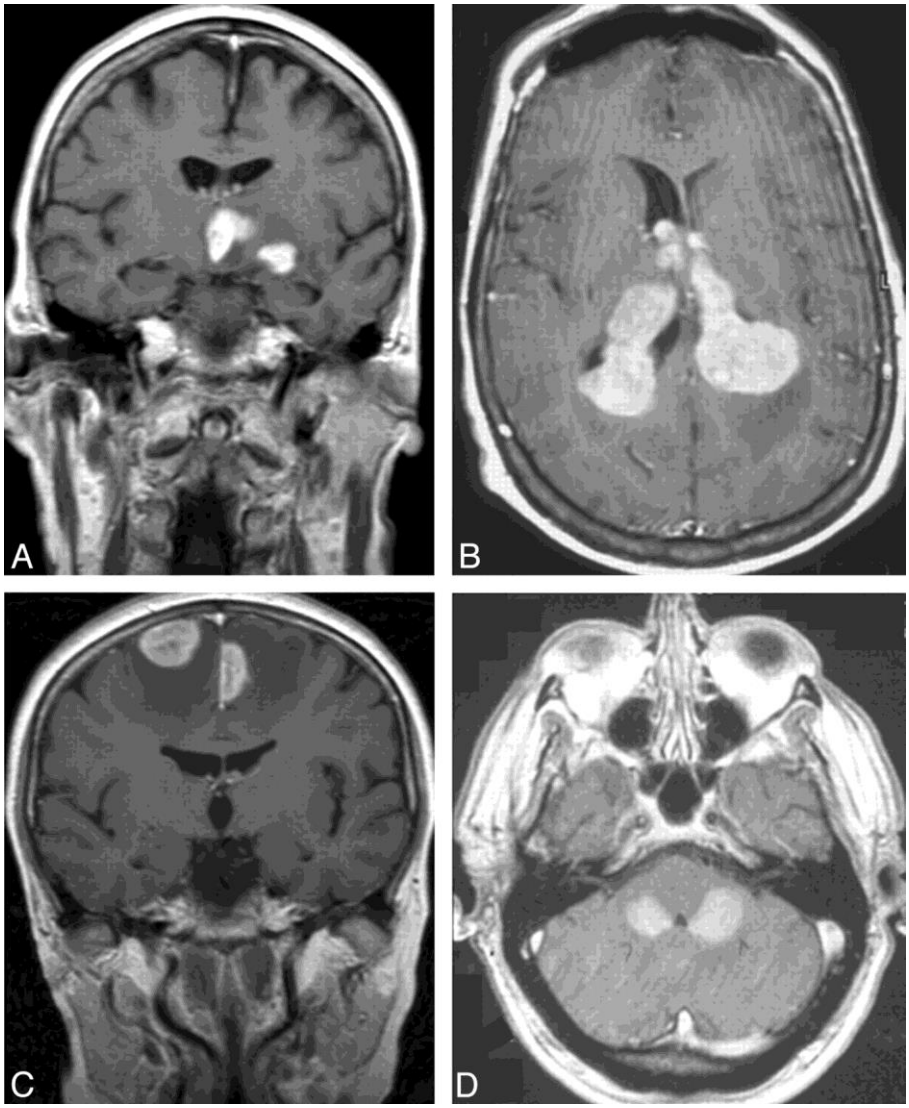

Figure 1 – Magnetic resonance images of PCNSL.
Coronal (**A**, **C**) and axial images (**B**, **D**) of 4 patients after administration of contrast agent reveal superficial or periventricular PCNSL. Lesions located in the basal ganglia (A), ventricles (B), frontal lobes (C), and cerebellum (D). Adapted from (Haldorsen, Espeland, and Larsson 2011).

Due to the low incidence of PNSL, randomized treatment trials are rare. Therefore, most treatment algorithms have been based on retrospective analyses and open label, single-arm trials. Generally, surgical resection is discouraged because of the infiltrative growth pattern. Accordingly, early trials showed no benefit for overall survival of patients after total or subtotal surgical PCNSL resection (DeAngelis et al. 1990; Bataille et al. 2000;

Bellinzona et al. 2005). Recently, this view has been challenged by one retrospective analysis of 526 patients, which resulted in improved progression-free and overall survival after total or subtotal resection compared to biopsy (Weller et al. 2012). However, after adjusting for lesion number, overall survival did not significantly differ. Therefore, surgical resection only provides limited benefit in PCNSL, and should only be considered for patients with easily accessible, single lesions with significant mass effect and low perioperative risks (Rubenstein, Gupta, et al. 2013; Korfel and Schlegel 2013; Fraser, Gruenberg, and Rubenstein 2015).

Initially, PCNSL was treated with radiotherapy alone. Although up to 90% of patients showed tumor regression after radiotherapy, relapses were inevitable and median overall survival ranged from 10 to 18 months (Jellinger, Radaskiewicz, and Slowik 1975; Sagerman, Collier, and King 1983; Murray, Kun, and Cox 1986). Therefore, combined radiochemotherapy including methotrexate was applied to increase tumor control, and median survival was increased to more than 30 months (DeAngelis et al. 1990; Ferreri et al. 2002; DeAngelis et al. 2002; Omuro, DeAngelis, et al. 2005). However, combined treatment led to severe neurotoxicity in up to 70% of patients with a mortality of up to 30% (Omuro, Ben-Porat, et al. 2005; Gavrilovic et al. 2006; Thiel et al. 2010). Furthermore, a randomized phase III trial showed that in patients treated with methotrexate-based polychemotherapy, additional radiotherapy does not result in a survival benefit (Thiel et al. 2010; Korfel et al. 2015). Nowadays, methotrexate has become the mainstay of current treatment algorithms. Although the 5-year survival rates increased considerably even outside clinical trials (from 19.1% in the 1990's to more than 30% in the 2000's) (Shiels et al. 2016), there is currently no international consensus regarding the optimal treatment regimen for individual PCNSL patients. Rituximab, a monoclonal anti-CD20 antibody, is usually added to current treatment regimens in patients with $CD20^+$ PCNSL (Batchelor et al. 2011; Fritsch et al. 2011; Birnbaum et al. 2012; Ferreri et al. 2016). Additionally, methotrexate is often combined with other agents able to cross the blood brain barrier, such as temozolomide (Rubenstein, Hsi, et al. 2013), procarbazine and vincristine (Shah et al. 2007; Morris et al. 2013), cytarabine (Ferreri et al. 2009), thiotepa (Soussain et al. 2012), or ifosfamid (Fischer et al. 2009).

For young and fit patients, intensification of therapy (consisting of high-dose, myeloablative chemotherapy followed by autologous hematopoietic stem cell transplantation (HSCT)) has resulted in 5-year survival of up to 79% of patients (Illerhaus et al. 2006; Kasenda et al. 2012; Schorb et al. 2013). However, this is associated with considerable treatment related toxicity (including a transplantation-associated mortality of 2.8%), and its efficacy remains to be confirmed in prospective, controlled clinical trials.

Despite aggressive therapy, up to 30% of patients do not respond to therapy, and more than 50% of patients relapse, the majority of them within the first two years after diagnosis (Nicolas-Virelizier et al. 2013). Close follow-up and monitoring is mandatory, screening for relapse as well as for treatment-associated, delayed CNS toxicity.

Therefore, new therapeutic strategies for this highly malignant disease are urgently needed.

2.2 Chimeric antigen receptor (CAR) T cells

The potential benefits of cancer immunotherapy have been observed even well before the specific components of the immune system have been characterized. Already more than 100 years ago, repeated injection of bacterial toxins into patients suffering from late stage sarcoma has led to tumor regressions (Coley 1898). Since then, knowledge about the interaction between the immune system and cancer has expanded dramatically. In 2013, cancer immunotherapy was chosen as *Science*'s breakthrough of the year (Couzin-Frankel 2013), and numerous encouraging results have emerged for several immunotherapeutic approaches, including immune checkpoint inhibitors (Page et al. 2014; Rizvi et al. 2015), adoptive cell therapy with autologous tumor-infiltrating lymphocytes (Dudley et al. 2013), and cancer vaccines (Walter et al. 2012). Similarly, treatment with therapeutic monoclonal antibodies against selected cancer cell surface antigens (CD20, CD52, ERBB2, EGFR) have led to survival benefit for patients with hematological malignancies and solid tumors alike (Scott, Wolchok, and Old 2012).

However, one of the most successful breakthroughs in cancer immunotherapy during the last decade has been the development of chimeric antigen receptor (CAR) T cells (Figure 2) (Maus et al. 2014; Yeku, Li, and Brentjens 2017; Fesnak, June, and Levine 2016; Sadelain, Brentjens, and Riviere 2013).

Chimeric antigen receptors are genetically engineered proteins that, once expressed, enable T cells to selectively target tumor-specific surface antigens independent of major histocompatibility complex (MHC) presentation. Tumor-specific antigen recognition via CAR leads to T cell activation, proliferation and tumor cell lysis, overcoming limitations of T cell receptor (TCR)-based adoptive cell therapy such as self-antigen tolerance and MHC downregulation.

CARs typically consist of two parts: an extracellular domain, usually an antibody-derived or ligand-derived domain specifically targeting a cell surface antigen, fused to an intracellular domain, responsible for T cell activation, proliferation and cytotoxicity. Kuwana and colleagues first reported the expression of antibody single-chain variable fragments (scFv) fused to intracellular signaling domains derived from the T cell receptor (TCR) (Kuwana et al. 1987). Soon thereafter, reports provided evidence that CAR expression leads to IL-2 secretion and cell lysis upon encounter of the target-specific antigen *in vitro* (Eshhar et al. 1993). *In vivo*, these CAR T cells have shown some therapeutic success in controlling tumor xenografts (Hwu et al. 1995). However, anti-tumor responses of these “first-generation” CAR T cells were limited, as T cell activation signaling through the CD3ζ chain alone was not enough to activate resting T cells (Brocker and Karjalainen 1995). Furthermore, repeated exposure to antigen led to a condition called T cell anergy, during which T cells fail to elicit a robust cytokine response (Gong et al. 1999).

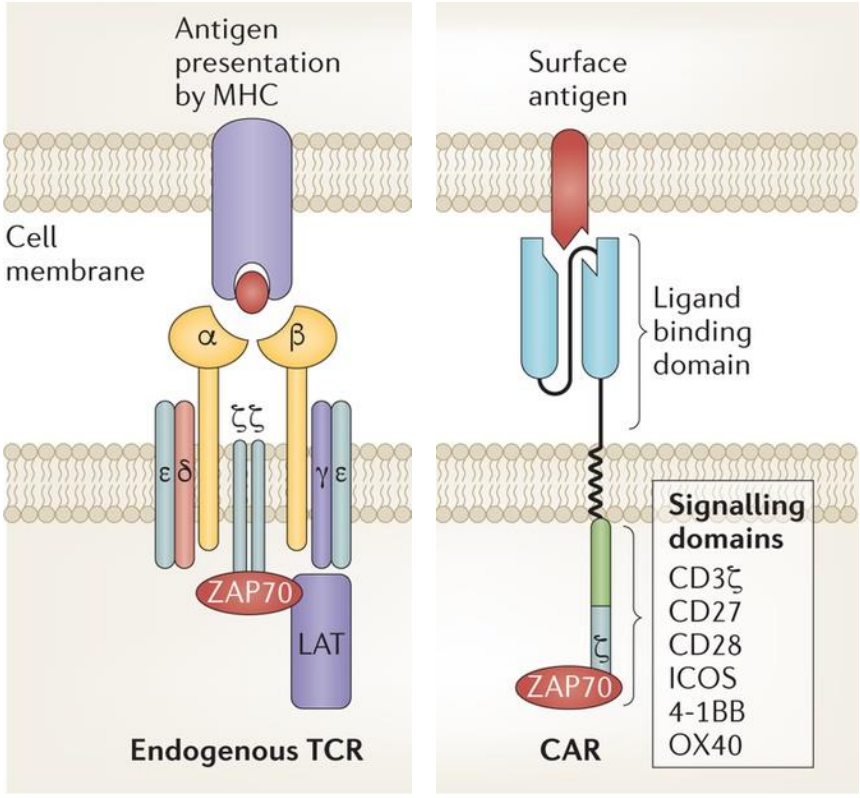

Figure 2 – Illustration of the T cell receptor (TCR) and the chimeric antigen receptor (CAR).
The TCR is dependent on antigen presentation of intracellularly processed antigens, presented on major histocompatibility complexes (MHC). In cancer, tumor cells frequently downregulate MHC expression as an immune escape mechanism. The CAR’s extracellular ligand binding domain often consists of single-chain variable fragments derived from immunoglobulin domains. Thereby, CAR activation is independent of major histocompatibility complex (MHC) presentation. Via connection by a hinge and a transmembrane domain, these extracellular domains are fused to an intracellular CD3ζ chain domain. In second-generation CAR T cells, this intracellular domain is combined with a second, costimulatory signalling domain. Adapted from (Fesnak, June, and Levine 2016).

Addition of a second costimulatory signaling domain, CD28, helped overcome T cell anergy, as T cells expressing these (eventually termed “second-generation”) CARs were able to retain their cytolytic properties after repeated antigen exposure for a duration of several weeks (Maher et al. 2002).

Since then, several costimulatory domains have been evaluated (including CD27, CD28, OX40, ICOS, 4-1BB), and their superiority compared to first-generation CAR T cells has been verified in several preclinical trials (Maher et al. 2002; Brentjens et al. 2007). Taken together, costimulatory signaling of this second-generation CAR design substantially increases CAR T cell expansion, tumor infiltration, and persistence in these mouse models.

The enormous potential of CAR T cells has also been proven in numerous clinical trials against therapy refractory cancers. Its most successful example to date is the anti-CD19 CAR, targeting CD19-positive B cell malignancies (Porter et al. 2011; Kochenderfer et al. 2012; Brentjens et al. 2013; Grupp et al. 2013; Davila et al. 2014; Lee et al. 2015; Savoldo et al. 2011). For example, in one of these trials, 5 of 5 patients with relapsed or refractory acute lymphoblastic leukemia (ALL) achieved complete remission after injection of second-generation 19-28z CAR T cells. These results have later been corroborated in another trial, where 14 of 16 patients with relapsed or refractory ALL achieved complete remission (Davila et al. 2014). Similarly astonishing results, albeit at lower rates of complete remission, have been shown for diffuse large B cell lymphoma (DLBCL), a solid $CD19^+$ tumor (Kochenderfer et al. 2015). Several factors have been hypothesized for the limited success of CAR T cell therapy in solid tumors compared to their semiliquid hematological counterparts, including physical barriers, a hostile tumor microenvironment (depleted of oxygen and nutrients, with lower pH and high levels of oxidative stress) and immunosuppressive cytokines and immune cells (Newick et al. 2017; Yong et al. 2017). However, the exact infiltration patterns of CAR T cells in solid tumors have never been analyzed in detail.

Even in patients after allogeneic hematopoietic stem-cell transplantation, allogeneic CAR T cells have successfully been generated and used in patients suffering from progressive $CD19^+$ relapses – importantly, without the development of graft-versus-host disease, a potentially fatal side effect of allogeneic cell transplantation (Brudno et al. 2016).

In spite of these magnificent clinical successes of CAR T cells in systemic, therapy-refractory B cell malignancies, the effect of CAR T cell therapy has never been evaluated for $CD19^+$ PCNSL, neither in humans nor in preclinical animal models.

Furthermore, many important questions regarding CAR T cell biology remain unanswered, especially in immune privileged organs like the brain (Engelhardt, Vajkoczy, and Weller 2017). Until now, most preclinical data on tumor infiltration patterns, local proliferation, and intratumoral migration of CAR T cells are based on flow cytometry, bioluminescence signals, autopsy studies and *in vitro* experiments (Santos et al. 2009; Bai et al. 2015; Kochenderfer et al. 2010; Roybal et al. 2016), and not able to repeatedly visualize cerebral CAR T cell behavior in detail. Therefore, how these important cell patterns change over time is not yet completely understood. Similarly, current data does not offer conclusive answers about long-term *in situ* persistence, especially regarding the spatial (i.e. which compartment) and temporal (i.e. the maximum duration) characteristics of intracerebral CAR T cell persistence.

2.3 Two-photon laser scanning microscopy (TPLSM)

For several decades, researchers have sought to understand the exact cellular interactions of immune cells with tumor cells. One particular technology, *in vivo* fluorescence microscopy, has revolutionized our understanding of these complex interactions.

When fluorophores absorb enough energy via electromagnetic radiation (“excitation“ light), these fluorophores are thereby excited to a higher singlet energy state. After internal conversion, most fluorophores are relaxed to the lowest excited singlet state. Upon relaxation from this excited singlet state, these excited fluorophores are able to emit light, usually at a longer wavelength than the absorbed light. Detection of this emitted light (“emission“ light) can be used to locate fluorescently labelled structures like cells, organelles, or macromolecules in space and time, conferring information about their position and behavior.

In conventional wide-field fluorescence microscopy, the wavelength of excitation light is lower than the wavelength of emission light. As the energy of light is inversely proportionate to its wavelength (c / λ), photons at lower wavelengths transmit more energy. Hence, long and intense application of low wavelength / high energy light can lead to the production of reactive oxygen species (ROS) (Dixit and Cyr 2003). ROS can react with a range of oxidizable components, including proteins, lipids, nucleic acids and fluorophores. This can damage biological samples, a process called phototoxicity, or lead to loss of fluorescence signal, called photobleaching. Apart from phototoxicity and

photobleaching, light scattering prevents image acquisition through thick layers of biological specimens. Light at wavelengths in the visible spectrum (corresponding to electromagnetic radiation at a wavelength of approximately 400 – 700 nm) results in high scattering in these tissues, leading to lower signal-to-background ratio and hence lower image quality. Therefore, wide-field fluorescence microscopy of biological samples is mostly restricted to thin or superficial structures, due to phototoxicity, photobleaching and high scattering. Additionally, wide-field fluorescence microscopy is limited by its low axial resolution (i.e., the ability to distinguish detail in the z-dimension) due to background noise above and below the focal plane, thus inhibiting three-dimensional reconstruction in high quality.

In contrast, two-photon laser scanning microscopy (TPLSM) uses excitation light at a wavelength approximately twice the wavelength used by single-photon fluorescence microscopy (usually in the near-infrared range, at approximately 700 – 1200 nm). Photons at higher wavelengths carry less energy than photons emitted at a lower wavelength. Hence, to successfully excite fluorophores commonly used in fluorescence microscopy, the absorption of two photons at the exact same time (in the range of a few femtoseconds, i.e. $^{1}/_{1,000,000,000,000,000}$ of seconds) is necessary. Therefore, excitation light needs a density of photons high enough to excite these fluorophores. This is only possible with the use of high powered mode-locked lasers with a pulse width of usually less than <100fs, temporally concentrating photons at an extremely high density.

In a laser scanning microscope, excitation is furthermore limited to the focal point of a diffraction-limited microscope (e.g. exciting only a fraction of a μm^3). Rapidly moving mirrors connected to a microscope can raster-scan a specimen in a focal plane (Figure 3). Organs like the brain can then be scanned sequentially at imaging depths of up to 1 mm beneath the surface, creating high-resolution three-dimensional images, limiting light pulses (as well as adverse effects like photobleaching and phototoxicity) to just one focal plane. TPLSM is combining these advantages with high-wavelength inherent reduction of tissue absorption and scattering. Therefore, it is often the method of choice for fluorescence microscopy of thick biological samples, including living tissues (Helmchen and Denk 2005; Kobat et al. 2009; Horton et al. 2013; Denk, Strickler, and Webb 1990; Misgeld and Kerschensteiner 2006).

Since its inception, this technique has been used to disentangle many aspects of immune cell interaction with cancer cells *in vivo* (Ellenbroek and van Rheenen 2014; Zal and Chodaczek 2010; Ramamonjisoa and Ackerstaff 2017; Torcellan, Stolp, and Chtanova 2017; Breart et al. 2008; Deguine et al. 2010).

Most of these studies have relied on *in vivo* microscopy at single time points, as experimental setups seldom allow for repeated imaging of the same position. However, several groups have shown that repeated, intravital microscopy through a chronic cranial window is possible in individual mice over time, enabling repeated visualization of biological processes during a time frame of several weeks to months (Kienast et al. 2010; von Baumgarten et al. 2011; Osswald et al. 2015). Specifically in neuro-oncological research, this method has enabled researchers to analyze many important aspects of intracranial cell migration, metastasis formation, tumor growth patterns, and therapeutic effects of several CNS malignancies in detail.

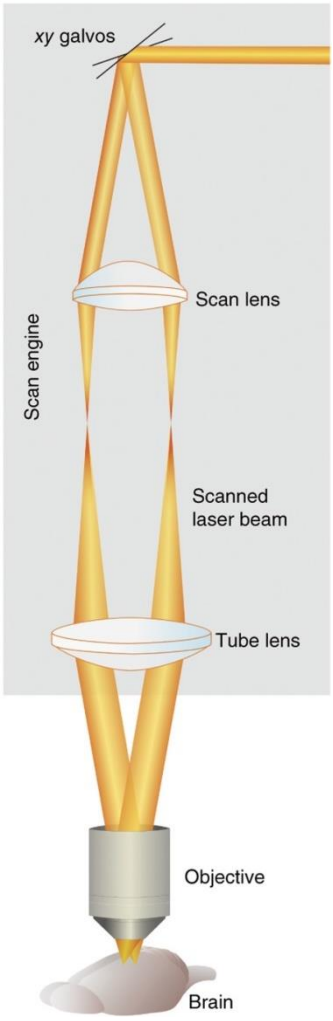

Figure 3 – Illustration of a TPLSM.
Adapted from (Ji, Freeman, and Smith 2016)

2.4 Aims of this thesis

Despite the magnificent preclinical and clinical results in B cell malignancies, the therapeutic efficacy of anti-CD19 CAR T cells has never been evaluated for their effect in PCNSL, a highly malignant, $CD19^+$ CNS tumor with poor prognosis. Besides, many important aspects of CAR T cell biology remain unclear, including tumor infiltration patterns, intratumoral and intracerebral motility, CAR T cell behavior after tumor regression, and long-term persistence in the brain.

Therefore, the objectives of this thesis were:

- to create a novel animal model of PCNSL,
- to combine this animal model with a chronic cranial window and repeated TPLSM to follow *in vivo* development of orthotopic PCNSL growth,
- to evaluate the effect of activated, second-generation anti-CD19 CAR T cells on PCNSL, and
- to answer essential questions of intracerebral CAR T cell biology, including tumor infiltration patterns, migration, proliferation and long-term persistence, evaluating changes over time.

3 Materials and methods

3.1 Cell culture

OCI-LY10, OCI-LY3, U-2932, three human diffuse large B cell lymphoma (DLBCL) cell lines, as well as the human Burkitt lymphoma cell line Raji, were kindly provided by Prof. Dreyling (LMU Munich, Germany). HKBML, a cell line generated from a human primary CNS lymphoma, was purchased from RIKEN BioResource Center (Tsukuba, Japan). OCI-LY3 and OCI-LY10 cells were cultured in Iscove's Modified Dulbecco's medium (IMDM, Life Technologies, Darmstadt, Germany) supplemented with 20% human plasma, 0.4% heparin (Ratiopharm, Ulm, Germany) and 0.1% beta-mercaptoethanol (Sigma-Aldrich, Missouri, USA). HKBML cells were cultured in Ham's F12 Nutrient Mixture (Life Technologies, Darmstadt, Germany) supplemented with 15% fetal bovine serum (FBS, from Biochrom GmbH, Berlin, Germany and Thermo Fisher Scientific, Wilmington, USA). U-2932 and Raji cells were cultured in RPMI (Life Technologies) supplemented with 10% FBS. All cells were regularly tested for mycoplasma infection using the PCR Mycoplasma Test Kit (PanReac AppliChem GmbH, Darmstadt, Germany). To keep genetic drift to a minimum, cells were maintained in culture for a maximum duration of 2-3 months before replacing them.

3.2 Bacterial plasmid replication

For plasmid replication, *XL2-Blue Ultracompetent* cells (Stratagene, La Jolla, USA) were used, kindly provided by Prof. Dreyling (LMU Munich, Germany). These bacteria were chosen because of their high transformation efficiency. Their exact genotype is *endA1 supE44 thi-1 hsdR17 recA1 gyrA96 relA1 lac* [F´ *proAB lacI*^{q}*ZΔM15 Tn10* (Tet^{r}) Amy Cam^{r}] (the listed alleles represent the mutant alleles increasing transformation efficiency, plasmid yield, and stability of the cloned plasmid).

To manufacture $CaCl_2$ competent bacteria, the XL2-Blue cells were grown in 10 ml of lysogeny broth (LB) medium overnight at 37°C at a platform shaker with 130 rpm. On day two, 1ml of bacteria suspension was added to 100 ml of LB medium (100 ml double deionized water, 2.5 g LB (Carl Roth GmbH, Karlsruhe, Germany)) at 37°C with 130 rpm,

until the optical density at a wavelength of 600 nm (OD600) reached 0.7 - 0.8 (approximately after 2.5-4 h). Immediately afterwards, the liquid was cooled on ice for 30 minutes. Then, the liquid was centrifuged in 2 Falcon tubes (50 ml) for 15 minutes at 4°C with 4500 rpm. Next, the pellets were resuspended with 25 ml of 0.1M $CaCl_2$ solution (freshly prepared at 4°C). After another 30 minutes on ice, the solutions were centrifuged for 15 minutes at 4°C with 4500 rpm. The resulting pellets were resuspended in 2.5 ml 0.1M $CaCl_2$/10% glycerol solution (freshly prepared at 4°C). This solution was portioned to 100 µl aliquots and shock frozen in liquid nitrogen. Afterwards, these aliquots were stored at -80°C.

To transform these $CaCl_2$ competent bacteria, an aliquot was thawed on ice and split into two aliquots with 50 µl. To each of these samples, 1-100 ng of plasmid was added. Next, the samples were incubated on ice for 30 minutes. Afterwards, they were exposed to 1 minute of *heat-shock* at 42°C. Subsequently, they were returned to ice for 3 minutes. Then, 500 µl of LB medium were added. After one hour of shaking at 37°C (130 rpm), 100-200 µl of each sample was plated onto LB-*Amp* agar plates (100 ml double deionized water, 2.5 g LB, 1.5 g agar (Sigma-Aldrich, St. Louis, USA), and ampicillin (Ratiopharm) at a target concentration of 100 µg/ml). Next, they were grown overnight at 37°C (5% CO_2). The next day, single colonies were isolated and inoculated into 5 ml of LB-*Amp* medium each (LB medium with ampicillin at a target concentration of 100 µg/ml). These solutions were shaken at 37°C for 8 hours. One of these was selected, 500 µl of it were added to 250 ml of LB-*Amp* medium and shaken at 37°C overnight (250 rpm) before plasmid isolation.

3.3 Plasmid isolation

Isolation of plasmid DNA was performed according to the manufacturer's instructions of the Qiagen MaxiKit (Qiagen, Hilden, Germany). Briefly, the cells were lysed with an alkaline solution, genomic DNA and proteins were precipitated, and the remaining plasmid DNA was further purified and isolated. To determine purity and yield, a spectrophotometer was used according to the manufacturer's instructions (Nanodrop 2000, Thermo Fisher Scientific) (Desjardins and Conklin 2010). To determine DNA purity, the ratio of absorbance at wavelengths of 260 nm and 280 nm was measured ($A_{260/280}$). A ratio of more than 1.8 was considered pure, a ratio of less than 1.8 was considered to indicate protein contamination. After calibration of the instrument, the quantity of DNA was

measured based on the Lambert-Beer law by absorbance at 260 nm. Plasmid samples were stored in TE buffer at -80°C until further use.

3.4 TdTomato Vector

Genetically engineered cells tend to downregulate transgene expression over time, often facilitated via epigenetic silencing of the transgene promoter (Kaufman et al. 2008). This mechanism can lead to mosaic expression and/or reduced fluorescence, hindering efficient tumor cell visualization. To inhibit epigenetic silencing, thereby generating stable fluorescent cells, we created a vector expressing both the resistance protein and the fluorescent protein under the control of the same promoter. Therefore, we made use of the internal ribosome entry site (IRES), first described by Pelletier and Sonenberg (Pelletier and Sonenberg 1988). This noncoding RNA element, originally found in eukaryotic viruses, allows for translation of two different proteins from the same mRNA. Translation of these mRNAs occurs at the 5' end of the mRNA as well as at the IRES, thereby enabling initiation of translation of two proteins from the same mRNA. However, expression of the downstream protein occurs at significantly lower numbers compared to the upstream protein, as translation initiation mid-mRNA is generally less efficient (Mizuguchi et al. 2000). Thus, placing the neomycin resistance protein downstream of the IRES, the ratio of fluorescent protein to neomycin resistance protein is expected to be shifted towards the fluorescent protein, enhancing imaging quality.

Therefore, we combined tdTomato with an IRES linked to neomycine resistance: To this aim, a PCR product containing the coding sequence of tdTomato (vector ptdTomato, catalog No. 632531, TaKaRa Clontech, Mountain View, USA) was cloned into the lentiviral expression vector pLVX-IRES-neoR (content of the Lenti X Bicistronic Expression System, Catalog No. 632181, TaKaRa Clontech). The resulting construct pLVX-tdTomato-IRES-Neo (Figure 4) was verified by restriction enzyme digest and by direct sequencing.

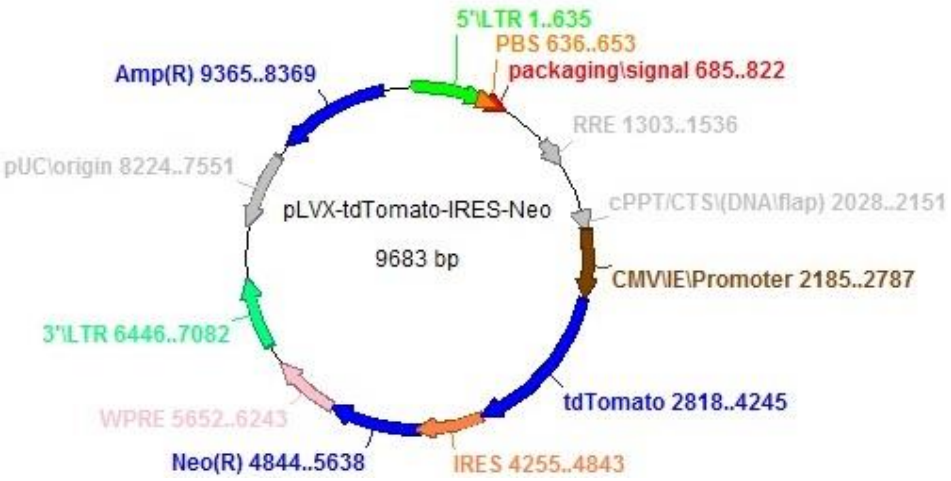

Figure 4 – pLVX-tdTomato-IRES-Neo^r plasmid.

3.5 Electroporation

To stably transfect tumor cells, the pLVX-tdTomato-IRES-Neo vector was electroporated into U-2932 or OCI-LY10 cells. Briefly, 20 µg of supercoiled vector in TE buffer was added to 3x10^7 lymphoma cells in 500 µl of respective cell medium and the solution was gently mixed. Electroporation was performed using the Gene Pulser Xcell system (Bio-Rad Laboratories, Hercules, USA) with 200 V, 1200 µF, unlimited resistance and exponential decay. Immediately after electroporation, cells were carefully resuspended in pre-warmed CO_2-equilibrated medium (37°C). 24 hours after electroporation, G418 was added at the appropriate concentration, determined beforehand in G418 cytotoxicity assays (800 µg/ml for U-2932, 600 µg/ml for OCI-LY10, 400 µg/ml for HKBML and OCI-LY3).

3.6 Fluorescence-activated cell sorting (FACS)

Selection of fluorescent cells by antibiotic selection often leads to variable transgene expression. To achieve homogeneous and intense expression of tdTomato, cell sorting is more reliable than antibiotic selection alone (Kaufman et al. 2008).

Flow cytometry and cell sorting was performed on a MoFlo Astrios Cell Sorter (Beckman Coulter, Munich, Germany). Briefly, single cell suspensions of lymphoma cells were measured for tdTomato expression by flow cytometry. 1-5% of the cells with the highest

level of tdTomato expression were sorted and cultured for approximately two weeks until sufficient cell numbers were attained. This process was repeated until tdTomato expression was high enough for TPLSM. Cells with sufficient levels of tdTomato expression were frozen in culture medium with 10% DMSO (v/v) and kept at -80°C until use.

3.7 CAR vectors

CAR vector cloning and CAR T cell generation were conducted at the TUM (Munich, Germany) in cooperation with Simon Fräßle and Dirk Busch (Institute for Medical Microbiology, Immunology and Hygiene, TUM, Munich, Germany). For the *in vitro* LDH assay, the second-generation anti-murine CD19 CAR vector m1928z was used as described (Paszkiewicz et al. 2016). For *in vivo* experiments, the second-generation murine m1928z CAR vector was modified to contain a murine anti-**h**uman CD**19** single chain variable fragment (scFv, derived from clone FMC63 (Nicholson et al. 1997)), fused via CD8 derived extracellular domain and transmembrane domain to the intracellular CD**28** costimulatory domain and the CD3**ζ** signaling domain into the retroviral pMP71 vector. By a P2A linker, this gene construct is connected to a truncated, functionally inert version of the epidermal growth factor receptor (EGFRt) (Wang et al. 2011), resulting in the **h1928z** vector (Figure 5).

Figure 5 – Vectors for h1928z CAR (A) and mock CAR (B) transduction.
(**A**) The anti-human CD19 scFv is fused to the CD8 derived hinge and transmembrane domains, the CD28 costimulatory domain and the CD3ζ intracellular signaling domain. For cell isolation and assessment of transduction efficacy, the truncated, inert version of the epidermal growth factor receptor is added. (**B**) The mock CAR transduction vector has no extracellular domain (scFv), thereby serving as the control group for *in vivo* experiments to exclude spontaneous CAR activation.

For eGFP transfection, the pMP71 retroviral vector containing the sequence for eGFP (Engels et al. 2003) was used, kindly provided by Stanley Riddell, Fred Hutchinson Cancer Research Center (Wang et al. 2011).

3.8 Retroviral T cell transduction

Primary NMRI Foxn1 nu/+ T cells or beta-actin-eGFP T cells were isolated and transduced as described (Paszkiewicz et al. 2016).

Briefly, two days before T cell transduction, the retroviral packaging cell line Platinum-E (PlatE, Cell Biolabs, San Diego, USA) was plated out at a density of $5x10^5$ cells per 6-well plate and cultivated overnight in cDMEM medium (*complete* DMEM (Gibco, Waltham, USA), containing 10% (v/v) FCS, 0.025% (w/v) L-glutamine, 0.1% (w/v) HEPES, 0.001% (w/v) gentamicin, 0.002% (w/v) streptomycin). On the next day, PlatE cells were transfected using calcium chloride precipitation. Briefly, 18 µg of purified DNA (in ddH_2O) was mixed with 15 µl $CaCl_2$ (2.5 M), and diluted in sterile ddH_2O to a total volume of 150 µl. 150 µl of 2x HBSS buffer (pH 6.74) were added and the resulting solution incubated at room temperature for 30 min to form DNA precipitates. The precipitates were added to the PlatE cells and incubated for 6h at 37°C, 5% CO_2, followed by medium replacement with cDMEM. The supernatant containing the retroviral particles was collected 48 h and 72 h after CaCl2 addition, filtered through a 0.45µm filter and either directly used or stored at -80°C for transduction of primary mouse T cells.

Murine splenocytes were isolated from spleens of beta-actin eGFP mice (allogeneic) or heterozygous NMRI $Foxn1^{nu/+}$ mice (syngeneic). Spleens were dissected, minced and filtered through a 70 µm cell strainer into a single cell solution. After centrifugation, ammonium chloride-Tris (ACT) buffer (0.17 M NH_4Cl, and 0.17 Tris-HCl, pH 7.5, mixed at a ratio of 9:1) was added for erythrocyte lysis. Remaining splenocytes were cultured in cRPMI (*complete* RPMI 1640 (Gibco), containing 10% FCS (v/v), 0.025% L-glutamine (w/v), 0.1% HEPES (w/v), 0.001% gentamicin (w/v), 0.002% streptomycin (w/v)), supplemented with 25 U/ml of IL-2 (Proleukin, Novartis, Basel, Switzerland) and stimulated overnight with anti-mouse CD3 antibodies (1:1000, clone 145-2C11, BD Pharmingen, San Diego, USA) and anti-mouse CD28 antibodies (1:5,000, clone 37.51, BD Pharmingen).

One day before transduction, 24-well plates were coated with retronectin (1:160, Takara Clontech), anti-mouse CD3 (1:1000) and anti-mouse CD28 (1:5000) in sterile PBS (Sigma

Aldrich) by addition of 300 µl per well and centrifugation at 2000 g, 32°C for 90 minutes. On the day of transduction, 500 µl of virus (h1928z CAR, m2918z CAR or mock CAR, together with the eGFP vector) were added per well, and the 24-well plates were centrifuged at 3000 g, 32°C for 2 hours. Virus-containing supernatant was removed and the murine splenocytes were resuspended in cRPMI supplemented with 25 U/ml of IL-2, counted and seeded into the virus-coated 24-wells at a concentration of $5x10^5$ cells/ml. Cells were transduced during centrifugation (800 g, 32°C) for 90 minutes. After transduction, cells were expanded for 48 h (37°C, 5% CO_2). Transduced T cells were sorted using a MoFlo Astrios Cell Sorter (Beckman Coulter) or FACSAria (BD Biosciences, San Jose, USA). Cells were sorted on double positivity (eGFP and EGFRt positivity, by addition of biotinylated cetuximab, kindly provided by Stanley Riddell, Fred Hutchinson Cancer Research Center (Wang et al. 2011), and streptavidin-APC) after excluding $CD19^+$ B cells (aCD19mAB, clone 1D3, PECF594, BD Pharmingen) and dead cells (propidium iodide, Invitrogen).

3.9 Cytotoxicity assay

To determine cell-mediated cytotoxicity, a Lactate dehydrogenase (LDH)-based cytotoxicity assay was performed. LDH is an enzyme present in all eukaryotic cells. Cell damage releases LDH into the surrounding supernatant (Legrand et al. 1992). Quantitative measurement of this enzyme's activity enables calculation of the number of lysed cells.

To assess the level of CD19-specific CAR-mediated cytotoxicity on human lymphoma cells, we co-cultured 7,500 OCI-LY10tdt cells with serial dilutions of murine anti-human CD19 CAR T cells, or murine anti-mouse CD19 CAR T cells as controls in 96 well V-bottom plates in triplicate. LDH assay was performed according to the manufacturer's instructions of the *Cytotox 96 Non-Radioactive Cytotoxicity Assay* (Promega, Madison, Wisconsin, USA). Briefly, after 4 hours of co-incubation in a humidified chamber at 37°C with 5% CO_2, the 96 well plate was centrifuged at 250 g for 4 minutes. 50 µl aliquots of supernatants were transferred to a fresh 96-well flat-bottom plate. 50 µl of *Cytotox 96 Reagent* were added to each well. The plate was protected from light and incubated for 30 minutes at room temperature. 50 µl of *Stop Solution* were added to each well, and absorbance of each well was measured at a wavelength of 490 nm using a microplate reader (Victor X3, Perkin Elmer, Waltham, USA).

Tumor cell control (OCI-LY10tdt cells only, $LDH_{target\ spontaneous}$), CAR T cell control (CAR T cells only, $LDH_{effector\ spontaneous}$), and maximum LDH release control (OCI-LY10tdt cells treated with *Lysis Solution*, $LDH_{maximum}$), were measured. From all values, no-cell control (culture medium background, LDH_{medium}, normalized to volume) values were subtracted. Cytotoxicity was calculated as follows:

$$\% \text{ Cytotoxicity} = LDH_{sample} - LDH_{effector\ spontaneous} - LDH_{target\ spontaneous} / LDH_{maximum} \times 100$$

3.10 Mice

All animal experiments were conducted in accordance with the animal welfare act and the Bavarian state regulations for animal experimentation. Protocols were approved by the state authorities (Regierung von Oberbayern, Munich, Germany).

NMRI $Foxn1^{nu/nu}$ mice are an outbred albino mouse strain harboring a mutation in the *Foxn1* gene, a transcription factor necessary for the development and function of epithelial cells in the thymus, skin, hair and nails. In homozygotes ($Foxn1^{nu/nu}$), this mutation leads to universal alopecia (hence the term “nude” mice) (Flanagan 1966) and absence of thymus (Pantelouris 1968), the primary organ of T cell development. Similarly to human patients harboring a mutation in *FOXN1* first described thirty years later (Frank et al. 1999), these mice are devoid of functional T cells (Zuklys et al. 2016). As xenografts of human cancer cells are not rejected in these mice (Fogh, Fogh, and Orfeo 1977), $Foxn1^{nu/nu}$ mice are often used in preclinical cancer xenograft models. Still, nude mice retain complement function and have robust B cell and NK cell responses. Due to the outbred background, NMRI $Foxn1^{nu/nu}$ mice may show higher variation in tumor growth compared to inbred mice. However, they are more robust and therefore more likely to sustain invasive experimental procedures than inbred mice.

$Foxn1^{nu/+}$ mice, heterozygous for the Foxn1 mutation, express reduced mRNA levels of *Foxn1* (Zuklys et al. 2016), and show a partially rescued phenotype with normal hair growth and a functional thymus, albeit at a reduced size compared to wildtype mice (Holub 1992; Scheiff, Cordier, and Haumont 1978). However, functional T cells develop in heterozygous $Foxn1^{nu/+}$ mice (Hunig and Bevan 1980).

C57BL/6J Beta-actin-eGFP mice are expressing “enhanced” GFP (eGFP, a mutated version of GFP with 35 times brighter fluorescence compared to wildtype GFP, (Zhang, Gurtu, and Kain 1996)) under the control of a chicken beta-actin promotor (Okabe et al.

1997). Except hair and erythrocytes, all cells thereby stably express intracellular eGFP, enabling fluorescence microscopy of these cells.

NMRI Foxn1$^{nu/nu}$ mice, NMRI Foxn1$^{nu/+}$ mice, C57BL/6J beta-actin-eGFP mice and C57BL/6J wild-type mice were purchased from The Jackson Laboratory via their distributor, Charles River Germany (Sulzfeld, Germany), and maintained at our facility according to Federation of European Laboratory Animal Associations (FELASA) guidelines. Experiments were started at the age of 8-14 weeks. For experiments with cranial window implantation or T cell injection, only male mice were used.

3.11 Anesthesia and postoperative care

For surgical procedures, mice were anesthetized by intraperitoneal (i.p.) injection of MMF (a combination of medetomidine (0.5 mg/kg, Ratiopharm), midazolam (5 mg/kg, Pfizer, Karlsruhe, Germany) and fentanyl (0.05 mg/kg, CuraMed Pharma GmbH, Karlsruhe, Germany) mixed in 0.9% sodium chloride solution (Fresenius Kabi Deutschland, Bad Homburg, Germany)), leading to safe and reliable anesthesia, sedation and relaxation. After injection, mice were returned to their home cages until they became motionless, usually within 10 minutes after injection, followed by application of eye ointment. During surgery, depth of anesthesia was regularly monitored by testing the pedal withdrawal reflex and by verifying respiratory frequency. 30 minutes before the end of the surgery, 0.1mg/kg buprenorphine (Essex Pharma, Munich, Germany) was administered subcutaneously (s.c.). After completion of the surgery, anesthesia was antagonized with s.c. injection of atipamezole (0.75 mg/kg, Pfizer), flumazenil (0.2 mg/kg, Roche, Basel, Switzerland) and naloxone (0.12mg/kg, Delta-Select, Dreiech, Germany), and mice were kept on a heating mat until fully awake. Postoperative analgesia was maintained by regular s.c. injections of buprenorphine every 8 hours for three days (after cranial window implantation or tumor implantation) or one day (after stereotactic T cell injection). After surgeries, mice were inspected and evaluated for development of symptoms at least three times per week using a standardized test for neurological symptoms considering body weight, spontaneous movement, reaction to blunt touch, and balance testing. Mice were euthanized if predefined symptoms occurred or weight loss exceeded more than 20%.

3.12 Chronic cranial window implantation

Implantation of a chronic cranial window was performed as previously described (Kienast et al. 2010; von Baumgarten et al. 2011). Briefly, after induction of a sufficient level of anesthesia, mice were immobilized in a stereotactic frame (David Kopf Instruments, Tujunga, USA) on a heating mat. Cefotaxime (250 mg/kg, Fresenius Kabi Deutschland, Bad Homburg, Germany) and dexamethasone (2mg/kg, Ratiopharm) were s.c. injected. Disinfection of the cranial skin was performed using povidone-iodine solution (Braunol, B. Braun Melsungen AG). Subsequently, a small incision along the sagittal suture was made. After removal of the skin and the epicranial aponeurosis, a circular part of the cranium with a diameter of 5,5mm was carefully drilled away using a dental drill equipped with a sterile carbon steel micro drill (tip diameter: 0.5mm, Fine Science Tools Germany, Heidelberg, Germany) under constant saline flush to prevent heat damage to underlying structures. Thereafter, the circular bone was cautiously removed while separating the endosteal layer of the dura mater from the bone using a blunt forceps to preclude injury of the sagittal sinus. If vessels were damaged, bleeding was stopped by short application of sterile sponges coated with fibrinogen and thrombin (TachoSil, Takeda Austria, Linz, Austria). The brain surface was constantly kept moist using 0.9% saline chloride solution. To inhibit late dural fibrosis from restricting microscopy quality, the meningeal layer of the dura mater was separated from the leptomeninges and removed (except in the region demarcating the sagittal sinus). After removal of the dura, the bone surrounding the opening was completely dried using sterile absorbent swabs (Sugi Eyespear, Kettenbach GmbH, Eschenburg, Germany) while the brain surface remained soaked with saline chloride solution. An autoclaved round cover glass with a diameter of 6mm was placed on top. Any incidental air bubbles were carefully removed using saline chloride solution. The outer rim of the cover slip was attached to the dry bone by circular application of a mixture of liquid ethylcyanoacrylate with methylacrylate powder (Cyano veneer, Hager Werken, Duisburg, Germany). While the cyanoacrylate glue was still semiliquid, an autoclaved, custom made ring consisting of polyether ether ketone (PEEK) was firmly attached to the cranial bone around the cover slip (Figure 6).

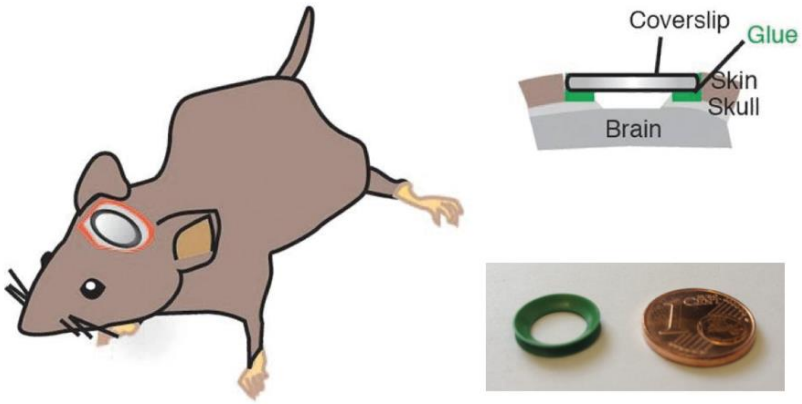

Figure 6 – Illustration of the chronic cranial window and the PEEK ring.
After fixation of the coverslip (diameter: 6mm), the PEEK ring (green, inner diameter: 8mm) is firmly attached onto the cranial bone surrounding the glass cover. European 1 cent coin (diameter: 16.25 mm) for scale. Adapted from (Alieva et al. 2014).

3.13 Stereotactic injection of tumor cells and CAR T cells

For establishment of the PCNSL animal model, no cranial windows were implanted. After induction of anesthesia and application of eye ointment, cefotaxime (250 mg/kg, Fresenius Kabi, Bad Homburg, Germany) was s.c. injected. Dexamethasone injection was omitted during tumor cell injection or T cell injection, as corticosteroid treatment impairs PCNSL growth (DeAngelis et al. 1990). Mice were immobilized in a stereotactic frame (David Kopf Instruments, Tujunga, USA) on a heating mat. Disinfection of the cranial skin was carried out using povidone-iodine solution (Braunol, B. Braun Melsungen AG). Subsequently, a small paramedian incision above the stereotactic coordinates (1 mm lateral and 2 mm posterior to the bregma) was made. After removal of the skin and the epicranial aponeurosis, a small part of the cranium with a diameter of 0.5 mm was carefully drilled away using a dental drill equipped with a sterile carbon steel micro drill (tip diameter: 0.5mm, Fine Science Tools Germany). Before tumor cell injection, cells were repeatedly washed and resuspended in DPBS. Cell viability and concentration was measured using trypan blue exclusion test. Raji, U-2932, OCI-LY3, OCI-LY10, and HKBML cells, at a viability of more than 95%, were filtered to a single cell solution in 1-2 µl

of DPBS and stereotactically injected using a modified Koch stereotactic adapter and a 10 µl Hamilton gas-tight microsyringe (Hamilton, Reno, USA) with a 32 gauge needle (45° bevel degree, Hamilton, Reno, USA) at an intraparenchymal depth of 2 mm. To determine optimal number of injected cells, 2.5 x 10^4 to 2.5 x 10^5 tumor cells were injected at varying numbers (n = 36 in total). After tumor cell injection, the skin was closed using simple interrupted stitches with non-absorbable 5-0 sutures.

To follow intracranial tumor growth with intravital TPLSM, fluorescent lymphoma cells were implanted into mice equipped with chronic cranial windows. To prevent postsurgical astroglial or microglial activation affecting tumor growth, stereotactic tumor implantation was performed at least two weeks after cranial window implantation. After induction of anesthesia and application of eye ointment, cefotaxime (250 mg/kg, Fresenius Kabi Germany) was s.c. injected. Mice were immobilized in a stereotactic frame (David Kopf Instruments) on a heating mat. Disinfection of the cranial skin was carried out by applying povidone-iodine solution (Braunol), followed by careful removal of the cover glass. Fluorescent lymphoma cells (U-2932tdt or OCI-LY10tdt, as indicated) were washed and resuspended in sterile DPBS and filtered to a single cell solution in 1-2 µl of DPBS. 2.5 x 10^5 lymphoma cells were stereotactically injected 1 mm lateral and 2 mm posterior to the bregma at an intraparenchymal depth of 1 mm (Figure 7). After injection, a new, sterile cranial window was attached. TPLSM was performed at regular intervals to analyze intracranial PCNSL growth pattern.

To evaluate CAR T cell effects on intracranial PCNSL growth, cranial window and tumor cell implantation was done as described before. For CAR T cell injection, mice were randomized to treatment groups 14 days after tumor implantation. One day before CAR T cell injection (day 13), tumor presence was confirmed via epifluorescence microscopy. After induction of anesthesia, application of eye ointment and cefotaxime, mice were immobilized as above. Disinfection of the cranial skin was carried out by applying povidone-iodine solution (Braunol), followed by careful removal of the cover glass. 5x10^4 h1928z CAR T cells or mock CAR T cells were injected 1 mm posterior to the tumor injection point at an intraparenchymal depth of 1 mm. After T cell injection, a cranial window was attached. TPLSM was performed at days 1, 4, 8, 14, 21, 28 and thereafter at biweekly intervals.

For validation experiments, mice without cranial windows were used. Briefly, 2.5 x 10^5 tumor cells were injected as described. 14 days thereafter, 2 x 10^4 h1928z CAR T cells or mock CAR T cells were injected at an intraparenchymal depth of 2 mm. After injection, the skin was closed using simple interrupted stitches with non-absorbable 5-0 sutures. At day 5, 10 and 25 after T cell injection, CAR T cells were quantified by blood sampling of the

facial vein. 28 days after T cell injection, mice were perfused and brain and lymph nodes extracted.

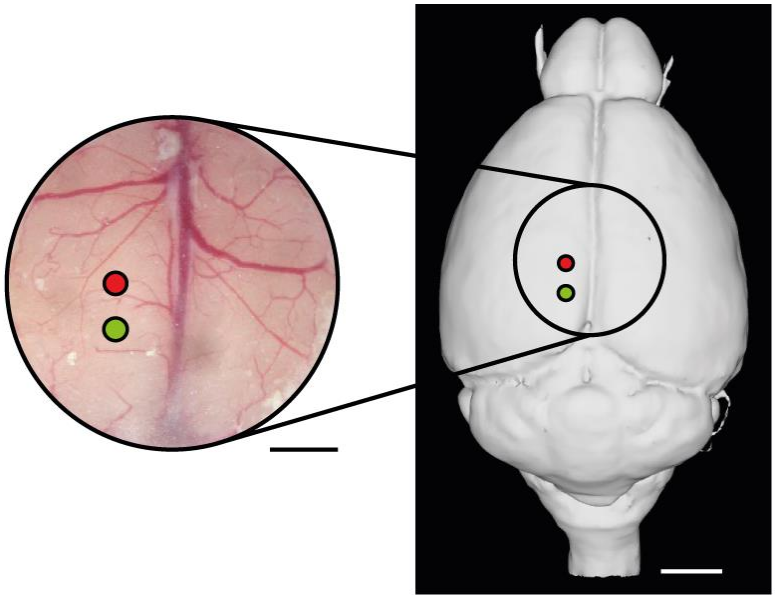

Figure 7 – Injection sites for stereotactic tumor cell and CAR T cell injection.
Brain surface photography through a cranial window (left) and 3D model of mouse brain (right) illustrating sites of stereotactic tumor cell (red) and CAR T cell (green) injection. Scale bars, 1 mm (left), 2 mm (right). Right: adapted from (Bakker, Tiesinga, and Kotter 2015).

3.14 Two-photon laser scanning microscopy

For TPLSM, we used a Multiphoton TrimScope I system (LaVision BioTec, Bielefeld, Germany) connected to an upright Olympus microscope (Olympus, Tokyo, Japan), equipped with a MaiTai Laser (690-1040 nm, Spectra Physics, Santa Clara, USA) and either a 20x water immersion objective (numerical aperture 0.95, Olympus XLUMPlanFl, Olympus) with double distilled water as immersion medium, or a 4x objective (numerical aperture 0.28, Olympus XLFluor 4x/340). Signals were collected with three non-descanned PMTs (G6780-20, Hamamatsu). The following filter combination was used: second harmonic generation (SHG) signals were collected with reflection of two longpass dichroic mirrors (560 nm and 495 nm). eGFP signal was collected with the same longpass dichroic mirrors (560 nm and 495 nm) and a band-pass filter (525/50). TdTomato signal was collected with two longpass dichroic mirrors (560 nm and 615 nm) and a band-pass filter (593/40). To visualize FITC-dextran and tdTomato simultaneously, the MaiTai laser

was tuned to 775 nm. To visualize eGFP, tdTomato and the SHG signal simultaneously, an excitation wavelength of 920 nm was used. Except when stated otherwise, z-stacks acquired had dimensions of 450x450 µm with 400 µm depth, a z-interval of 5 µm and a resolution of 1024x1024 pixels or 512x512 pixels. Except when stated otherwise, time lapse movies were acquired at dimensions of 450x450 µm with 65 µm depth with a z-interval of 5 µm at a resolution of 1024x1024 pixels with 1 stack acquired every 30 seconds. Imspector (LaVision Biotec, Bielefeld, Germany) software was used for image acquisition. During microscopy, mice were anesthetized using isoflurane in oxygen at a constant concentration of 1.0 to 2.0%, adjusted according to breathing rate. Body temperature was kept constant by fixation of the mouse on top of a heating pad with temperature tester. During imaging, the PEEK ring was tightly secured into a custom built fixation device (Figure 8). For visualization of cerebral vessels, 0.1 ml of FITC-dextran (2 MDa molecular weight, Sigma-Aldrich) were injected i.v. at a concentration of 10 mg/ml. Each microscopy session was limited to a maximum of 2 hours.

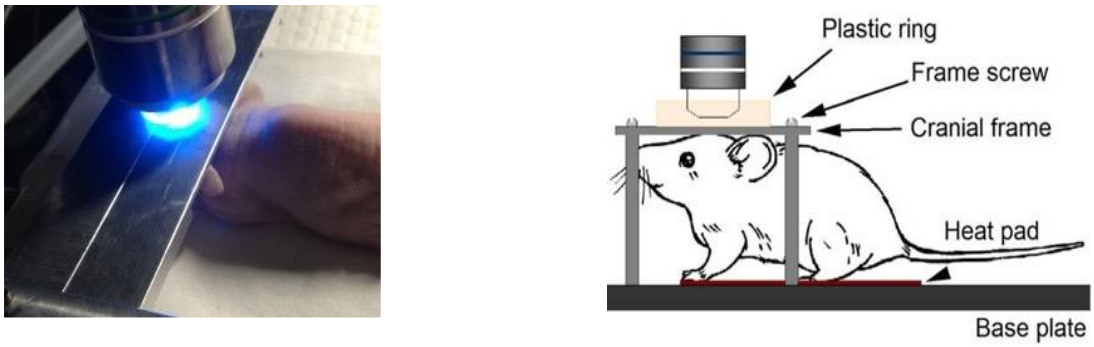

Figure 8 – Setup for intravital microscopy.
Left: Photography of the setup for epifluorescence and two-photon laser scanning microscopy demonstrating fixation of the anesthetized mouse on a heating mat. Right: Illustration, adapted from (Perez-Alvarez, Araque, and Martin 2013).

3.15 Image analysis

For image analysis, ImageJ/Fiji (National Institutes of Health, Bethesda, USA) and Imaris (Bitplane AG, Zurich, Switzerland) were used. For mosaic creation, maximum intensity projections of three-dimensional stacks were created using the Z-Project plugin of ImageJ/Fiji, followed by manual alignment using the MosaicJ function and use of the *despeckle* function for noise reduction (median filter; each pixel is replaced by the median value in its 3x3 neighborhood).

3.16 Semi-automatic T cell quantification

Quantification of intratumoral and intracerebral T cells was done using Imaris (Bitplane AG). Briefly, the three-dimensional image stack (450 x 450 x 400 µm, x/y/z) was loaded and the “cells” function was used to identify CAR T cells (source channel: GFP, smoothing filter width: 0.88µm without background subtraction). Cell threshold (absolute intensity) and number of voxels were manually adjusted to identify cells, (usually >180 and >160, respectively). Z-position was saved for each cell (Figure 9). For cell migration, the same settings were used, and cell velocity was saved for each individual cell track using Imaris software (Figure 20).

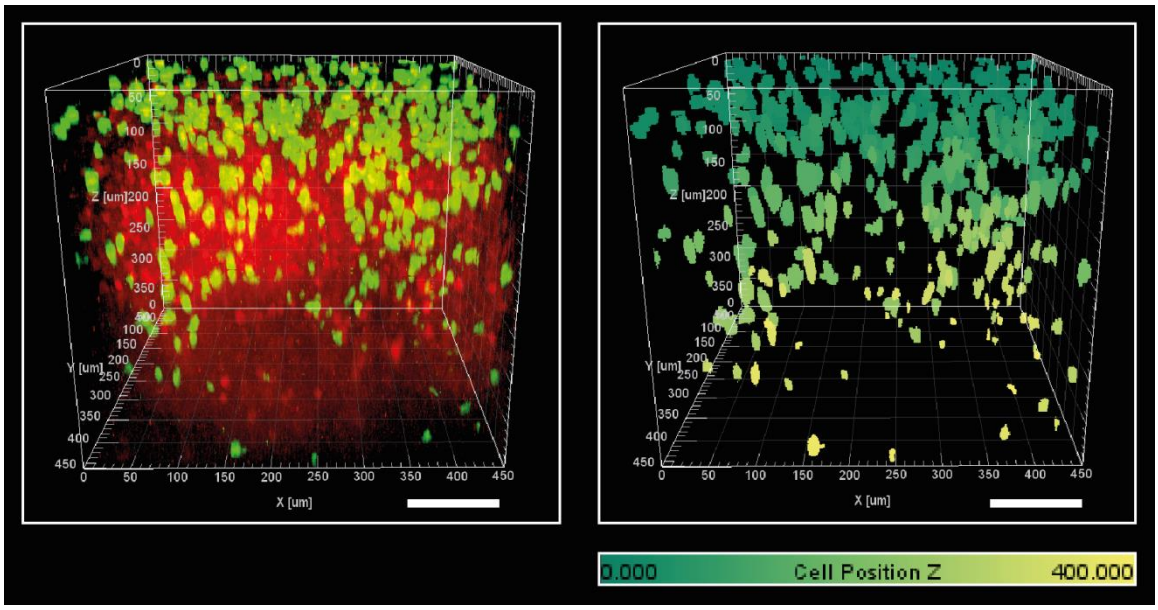

Figure 9 – Semi-automatic quantification of CAR T cell z-position.
Left: Three-dimensional visualization of TPLSM images showing intratumoral CAR T cells (green) and tumor cells (red). Right: Computer generated cell visualization. The top of the picture represents the cranial window, i.e. a z-position of 0 µm. Z-position was color-coded (dark green = 0 µm beneath the window, yellow = 400 µm below the window). Scale bar, 100 µm.

3.17 Tumor volume calculation via epifluorescence microscopy

To estimate tumor size using intravital microscopy, a spherical volume was assumed based on the two-dimensional diameters (anterior-posterior and left-right) during epifluorescence microscopy according to the following formula, modified after (Tomayko and Reynolds 1989):

$$\text{Volume} = 4/3 \times \text{pi} \times r^3$$

$$r = (\text{length}/2 + \text{width}/2)/2$$

If more than one tumor was visible, individual volumes were added.

3.18 Immunofluorescence

After anesthesia with MMF, intracardiac injection of 20 ml of saline chloride solution (0.9%), followed by intracardiac injection of freshly prepared 4% paraformaldehyde (PFA) in Dulbecco's phosphate-buffered saline (DPBS, v/v) was performed. Brain and lymph nodes were extracted and kept overnight in 4% PFA at 4°C for fixation. Afterwards, the organs were immersed in increasing sucrose solutions (10%, 20%, 30% sucrose in DPBS (w/v)) and kept overnight at 4°C until equilibrated. After equilibration in 30% sucrose solution, brains were frozen in the gas phase of liquid nitrogen and kept at -80°C until cryosectioning. Tissues were cut into 15 µm cryosections using a cryostat (Leica CM 1950, Leica, Wetzlar, Germany). The sections were kept in the dark at -20°C until staining.

3.19 Antibodies and reagents

After thawing at room temperature, cryosections were incubated for 10 minutes at 37°C and washed twice in TNT washing buffer (containing 0.1M Tris-HCl, 0.15M NaCl, 0.05% Tween 20, Perkin Elmer, Waltham, USA). Afterwards, cryosections were kept in 0.3% H_2O_2 in methanol (v/v), washed three times and blocked using TNB blocking buffer (containing 0.1M Tris-HCl, 0.15M NaCl, 0.5% blocking reagent (w/v), Perkin Elmer). Next, samples were incubated with primary antibodies at 4°C in TNB blocking buffer overnight, washed three times and incubated with the appropriate fluorophore-conjugated secondary antibodies in TNB blocking buffer. After three times washing with TNT washing buffer, the sections were stained with 4',6-Diamidino-2-phenylindole (DAPI), washed and mounted with Dako fluorescence mounting medium (Dako, Glostrup, Denmark). The following primary antibodies were used: goat anti-human CD20 (4 µg/ml or 3 µg/ml, ab194970, abcam, Cambridge, UK), rat anti-mouse CD3 (15 µg/ml, MAP4841, R&D Systems, Minnesota, USA). The following secondary antibody conjugates were used: donkey anti-goat Alexa Fluor (AF) 594 (1:200, A11D58, Thermo Fisher Scientific), donkey anti-rat AF594 (1:200, A21203, Thermo Fisher Scientific), or donkey anti-rat AF488 (1:200, A21208, Thermo Fisher Scientific).

3.20 Tumor volume and intratumoral CAR T cell measurement via immunofluorescence

After cranial window implantation, the intracranial volume is artificially expanded by the partial removal of cranial bone. Therefore, to measure the exact tumor volume, only mice without prior cranial window implantation were used. After anti-CD20 staining of 15 µm cryosections spaced 495 µm apart, immunofluorescent pictures were created for each slice on a BX60 upright microscope (Olympus). Tumor areas were manually delineated and measured using Axiovision software (Carl Zeiss Microscopy GmbH, Jena, Germany) If multiple tumors were present on one slice, individual tumor areas were added. Total tumor area per slice was multiplied with 0.495. Addition of all values yielded total tumor volume.

To determine intratumoral CAR T cell density, mosaics of these immunofluorescently stained cryosections were created on a Zeiss AxioImager.M2 upright microscope (Carl Zeiss Microscopy GmbH) using Axiovision software (Carl Zeiss Microscopy). Briefly, all intratumoral CAR T cells were counted manually and divided by the total volume of tumor in this cryosection (two-dimensional tumor area multiplied by cryosection thickness, i.e. 0.015).

3.21 Blood sampling

30 minutes before blood sampling, mice were s.c. injected with 0.1 mg/kg buprenorphine. Anesthesia was induced with 5% isoflurane in oxygen. As soon as the righting reflex was absent (indicating deep anesthesia), the facial vein was punctured using a small lancet (Solofix, B. Braun Melsungen AG). Blood drops were collected in EDTA coated capillary tubes (Microvette, Sarstedt AG & Co., Nümbrecht, Germany). $eGFP^+$ cells were quantified on a FACSAria (BD Biosciences, San Jose, USA) flow cytometer.

3.22 Statistical analysis

Data are expressed as mean +/- standard deviation, mean +/- s.e.m., or median +/- interquartile range, as indicated. For comparison of groups, the Mann-Whitney *U* test or Wilcoxon test was used, as indicated. A level of $p < 0.05$ was considered significant.

Calculations were performed using Graphpad Prism 7.02 for Windows (GraphPad Software, Inc., San Diego, USA).

3.23 Treatment allocation and blinding

Mice were randomized to treatment groups via coin toss. In accordance with guidelines for the design of animal experiments (Festing and Altman 2002), the author was blinded for treatment group allocation until data analysis was completed.

4 Results

4.1 Establishment of the PCNSL animal model

To establish a mouse model closely resembling human PCNSL growth, we compared five different human B-cell lymphoma cell lines regarding their histopathological and clinical growth patterns:

- Raji, derived from a patient with Burkitt's lymphoma
- U-2932, derived from a patient with DLBCL
- OCI-LY10, derived from a patient with DLBCL
- OCI-LY3, derived from a patient with DLBCL
- HKBML, derived from a patient with primary CNS lymphoma

After intracerebral, stereotactic implantation of these tumor cell lines at different concentrations (at least n = 3 per group), large, well-established intracerebral tumors were found in all groups. Histopathological comparison of these intracerebral tumors was performed to identify the cell line with highest accordance with human PCNSL. For further investigations, we decided to use the cell lines U-2932 and OCI-LY10 for the following reasons:

- Both are derived from a DLBCL primary tumor, similar to 90-95% of PCNSL lesions (Braaten et al. 2003; Rubenstein, Treseler, and O'Brien 2005)
- They form a solitary lesion with meningeal dissemination and perivascular growth (Figure 10), similar to human PCNSL (Kuker et al. 2005; Haldorsen, Espeland, and Larsson 2011; He et al. 2013)

- After stereotactic injection of 2.5 x10^5 cells, mice had a symptom-free survival of at least 40 days, therefore forming an ideal model to evaluate treatment effects of late treatment initiation, i.e. two weeks after tumor implantation.

The last point is of particular importance for the following two reasons: First, tumor growth for a prolonged duration leads to a tumor microenvironment different to the tumor microenvironment present immediately after implantation. These factors include changes in the cellular and humoral microenvironment and, in intracerebral tumors, include an impaired blood brain barrier. Many of these relevant features become present at least 14 days after orthotopic tumor implantation (Yu et al. 2006), when tumors become exceptionally difficult to eradicate in mice. Second, to reliably visualize intracerebral tumor growth during treatment using TPLSM, tumor size must exceed a certain threshold diameter to enable visualization of tumor cells within the most superficial 500µm of the cerebral cortex, a size more reliably achievable after two weeks of intracerebral tumor growth.

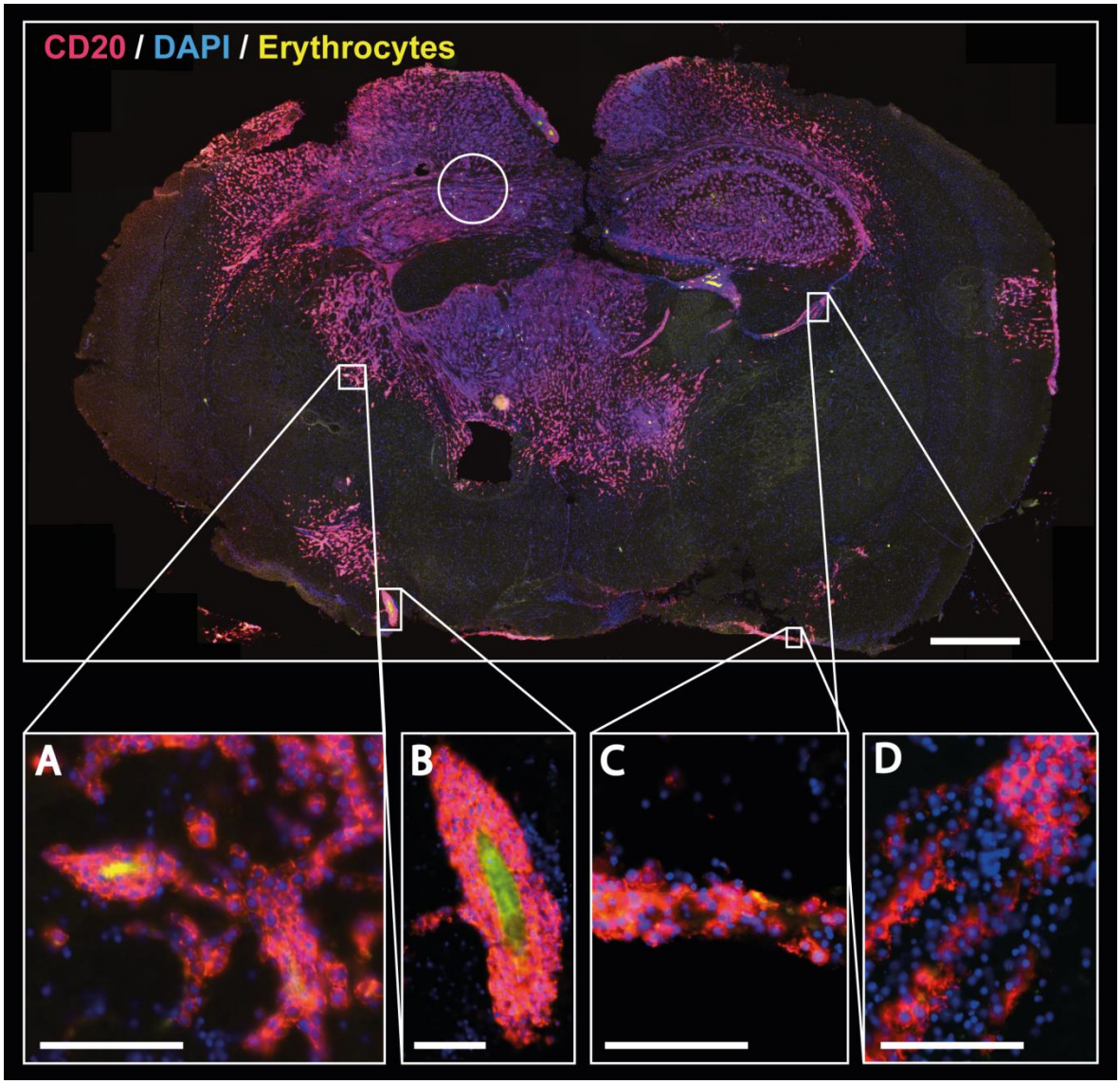

Figure 10 – Immunofluorescence of the mouse brain 49 days after stereotactic lymphoma implantation.
Stereotactic, intracerebral injection of 2.5x10^5 OCI-LY10 cells (circle) led to growth of a big, solitary cerebral lymphoma with several satellite lesions present at superficial, intraparenchymal and periventricular regions. The solid tumor invades big parts of the brain parenchyma, including the superficial and hippocampal structures in the contralateral brain hemisphere. (**A** and **B**) Perivascular lymphoma growth (pink) can be seen surrounding small (A) and big (B) intracerebral blood vessels. (**C**) Meningeal dissemination can be found at several regions. (**D**) Periventricular growth involves the subependymal structures and the choroid plexus. Representative immunofluorescence of OCI-LY10 cells with CD20 immunostaining (pink), erythrocytes autofluorescence (yellow) and 4',6-diamidino-2-phenylindole (DAPI) nuclear staining (blue). Scale bars, 1 mm (big panel) or 100 µm (A, B, C, D).

To summarize, stereotactic intracranial injection of 2.5 x 10^5 U-2932 or OCI-LY10 cells led to reliable intracerebral lymphoma growth, closely mimicking the neuropathological characteristics of human PCNSL.

Histopathological analysis of intracranial tumors enables analysis of the whole mouse brain, including the cellular tumor architecture and microenvironment, at a single time point. However, the growth of these tumors and their individual development over time cannot be followed via histopathological analysis alone. Furthermore, dynamic processes such as changes in vessel architecture, formation of secondary lesions, and treatment effects are impossible to analyze histopathologically at several time points in the same mouse. Thus, to analyze tumor growth repeatedly in the same animal, we next aimed to perform TPLSM through a chronic cranial window to repeatedly visualize tumor growth.

4.2 Stable transfection of lymphoma cell lines

To reliably follow intracranial lymphoma growth over a period of several weeks, lymphoma cells need to stably express a fluorescent protein. Therefore, our next step was to transfect these lymphoma cells with a fluorescent protein.

TdTomato is a well-established, non-toxic tandem dimer of a red fluorescent protein. Additionally to its non-toxic properties, it is known for its advantageous fluorescence properties compared to older examples such as DsRed2, especially regarding fluorescence intensity and light absorption (Drobizhev et al. 2011).

Electroporation of the pLVX-tdTomato-IRES-Neo plasmid yielded transfection efficiency rates of about 10% for both lymphoma cell lines, U-2932 and OCI-LY10. Repeated FACS sorting was performed to obtain the cells with highest fluorescence intensity. After five times of FACS sorting the 5% of cells with highest fluorescence intensity, all cells showed high fluorescence. Importantly, fluorescence intensity of these cells remained stable for several weeks during *in vitro* subculturing; no cells showed loss of intrinsic red fluorescence. *In vitro* growth rates did not significantly differ between tdTomato$^+$ and wild-type lymphoma cells. To simulate *in vivo* conditions, where selection agents are not present, we tested fluorescence intensity after 4 weeks of culture in the absence of the selection compound G418. Interestingly, under G418-free conditions, fluorescence intensity further increased, possibly improving imaging quality *in vivo*.

All in all, these experiments ensured stable expression of tdTomato in both lymphoma cell lines: tdTomato$^+$ U-2932 (U-2932tdt) and tdTomato$^+$ OCI-LY10 (OCI-LY10tdt).

4.3 Visualization of PCNSL growth *in vivo*

TPLSM enables users to create high quality three-dimensional image stacks with single-cell resolution and very low phototoxicity. Combining TPLSM with a chronic cranial window allows for long-term follow up of individual tumor cells inside the mouse cortex (Kienast et al. 2010; von Baumgarten et al. 2011). Therefore, our next aim was to analyze the development and growth characteristics of primary CNS lymphoma *in vivo*.

After implantation of a cranial window, the leptomeninges and the cortex could be visualized up to a depth of 500 µm. Two weeks after implantation of a cranial window, we injected 2.5 x 10^5 U-2932tdt or OCI-LY10tdt into the mouse cortex 1 mm lateral, 2 mm posterior to the bregma, at an intraparenchymal depth of 1 mm. Over time, PCNSL growth and the intracerebral vasculature, visualized with i.v. FITC-dextran injection, were followed repeatedly (Figure 11). To the best of our knowledge, these are the first experiments illustrating *in vivo* PCNSL growth in detail.

During the first days after stereotactic tumor cell implantation, a small cluster of lymphoma cells were found at the injection site. These cells formed a solitary lesion with close cell-cell contacts and a close association with preexisting intracerebral blood vessels. A few cells were seen infiltrating into the intraparenchymal peritumoral vicinity. Over the course of several weeks, tumor growth led to enlargement of the visible part of the tumor. 43 days after tumor implantation, single cortical tumor cells were found at distant sites such as the contralateral brain hemisphere, reflecting the histopathological growth pattern of advanced human PCNSL, often being considered a whole brain disease (Lai, Rosenblum, and DeAngelis 2002).

Following tumor growth over time, numerous satellite cells became visible. These cells, visible at a distance of more than 100 µm to solid tumors, often showed close contact with blood vessels. Some of these satellite cells were found at the same position over several weeks, resembling dormant tumor cells, i.e. quiescent cells with no apparent mitotic activity (Aguirre-Ghiso 2007). In time lapse analyses, these satellite cells, similar to tumor cells inside the solid tumor, showed no relevant migratory behavior over a time frame of one hour.

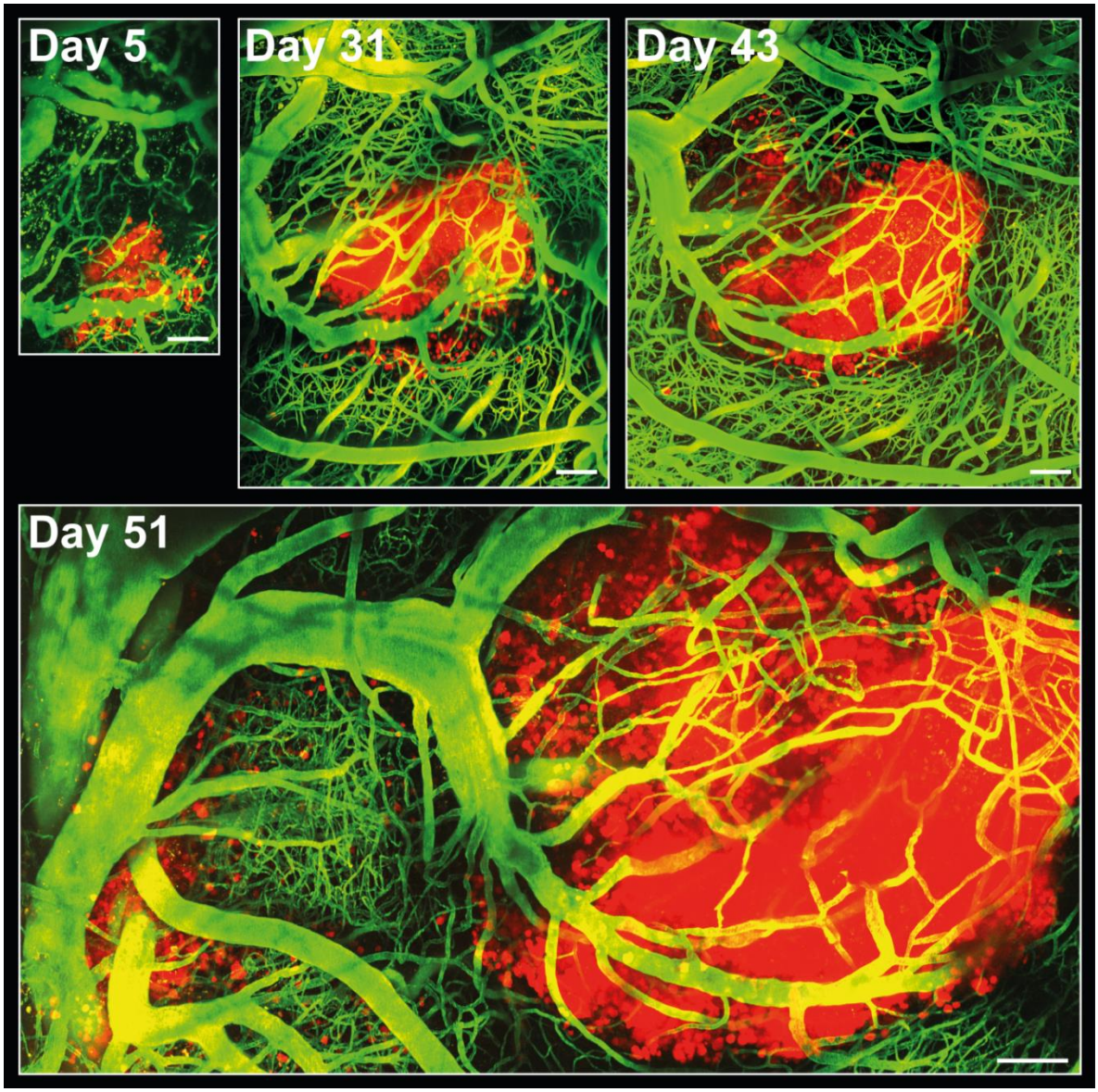

Figure 11 – Two-photon microscopy of cortical PCNSL growth *in vivo*.
Representative TPLSM images of PCNSL growth for 51 days after stereotactic intracortical implantation of 2.5 x 10^5 tdTomato$^+$ U-2932 (U-2932tdt) cells. Mosaics of maximum intensity projections with dimensions of 555 x 555 x 400 µm (x/y/z) per region of interest (ROI). Blood vessels were visualized after i.v. injection of FITC dextran in green, with tdTomato$^+$ lymphoma cells (U-2932tdt) in red. Scale bar, 100 µm.

Thus, combining a chronic cranial window, stereotactic intracerebral implantation of stably fluorescent lymphoma cells and regular TPLSM enables repeated analysis of *in vivo* PCNSL growth in unprecedented detail.

4.4 *In vitro* analysis of h1928zCAR T cell cytotoxicity

The most successful CARs to date are second-generation anti-human CARs targeting CD19, a surface antigen specifically expressed by cells of the B cell lineage (Sadelain 2015). Recently, it has been reported that the widely used U-2932 cell line is comprised of two different subclones of cells, representing two phenotypically stable subpopulations with double peaks of individual CD markers, including CD19 (Quentmeier et al. 2013). Therefore, to verify that anti-CD19 CAR T cell effects on lymphoma cells are specifically based on CAR function rather than on varying antigen expression on tumor cells, we restricted the following *in vitro* and *in vivo* experiments using CAR T cells to the human $CD19^+$ DLBCL cell line OCI-LY10tdt.

In our experiments, we used the h1928z anti-human CD19 CAR (consisting of a murine anti-**h**uman CD**19** scFv, a murine CD**28** costimulatory domain, and the murine CD3**z**eta intracellular signaling domain), modified from (Paszkiewicz et al. 2016). To evaluate the therapeutic efficacy of h1928z CAR T cells in the treatment of orthotopic PCNSL, we decided to first test their cytotoxic capabilities *in vitro*.

h1928z CAR T cells are produced by transduction of *in vitro* activated murine T cells using CD3 and CD28 antibodies in IL-2 containing cell medium. In addition to the chimeric antigen receptor, these activated T cells are equipped with functional T cell receptors (TCR). Therefore, murine CAR T cells theoretically possess two independent mechanisms of killing human lymphoma cells: via TCR-signaling or via CAR-signaling. Hence, comparison to similarly activated murine T cells is necessary to delineate CAR-specific cytotoxicity. To further control for potential effects of the transduction procedure on T cell cytotoxicity, we decided to compare the functional h1928z CAR T cells to T cells transduced with m1928z, a CAR construct specifically binding to murine CD19, an antigen not present on human lymphoma cells.

Therefore, we compared the *in vitro* cytotoxicity of two different second-generation CAR constructs:

- The anti-human CD19 (h1928z) CAR, targeting human CD19 present on the surface of OCI-LY10tdt cells
- The anti-mouse CD19 (m1928z) CAR, targeting murine CD19 not present on the surface of OCI-LY10tdt cells.

To further determine the most effective effector cell / target cell (E / T) ratio, we cultured 7,500 OCI-LY10tdt cells together with CAR T cells at CAR T cell / OCI-LY10tdt cell ratios ranging from 1:128 to 2:1. After 4 hours of co-culture, h1928z CD19 CAR T cells showed ratio-dependent cytotoxicity, with up to 60% of OCI-LY10tdt cells dead after co-incubation at an E / T ratio of 2:1 (Figure 12). Surprisingly, in the control group using m1928z CAR T cells, less than 3 percent of lymphoma cells were killed, suggesting that irrespective of chimeric antigen receptor, murine T cells show no significant contribution of TCR signaling to tumor cytotoxicity during 4 h of *in vitro* co-culture.

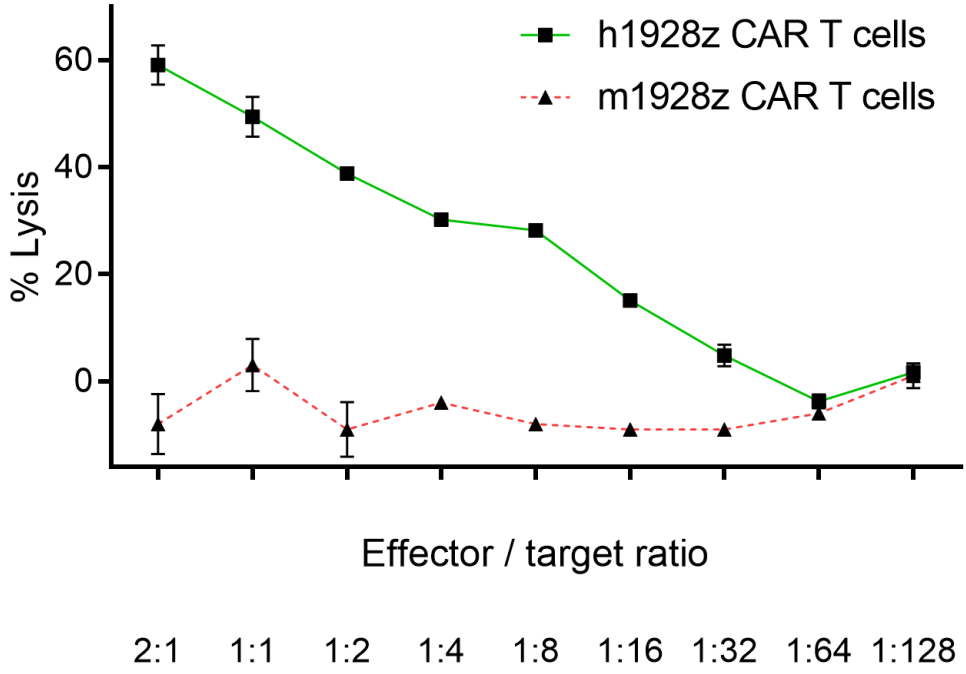

Figure 12 – *In vitro* cytotoxicity of h1928z CAR T cells and m1928z CAR T cells.
h1928z CAR T cells exhibit a ratio-dependent cytotoxicity against human OCI-LY10tdt cells, while m1928z CAR T cells do not lead to tumor cell lysis. *In vitro* LDH assay, measuring cellular cytotoxicity of h2918z CAR T cells and m1928z CAR T cells against human $CD19^{+}$ OCI-LY10tdt cells across a range of different effector / target cell ratios after 4 hours of co-incubation. Mean +/- standard deviation of triplicate wells.

4.5 Allogeneic CAR T cells control PCNSL growth, but persist for less than 3 weeks

Next, we aimed to assess the therapeutic utility of h1928z CAR T cells in PCNSL *in vivo*. Establishment of a big, solid tumor with at least 500 µm in visible, superficial diameter usually occured 10-14 days after tumor implantation. Accordingly, 14 days after tumor implantation, allogeneic green fluorescent h1928z CAR T cells (derived from C57BL/6J beta-actin eGFP$^+$ mice) were stereotactically injected into the mouse cortex 1 mm posterior of the tumor injection site, at a depth of 500 µm (day 1).

4 days after CAR T cell injection, T cells were found inside the tumor and the tumor periphery in high numbers (Figure 13). The number of visible T cells further increased over the following days, while the visible tumor size kept growing very slowly (at a much slower rate compared to tumor growth without CAR T cell therapy). At day 15, CAR T cells were still visible intra- and peritumorally in high numbers. Surprisingly, on day 21 after T cell injection, CAR T cell number dropped dramatically intratumorally (Figure 13) as well as extratumorally (n = 3 mice).

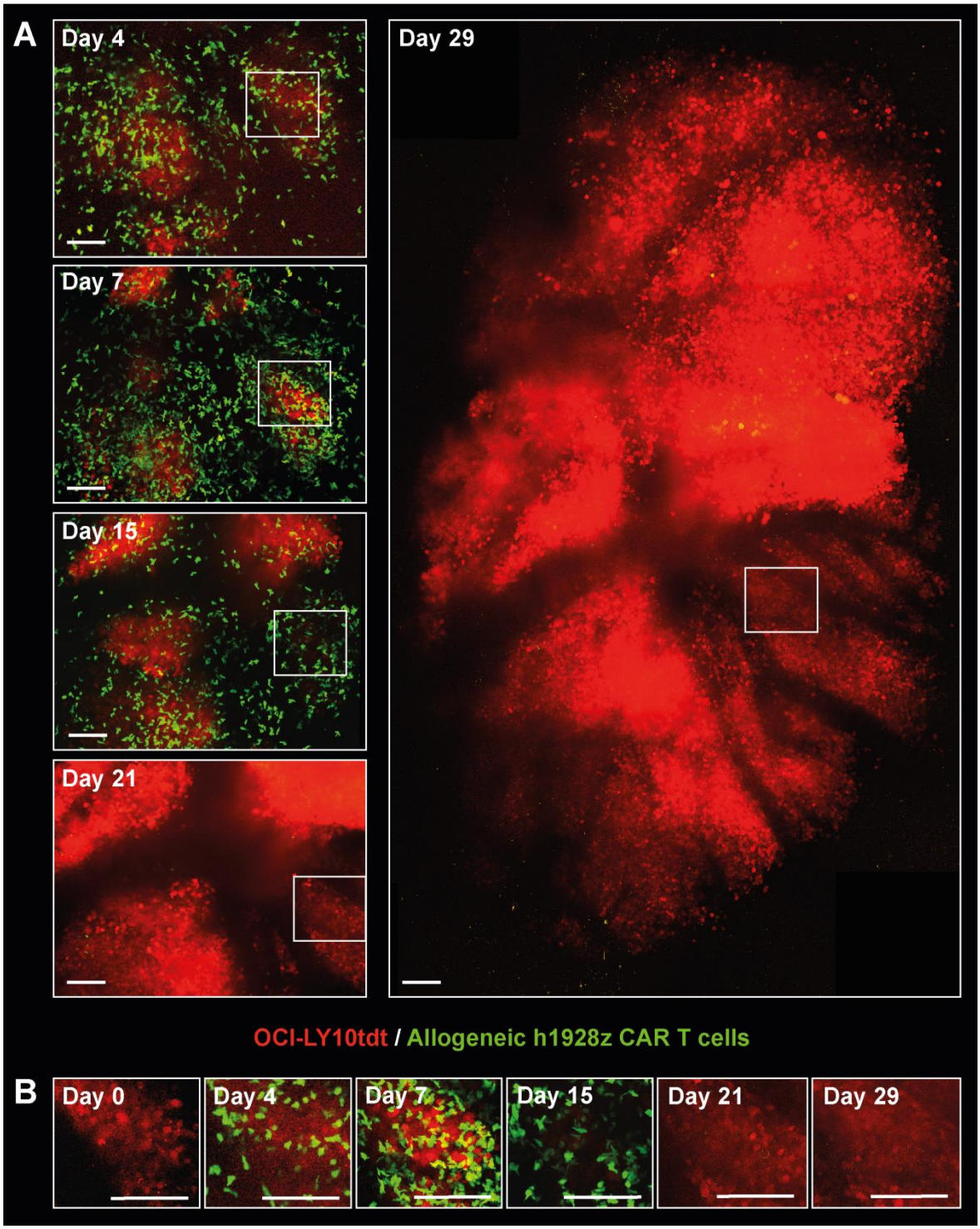

Figure 13 – Two-photon microscopy of tumor growth after allogeneic h1928z CAR T cell injection. Stereotactic injection of allogeneic h1928z CAR T cells impedes tumor growth, but CAR T cells persist for less than three weeks. (**A**) Two weeks after intracortical tumor implantation, $5x10^4$ allogeneic h1928z CAR T cells were stereotactically injected at a distance of 1 mm posterior to the tumor. Four days after CAR T cell injection, intra- and peritumoral CAR T cell accumulation becomes visible. On day 7 after CAR T cell injection, intratumoral T cells reach their peak density, while on day 15 still many intratumoral CAR T cells are found. On day 21, nearly no intratumoral CAR T cells remain visible, with exponential tumor growth taking place thereafter. Rectangle depicting the same ROI over time, details in (**B**). Intratumoral tdTomato$^+$ OCI-LY10 cells in red, beta-actin-eGFP$^+$ h1928z CAR T cells in green. Mosaic of maximum intensity projections with dimensions of 450 x 450 x 400 µm (x/y/z) per ROI. Representative cellular dynamics of three mice. Scale bars, 100 µm.

These results suggest that intracranial injection of allogeneic h1928z CAR T cells can control tumor growth, but do not lead to tumor regression, possibly due to their limited intratumoral and intracerebral persistence.

After intravenous injection of murine CAR T cells into allogeneic recipients, CAR T cell number has been reported to similarly diminish dramatically following day 15 after injection, consistent with rapid deletion in the context of graft-versus-host disease (Jacoby et al. 2016). Although our mice did not develop any symptoms suggestive of graft-versus-host disease, it seems conceivable that the limited persistence of the h1928z CAR T cells is due to the allogeneic background. Similar results have been described in irradiated mice receiving bone marrow transplantation, where rapidly proliferating T cells underwent peripheral apoptosis in allogeneic recipients, peaking between day 14 and day 21 after injection (Alpdogan et al. 2008). Therefore, we next aimed to assess the persistence of syngeneic h1928z CAR T cells compared to syngeneic mock CAR T cells after stereotactic, intracortical injection. The following experiments have been conducted with T cells isolated from syngeneic, heterozygous Foxn1$^{nu/+}$ mice retaining functional T cells.

4.6 Syngeneic CAR T cells eradicate PCNSL and persist for more than 4 weeks

For successful CAR T cell therapy, four steps are necessary for complete remission with sustained anti-tumor immunity:

1) CAR T cell trafficking into the solid tumor

2) CAR T cell activation and proliferation

3) Anti-tumor cytotoxicity, leading to tumor regression

4) Long term persistence of CAR T cells

None of these features has so far been visualized *in vivo*.

To address these four characteristics of successful CAR T cell therapy in an established cerebral tumor microenvironment in detail, we compared syngeneic eGFP transduced h1928z CAR T cells to mock CAR T cells, missing the obligate extracellular scFv domain.

14 days after intratumoral implantation, we injected $5x10^4$ CAR T cells into the cortex of mice bearing large, established PCNSL with a visible diameter of >500 µm.

During the 4 weeks following intracortical T cell injection, we performed regular TPLSM (Figure 14). Here, mock CAR T cells were present inside the cerebral tumor starting at day 4 after injection. While after 14 days, intratumoral T cells could still be seen, T cell numbers were significantly diminishing afterwards. Tumor growth was seemingly unimpeded during these four weeks, culminating in the development of a massive tumor with more than 3000 µm diameter at day 28, extending onto the contralateral brain hemisphere (Figure 14. The vertical gap in red fluorescence on the left side of the big panel (black) represents the superior sagittal sinus separating both brain hemispheres).

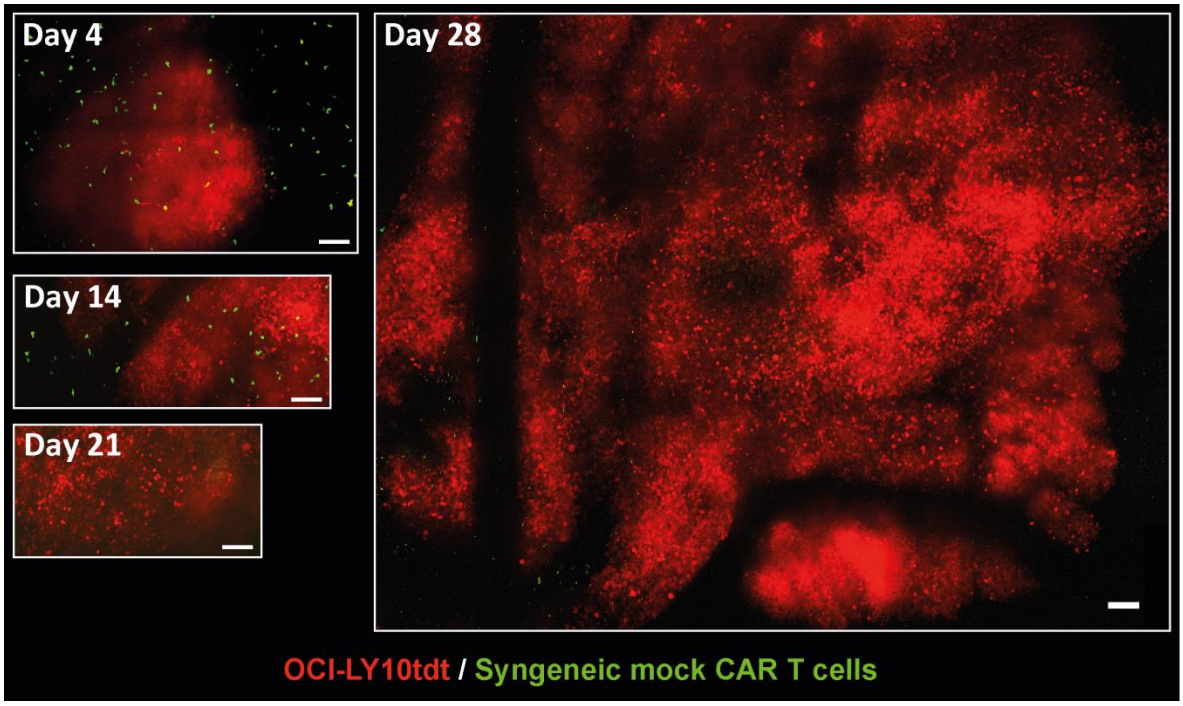

Figure 14 – Serial TPLSM of the interaction between mock CAR T cells and PCNSL.
Stereotactic injection of syngeneic mock CAR T cells (green) do not control orthotopic OCI-LY10tdt (red) growth and mock CAR T cells persist for less than three weeks. TPLSM images of intracranial PCNL growth for 28 days after intracortical mock CAR T cell injection. Four days after injection, mock CAR T cells accumulated intra- and peritumorally. At day 14, slightly less intratumoral mock CAR T cells were seen, while tumor size increased. Starting from day 21, only singular mock CAR T cells remained intratumorally. At day 28, the intracerebral tumor reached a diameter of more than 3000 µm, with less than 5 T cells present intratumorally. Mosaic of maximum intensity projections with dimensions of 450 x 450 x 400 µm (x/y/z) per ROI. Representative images of 4 mice. Scale bars, 100 µm.

In contrast, stereotactic injection of syngeneic h1928z CAR T cells led to a high intratumoral T cell density already at day 4 (Figure 15). Interestingly, intratumoral h1928z CAR T cell number further increased until day 14, and reached peak density at day 21

after T cell injection, while tumor size did not increase. 4 weeks after T cell injection, similar high T cell numbers were seen, while the tumor regressed with only two single tumor cells remaining visible (big panel, tumor cells indicated with a circle).

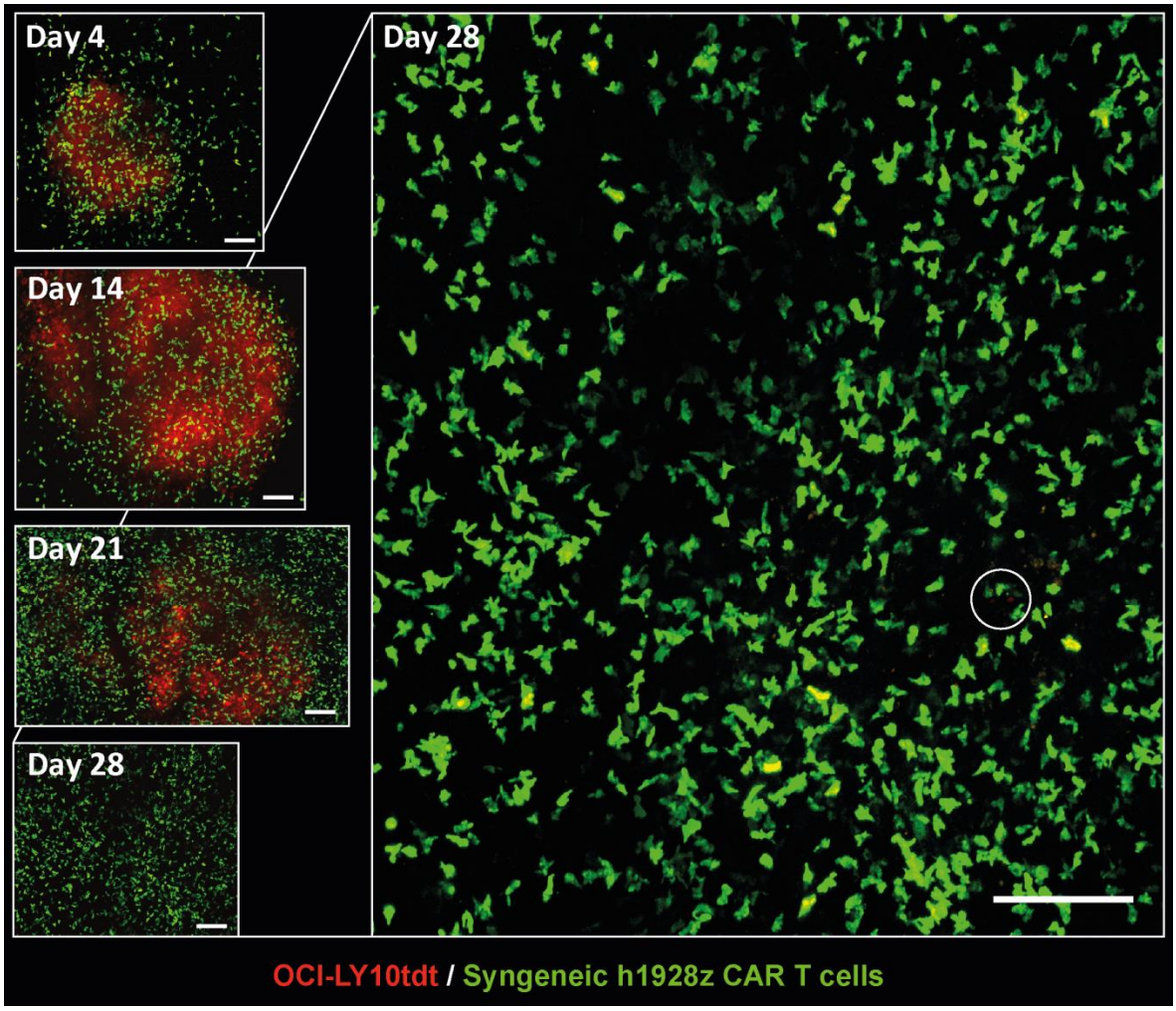

Figure 15 – Serial TPLSM of the interaction between h1928z CAR T cells and PCNSL.
Injection of syngeneic h1928z CAR T cells (green) leads to tumor regression and T cell persistence in high numbers for more than four weeks. TPLSM images of intracranial OCI-LY10tdt growth and tumor regression for 28 days after intracortical h1928z CAR T cell injection. 4 days after intracortical injection, syngeneic h1928z CAR T cells accumulated intra- and peritumorally. During the following weeks, CAR T cell number increased until intratumoral CAR T cell number reached its peak number on day 21. On day 28, the solid intracerebral lymphoma completely regressed (with only two tumor cells remaining visible, indicated with a circle in the big panel), while h1928z CAR T cells persisted in high numbers around the tumor injection site. Mosaics of maximum intensity projections with dimensions of 450 x 450 x 400 µm (x/y/z) per ROI. Scale bars, 100 µm.

4.6.1 CAR T cell trafficking into solid tumor

Next, we aimed to validate our observations by quantifying intratumoral CAR T cell density for h1928z CAR T cells and mock CAR T cells.

Directly after stereotactic T cell injection (day 0), mock CAR T cells as well as h1928z CAR T cells were present in the area surrounding T cell injection, but not inside the solid tumor (data not shown), providing evidence that intratumoral T cell numbers are the result of active T cell migration. As expected, on day 4 after T cell implantation, h1928z CAR T cells from both groups were found inside the tumor (Figure 16A). Already on day 4, intratumoral h1928z CAR T cells accumulated in higher numbers compared to mock CAR T cells. On day 8, intratumoral CAR T cell number further increased in both groups, reaching its peak density in the mock CAR T cell group. In the following weeks, mock CAR T cell numbers consistently decreased; at day 21 and 28, only low numbers of intratumoral mock CAR T cells were found. h1928z CAR T cells, on the other hand, showed a larger increase in number and reached their maximum intratumoral number at day 21 after T cell injection. At all time points after T cell injection, intratumoral h1928z CAR T cells exceeded the number of intratumoral mock CAR T cells (Figure 16A).

As PCNSL is a “whole brain disease” with infiltrative growth throughout the whole CNS (Lai, Rosenblum, and DeAngelis 2002), contralateral migration of CAR T cells would be suggestive of active CAR T cell surveillance of areas distant to the main tumor, potentially increasing the chance of immunotherapy to reach satellite lesions necessary for complete tumor eradication. Therefore, we determined to quantify the intracortical CAR T cell density in the contralateral brain hemisphere. To inhibit selection bias of areas showing higher T cell densities, we specifically measured the ROI directly opposite of the tumor injection site (i.e. in the contralateral brain hemisphere).

In the contralateral brain hemisphere, cellular kinetics are similar to intratumoral T cell numbers, although at lower numbers (Figure 16B). On day 4 after T cell injection, T cells of both groups have migrated to the region contralateral to the tumor injection site. On day 8, contralateral T cell number increases in both groups, showing no difference between groups. On day 14, mock CAR T cell number decreases, while h1928z CAR T cell number increases. On day 21 after T cell injection, mock CAR T cells are depleted, while h1928z CAR T cells can still be seen in high numbers (albeit in lower numbers compared to intratumoral h1928z CAR T cells). On day 28, h1928z CAR T cells are still present contralaterally, while the region contralateral to tumor injection was overgrown by tumor in 3 of 4 mice, precluding valid determination of contralateral mock CAR T cell number.

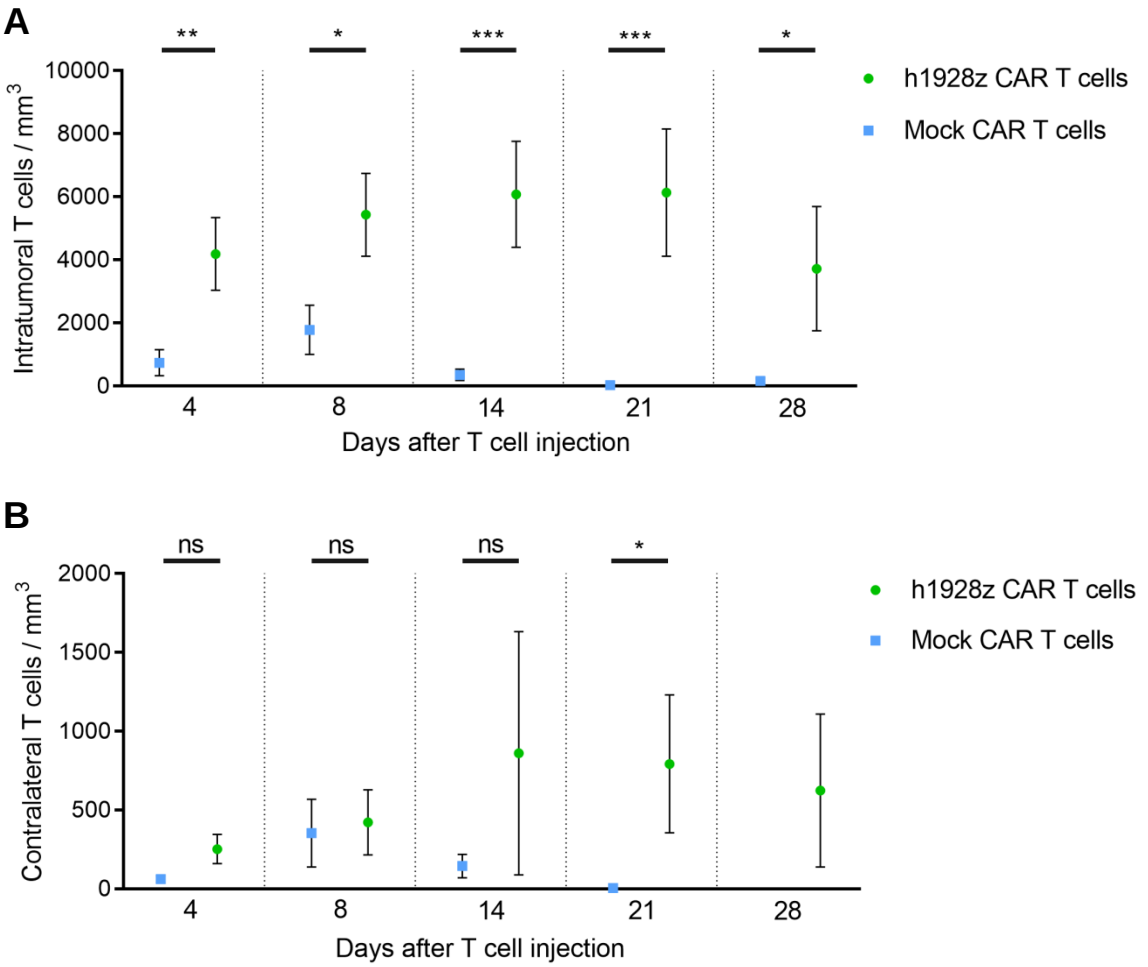

Figure 16 – Intratumoral and contralateral CAR T cell density.
h1928z CAR T cells show higher intratumoral numbers and persistence compared to mock CAR T cells (A). In the contralateral hemisphere, h1928z CAR T cells persist longer and at higher densities than mock CAR T cells (B). **A)** Intratumoral h1928z CAR T cell density increased until day 21 and h1928z CAR T cells stayed present in high numbers for at least 28 days. Intratumoral mock CAR T cells increased in number until day 8. 14 days after injection, intratumoral mock CAR T cells are less frequent and only exceptionally visible thereafter. T cell numbers quantified of 2 three-dimensional ROIs from 4 mice per group per time point. Pooled data from 4 independent experiments. Mean +/- s.e.m. Comparisons were made using the Mann-Whitney *U* test. *$p < 0.05$, **$p < 0.01$, ***$p < 0.001$. **B)** Both h1928z CAR T cells as well as mock CAR T cells migrated into the contralateral brain hemisphere, where they became visible already four days after injection, albeit at lower numbers compared to intratumoral T cells. Contralateral h1928z CAR T cells further increased in number over the following days and weeks, whereas contralateral mock CAR T cells were diminished in numbers until day 21. On day 28, in 3 of 4 mock CAR T cell mice, the tumors extended into the region contralateral to the tumor injection site, precluding quantification of contralateral mock CAR T cell number. In the h1928z CAR T cell group, T cells are still present in high numbers contralaterally for 28 days after injection. CAR T cell density of the ROI exactly contralateral to tumor injection site from 4 mice per group per time point. Pooled data from 4 independent experiments. Mean +/- s.e.m. Comparisons were made using the Mann-Whitney *U* test. ns = not significant, *$p < 0.05$.

To summarize, h1928z CAR T cells invaded the tumor in higher numbers, increased in number during a larger period, and persisted longer compared to mock CAR T cells. In the

contralateral brain hemisphere, h1928z CAR T cells and mock CAR T cells were initially found in similar numbers, but h1928z CAR T cells increased in number and persisted for more than 28 days, whereas mock CAR T cells were depleted at day 21 both intratumorally and contralaterally.

4.6.2 Intratumoral and intracortical CAR T cell distribution

Not only the intratumoral density of T cells, but also their intratumoral distribution plays a major role in anti-tumor efficacy. Especially in solid tumors, several physical and immunological barriers exist, potentially limiting CAR T cell penetration into the tumor core (Yong et al. 2017; Newick et al. 2017). Therefore, we determined the intratumoral and intracortical T cell z-position, i.e. the distance measured to the brain surface (0 µm = superficial, 400 µm = 400µm beneath the surface, Figure 9).

Interestingly, at all time points, T cells of the mock CAR group were predominantly accumulating at the most superficial intracerebral position (Figure 17A, B). This corresponds to the meningeal and subarachnoid space, where T cell immune surveillance is physiologically located in the healthy brain (Kivisakk et al. 2009; Ousman and Kubes 2012). Deep inside the tumor (i.e. more than 100 µm below the brain surface), more h1928z CAR T cells were found at all time points. (Figure 17C).

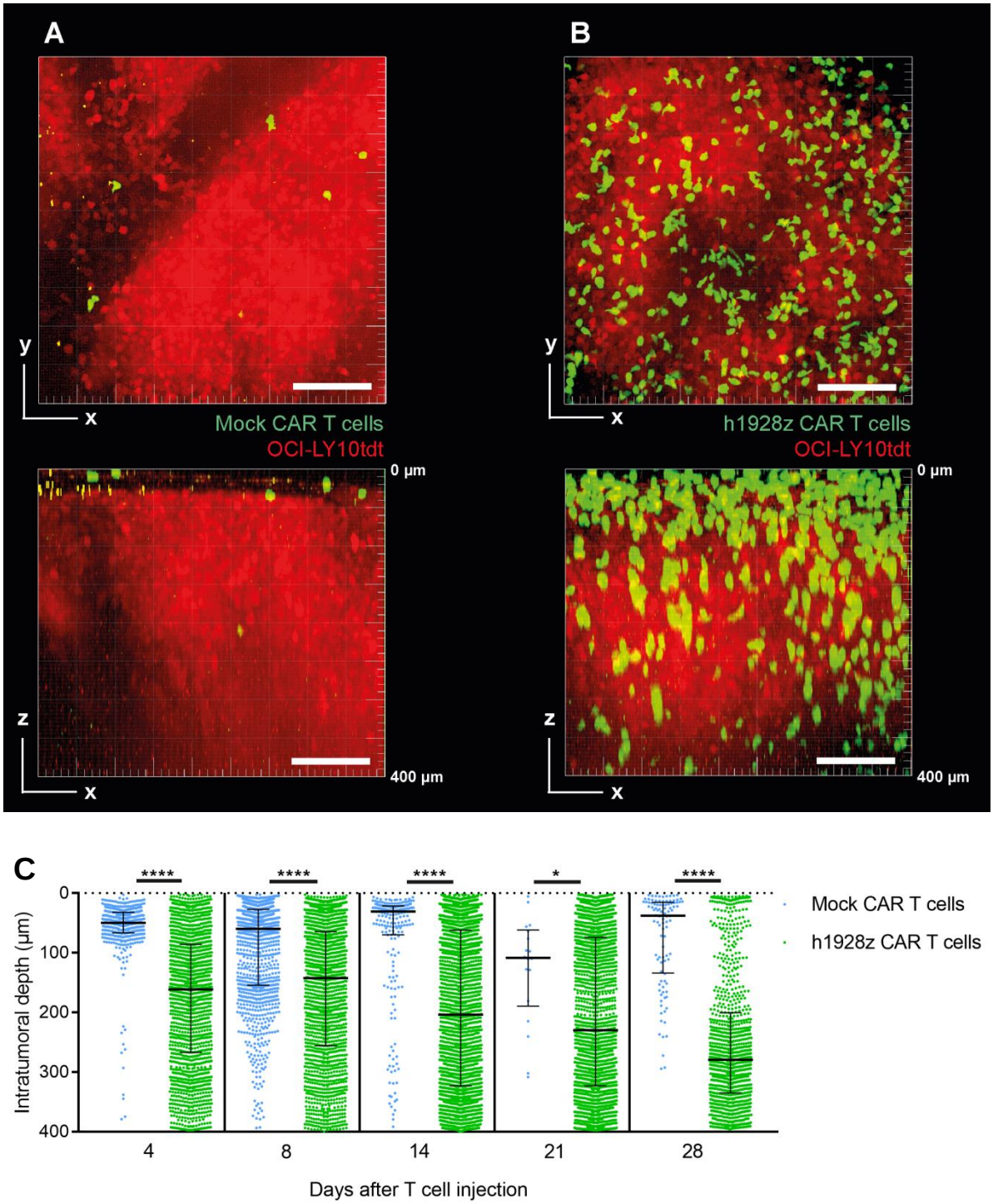

Figure 17 – Intratumoral distribution of h1928z CAR T cells and mock CAR T cells.
h1928z CAR T cells migrate deeper into the tumor compared to mock CAR T cells, who remain located at the tumor border. **A, B**) Examples of maximum intensity projections of intratumoral TPLSM images visualized in parallel (xy) or perpendicular (xz) to the cranial window 14 days after T cell injection. Intracerebral OCI-LY10tdt cells in red, mock CAR T cells (A) and h1928z CAR T cells (B) in green. Scale bars, 100 µm. **C**) Quantification of intratumoral T cell depth as shown in (A, B). Intracerebral depth below meningeal surface of individual intratumoral T cells. Already at day 4 after T cell injection, h1928z CAR T cells accumulated at a deeper intratumoral position compared to mock CAR T cells, the majority of which remained at the subarachnoid space during the whole observation period. After tumor regression (at day 28, 2 of 4 mice in the h1928z CAR group, 0 of 4 mice in the mock CAR group), T cell position at the tumor injection site has not been included in this analysis. Results combined from two three-dimensional regions of interest of 4 mice per group per time point. Pooled data from 4 independent experiments. Median +/- interquartile range. Comparisons were made using the Mann-Whitney *U* test. *$p < 0.05$, ****$p < 0.0001$.

As mock CAR T cells were restricted to the tumor border at the superficial, subarachnoid portion of the tumor, we next assessed the “lateral” (x/y) tumor borders, more than 100µm beneath the most superficial tumor compartment. Indeed, also at the lateral borders of the tumor located in deeper areas, mock CAR T cells accumulated in higher numbers at the borders compared to the tumor core (Figure 18). h1928z CAR T cells, on the other hand showed a homogenous distribution throughout the tumor, with no preferred accumulation at the tumor border or the subarachnoid space (Figure 17, Figure 18).

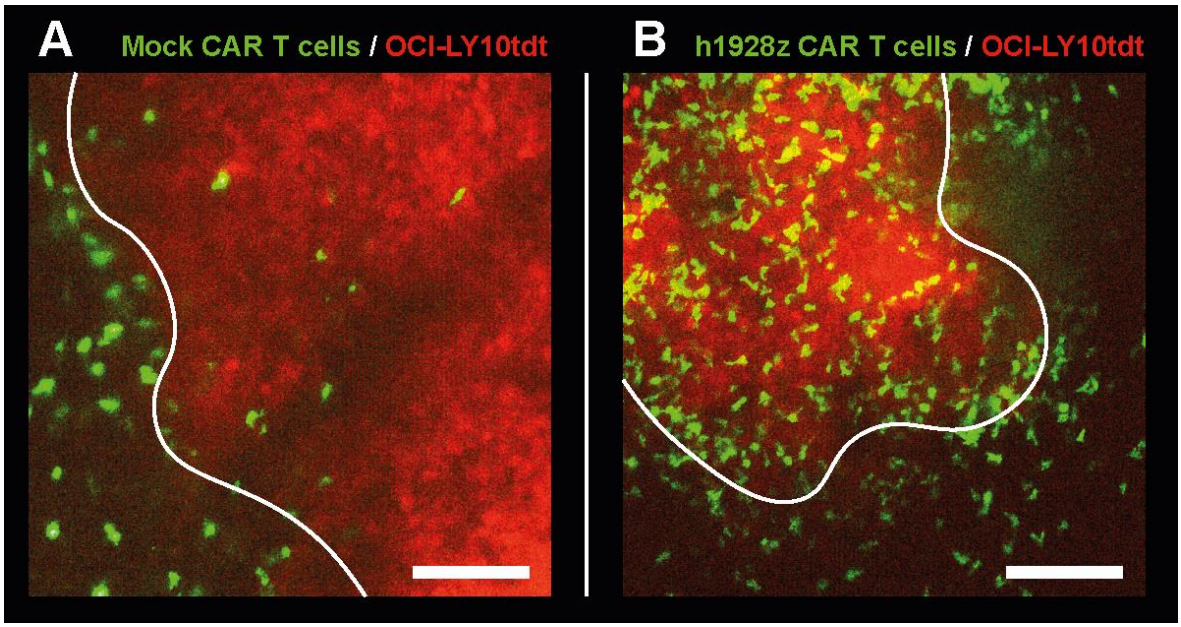

Figure 18 – TPLSM of deeper tumor regions illustrating T cell numbers at the tumor border.
Mock CAR T cells accumulate at the tumor border, whereas h1928z CAR T cells accumulate at the tumor core. Representative TPLSM images showing the border of the solid, intracerebral lymphoma 14 days after T cell injection. Maximum intensity projections of 450 x 450 x 55 µm (x/y/z), 100 µm below the most superficial tumor portion. OCI-LY10tdt cells in red, mock CAR T cells (**A**) or h1928z CAR T cells (**B**) in green. Scale bar, 100 µm.

As we have shown that mock CAR T cells accumulated at the tumor border, the question remained if h1928z CAR T cells similarly accumulated below the subarachnoid (i.e. at the intraparenchymal) compartment in the healthy, contralateral brain hemisphere, which would suggest increased intraparenchymal CAR T cell surveillance without localized inflammatory, chemotactic stimuli.

As expected, also in the contralateral brain hemisphere, mock CAR T cells and h1928z CAR T cells both initially accumulated in equal numbers in the subarachnoid compartment of the brain (Figure 19). Also here, until day 21 after T cell injection, mock CAR T cell number decreased, with only two mock CAR T cells present in the contralateral

subarachnoid space (results pooled from four mice). Conversely, h1928z CAR T cells remained present at a higher density in the subarachnoid space for at least 28 days after T cell injection. Additionally, h1928z CAR T cells migrated into the brain parenchyma in high numbers starting at day 14, suggesting a higher intraparenchymal h1928z CAR T cell immune surveillance compared to mock CAR T cells.

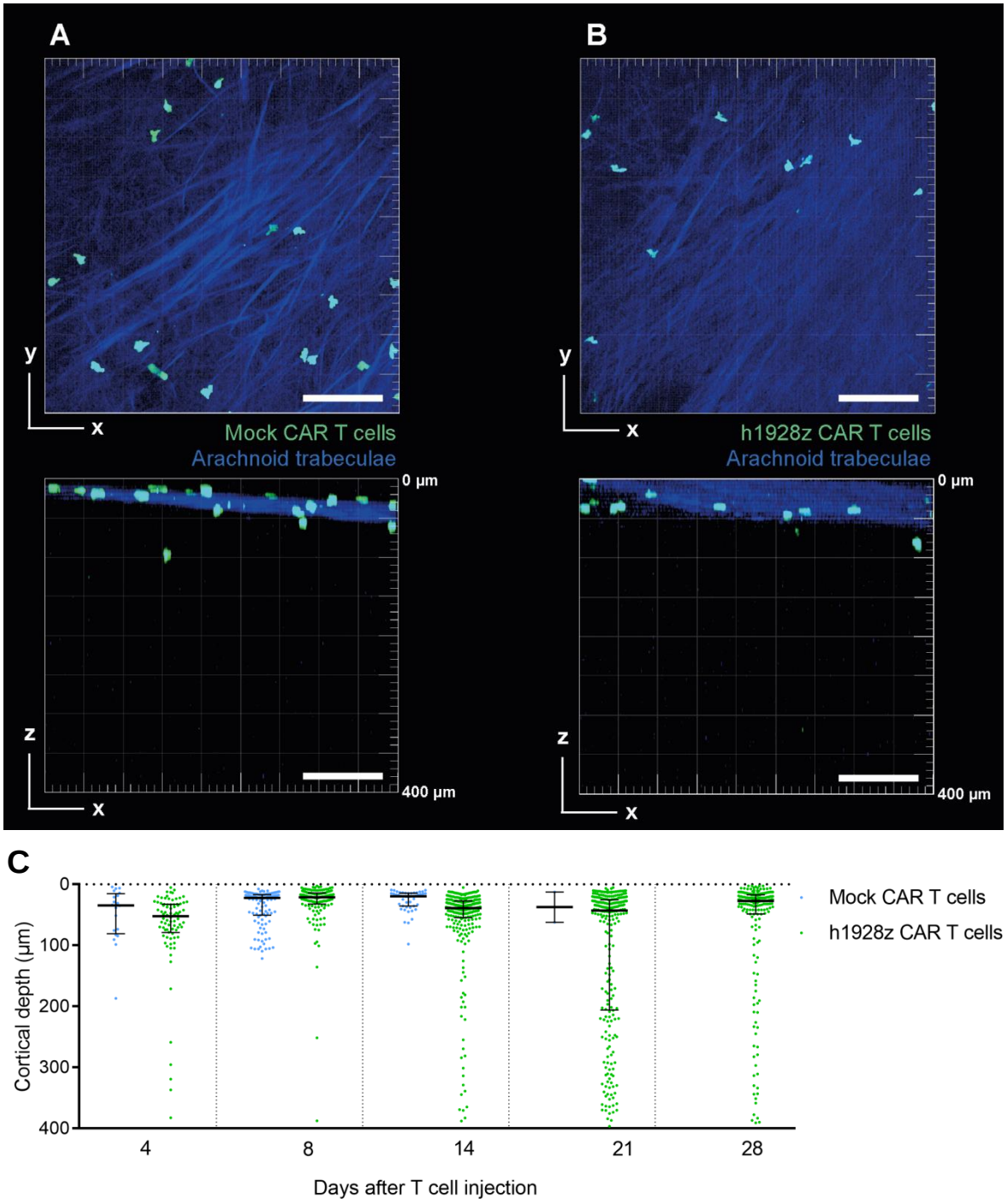

Figure 19 – Contralateral distribution of h1928z CAR T cells and mock CAR T cells.
Contralateral to the tumor injection site, T cells accumulated in the subarachnoid compartment, visualized by second harmonic generation (SHG) signal generated by collagenous arachnoid trabeculae. Also contralaterally, only h1928z CAR T cells persisted for more than three weeks. **A, B**) Examples of cortical three-dimensional two-photon microscopy images visualized in parallel (xy) or perpendicular (xz) to the cranial

window. Mock CAR (A) or h1928z CAR T cells (B) in green, second harmonic generation (SHG) signal of arachnoid trabeculae (collagen) in blue. Scale bars, 100 µm. **C**) Quantification of intratumoral T cell depth as shown in A, B. Cortical depth below meningeal surface of individual T cells. Contralateral to the tumor injection site, both h1928z CAR T cells and mock CAR T cells were visible in the subarachnoid space, where they stayed present during the whole observation period. Starting at day 14, h1928z CAR T cells were also found in the brain parenchyma (below the subarachnoid space, i.e. at least 100 µm below the meningeal surface), while intraparenchymal mock CAR T cells were not visible. On day 28, in 3 of 4 mock CAR T cell mice, the tumors extended into the region contralateral to the tumor injection site, precluding quantification of contralateral mock CAR T cell z-position. Results from the ROI contralateral to tumor injection site of 4 mice per group per time point. Pooled data from 4 independent experiments. Median +/- interquartile range.

To summarize, h1928z CAR T cells invaded the tumor in higher numbers and distributed evenly inside the tumor, where they also persisted for more than 28 days. Also in the brain hemisphere contralateral to the tumor injection site, more h1928z CAR T cells are present inside the brain parenchyma (>100 µm below the meningeal surface). In contrast, mock CAR T cells accumulated at the tumor border in low numbers, persisting for less than 21 days. In the contralateral brain hemisphere, mock CAR T cells were found in the subarachnoid space for less than 21 days, and did not invade the brain parenchyma in significant numbers.

4.6.3 CAR T cell activation and proliferation

So far, we have used TPLSM to delineate intratumoral and contralateral CAR T cell numbers and their distribution over the course of several weeks. Additionally, TPLSM offers the possibility of three-dimensional time lapse movies to analyze individual T cell behavior over time. Analyzing these cell movements at each time point, we sought to compare intratumoral and contralateral T cell velocities. Therefore, we evaluated eventual differences between mock CAR T cell and h1928z CAR T cell migration during tumor growth and regression (Figure 20).

Four days after T cell injection, intratumoral h1928z CAR T cells migrated at a lower velocity compared to intratumoral mock CAR T cells. Also on day 8 after T cell injection, intratumoral h1928z CAR T cell velocity was slower than mock CAR T cell velocity. Interestingly, starting at day 14, median velocity of intratumoral h1928z CAR T cells increased over the following weeks, whereas intratumoral mock CAR T cell velocity stayed low (at very low intratumoral T cell numbers).

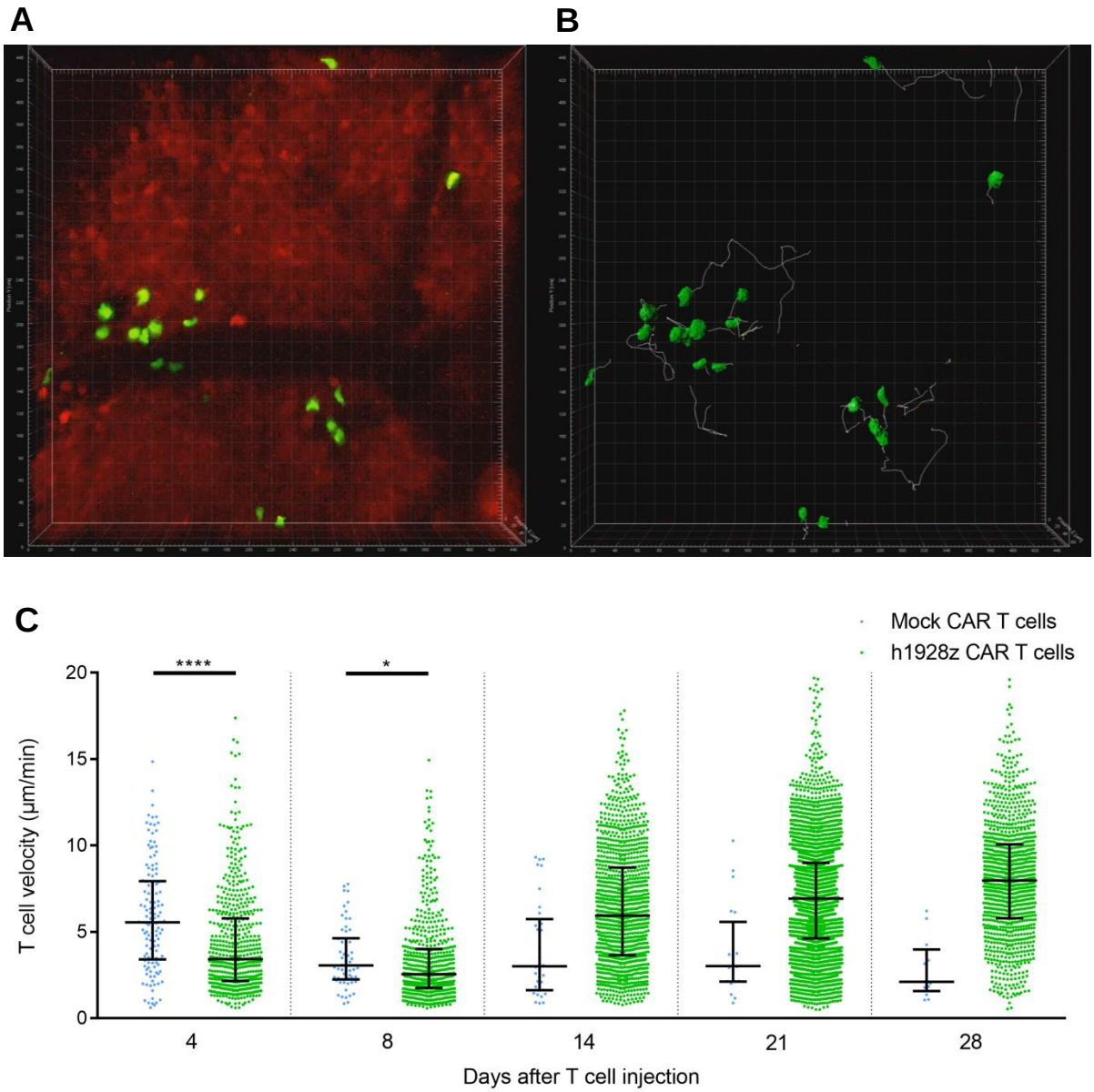

Figure 20 – Intratumoral CAR T cell velocity.
During the first 8 days after injection, h1928z CAR T cells migrated at lower velocities than mock CAR T cells. Starting at day 14, intratumoral h1928z CAR T cell velocity increased, while the absolute number of stationary CAR T cells remained high. Intratumoral mock CAR T cells remained slow (at low numbers). **A, B**) Examples of (A) TPLSM images of OCI-LY10tdt cells (red), h1928z CAR T cells (green) and (B) three-dimensional reconstruction of h1928z CAR T cells (green) with intratumoral migration tracks in white. Time lapse movie of 30 minutes duration, four days after T cell injection. **C)** Quantification of individual, intratumoral T cell velocity of migration tracks as shown in (B). Each dot represents one CAR T cell track. Results from pooled time lapse microscopy movies of at least 30 minutes duration (recording every 30 seconds) per time point, ROI of 450 x 450 x 66 µm (x/y/z) starting at least 100 µm underneath the most superficial tumor compartment. Pooled data from 4 independent experiments. Median +/- interquartile range. Time points with less than 50 intratumoral T cells after pooling were not compared. Comparisons were made using the Mann-Whitney *U* test. **p* < 0.05, *****p* < 0.0001.

In the contralateral hemisphere, h1928z CAR T cells and mock CAR T cells migrate at a similar velocity (Figure 21), indicating that CAR expression does not influence migratory velocity in the absence of the scFv-specific tumor antigen. After regression of all tumor

cells at the tumor injection site at day 28 and 42 after T cell injection, h1928z CAR T cells resumed migratory velocities similar to contralateral h1928z CAR T cell velocities.

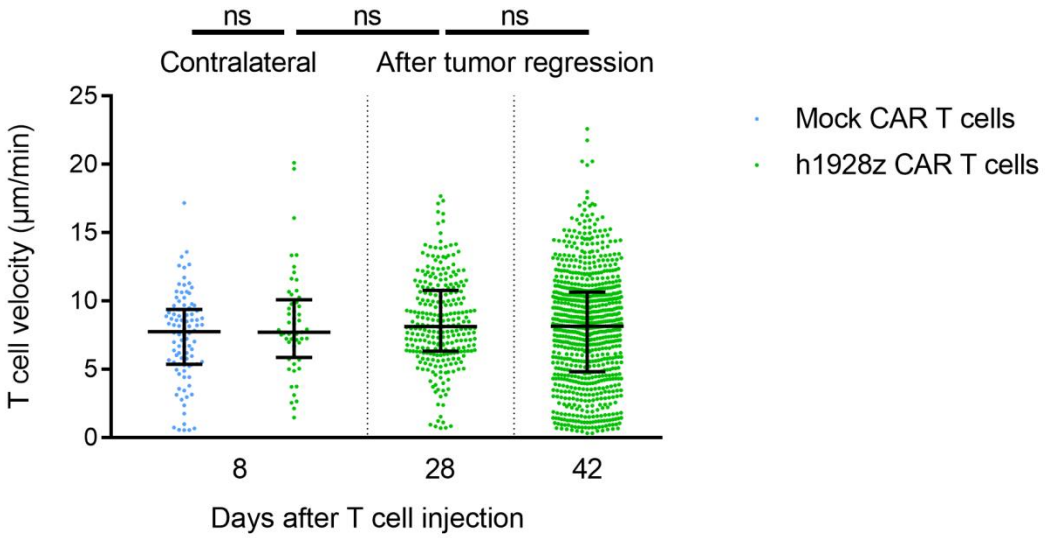

Figure 21 – Contralateral and cortical CAR T cell velocities after tumor regression.
In the contralateral hemisphere, h1928z CAR T cells and mock CAR T cells migrated at similar velocities. After tumor regression, h1928z CAR T cells at the tumor injection site resumed velocities similar to contralateral velocities. Individual extratumoral T cell velocity. Results from pooled time lapse microscopy data of at least 30 minutes per time point. Pooled data from 4 independent experiments. Median +/- interquartile range. Comparisons were made using the Mann-Whitney *U* test. ns = not significant.

Intratumoral CAR T cell number could theoretically be increased by increased migration, longerer persistence, or by increased CAR T cell proliferation. To evaluate intratumoral proliferation rates, time lapse movies were manually analyzed for mitotic cell divisions. Interestingly, in the h1928z CAR T cell group, several intratumoral mitoses were visible (Figure 22). In contrast, during all time lapse videos analyzed, no tumor cell mitosis was visible, suggesting that intratumoral CAR T cell proliferation rates exceeded the proliferation rate of the intracranial PCNSL cells.

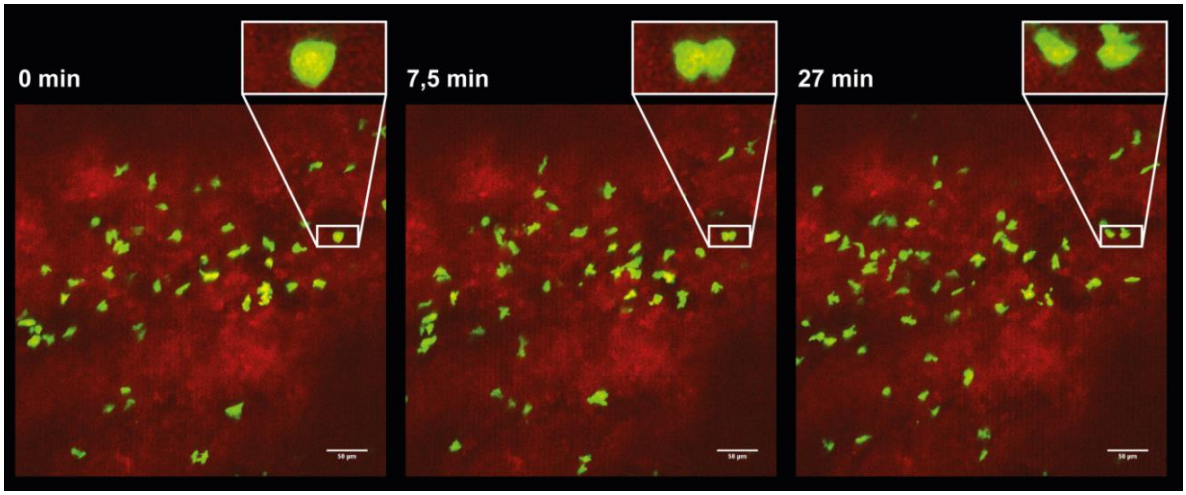

Figure 22 – Example of intratumoral h1928z CAR T cell mitosis *in vivo*.
TPLSM time lapse movie of 30 minutes duration. Maximum intensity projections of 450 x 450 x 66 µm (x/y/z), image acquisition every 30 seconds. Scale bars, 50 µm.

4.6.4 Anti-tumor cytotoxicity, leading to tumor regression

Intracerebral tumor volume can be approximated by calculation of a sphere using the tumor diameters visible through the cranial window via epifluorescence microscopy. Following stereotactic injection of CAR T cells, the tumor volume of the mock CAR T cell group increased significantly compared to the h1928z CAR T cell group during an observation period of 42 days after tumor implantation (Figure 23).

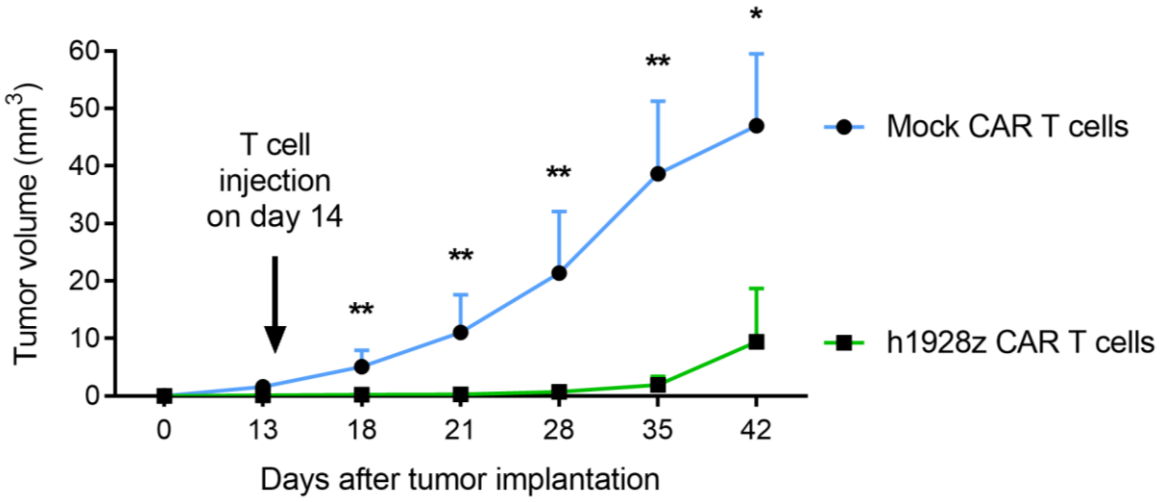

Figure 23 – Intracranial PCNSL growth after injection of CAR T cells.
Mice receiving mock CAR T cells showed increased tumor volume at all time points compared to mice after h1928z CAR T cell injection. 14 days after PCNSL implantation, $5x10^4$ h1928z CAR T cells or mock CAR T cells were injected at a distance of 1 mm posterior to the tumor. Mean +/- s.e.m. Comparisons were made using the Mann-Whitney *U* test. *$p < 0.05$, **$p < 0.01$, n = 5 mice (mock CAR group) or 6 mice (h1928z CAR group).

Furthermore, after injection of h1928z CAR T cells, 4 of 6 mice (66,7%) showed complete regression of these large, established PCNSL, while one mouse developed symptoms albeit a very small sized tumor (due to intraventricular tumor growth; Figure 24). Only 1 of these 6 mice had progressive tumor growth despite numerous intratumoral h1928z CAR T cells. After injection of mock CAR T cells, 4 of 5 mice (80%) developed large, intracerebral PCNSL (Figure 24). Interestingly, injection of mock CAR T cells led to complete regression of large established PCNSL in 1 out of 5 mice (20%), suggesting potential anti-tumor activity of activated mock CAR T cells.

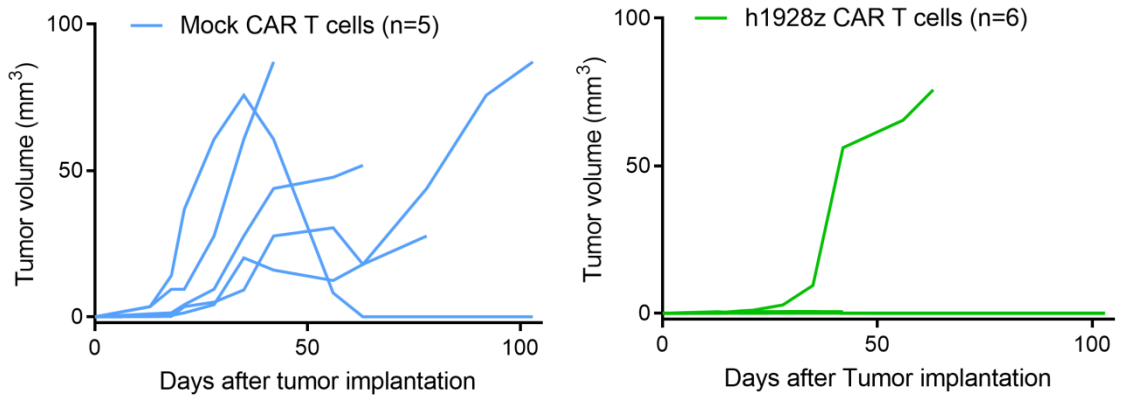

Figure 24 – Individual intracerebral tumor volume after mock CAR / h1928z CAR T cell injection. Tumor volume of the same mice seen in **Figure 23**. In the mock CAR T cell group (n = 5, tumor volume in blue), tumors continued to grow in 4 of 5 mice. In 1 mouse, the tumor completely regressed with no visible tumor cells for more than 100 days, indicating potential antitumor activity of murine mock CAR T cells against human OCI-LY10-tdt cells *in vivo*. After h1928z CAR T cell injection (n = 6, tumor volume in green), 4 of 6 tumors completely regressed for the observation period, one tumor stayed at a small size, while only one tumor progressed. Data pooled from 6 independent experiments.

4.6.5 Long term persistence of CAR T cells

Successful anti-tumor immunotherapy with CAR T cells not only leads to complete tumor regression, but ideally also results in long term persistence of tumor-specific CAR T cells, indicating higher therapeutic potential. Indeed, intracerebral h1928z CAR T cells remained visible for up to 159 days after h1928z CAR T cell injection, without recurrence of visible tumor cells (Figure 25, Figure 26).

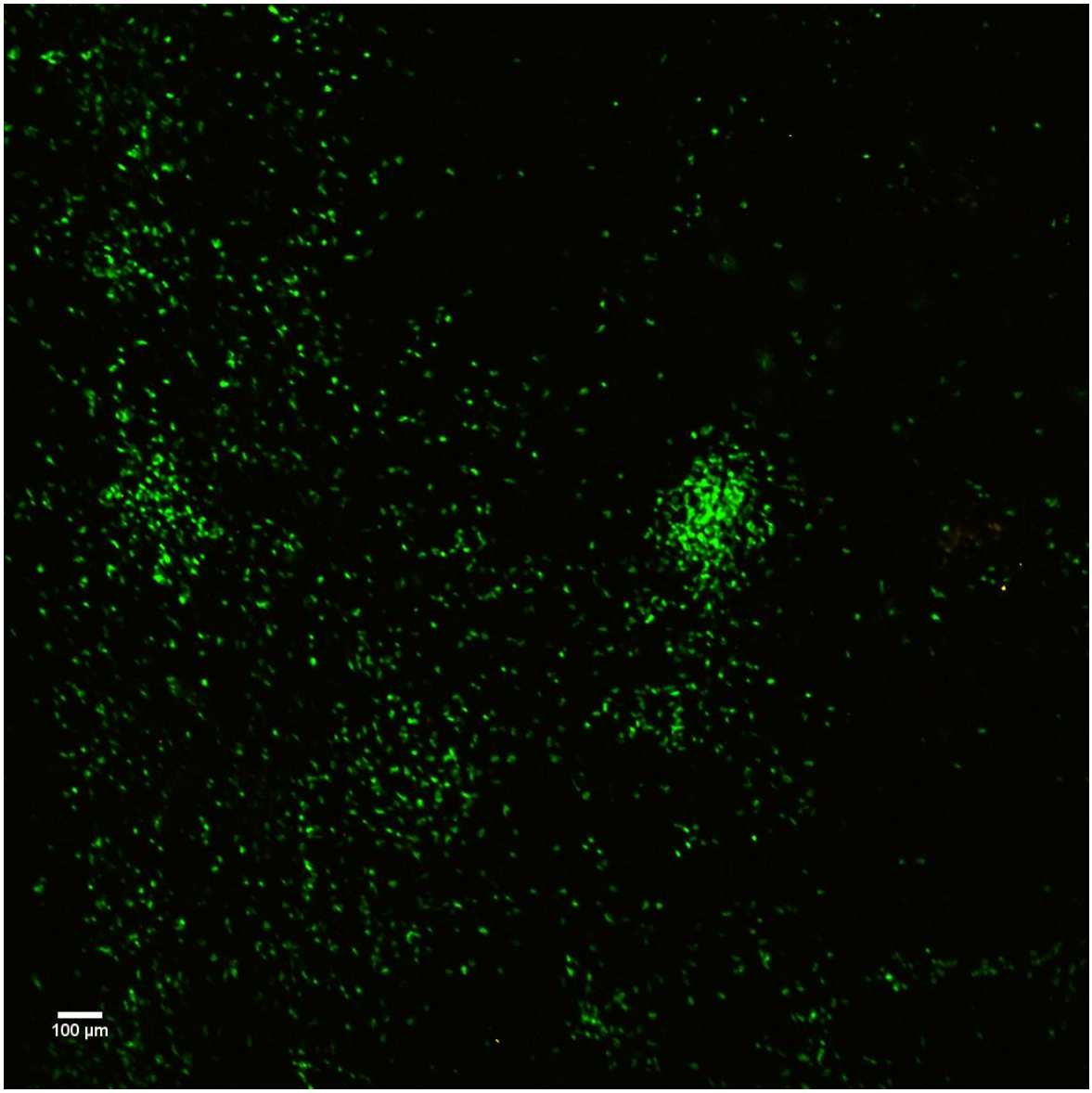

Figure 25 – TPSLM of intracranial h1928z CAR T cell persistence.
h1928z CAR T cells persisted intracranially for more than 98 days after tumor regression. 10 weeks after tumor regression (same mouse as in **figure 15**), no tumor cells were visible, while h1928z CAR T cells (in green) were visible across the whole brain surface. Scale bar, 100 µm.

To increase therapeutic efficacy, long-term persistence of intracerebral CAR T cells would also lead to systemic presence of these cells, thereby extending the immunosurveillence against distant metastases or newly arising tumor cells otherwise escaping the intracerebral CAR T cell induced immune response. 28 days after stereotactic h1928z CAR T cell injection, numerous CAR T cells became visible inravascularly during intravital epifluorescence imaging. Importantly, the number of intravascular h1928z CAR T cells, as well as the fraction of mice showing intravascular presence of h1928z CAR T cells further increased over the following days & weeks. These intravascular T cells remained visible,

similar to intracerebral CAR T cells, for up to 159 days after intracranial h1928z CAR T cell injection (Figure 26).

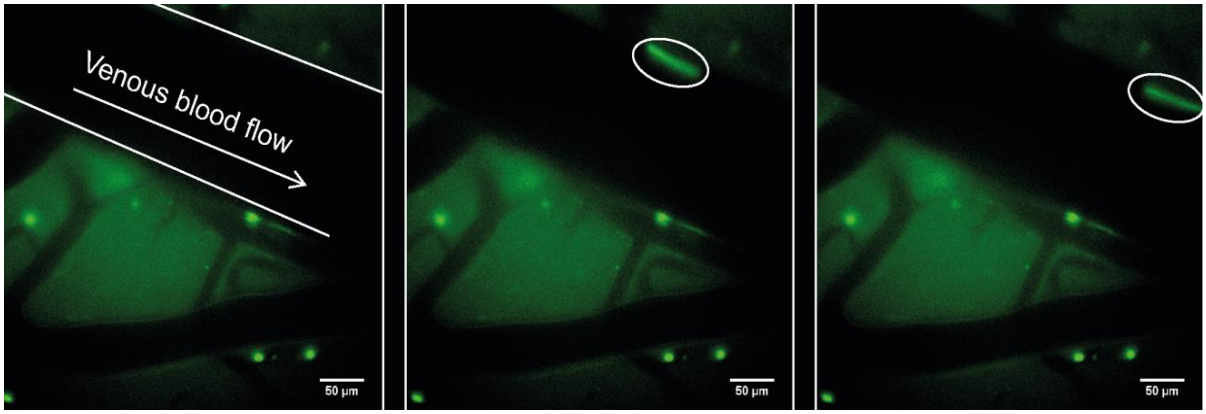

Figure 26 – Epifluorescent imaging of intravascular and intracerebral h1928z CAR T cells.
159 days after intracranial h1928z CAR T cell injection, intravascular h1928z CAR T cell were seen intravascularly (one example indicated with a circle) as well as intracerebrally. 3 consecutive frames acquired with a CCD camera and epifluorescent illumination. 25ms between each frame. Scale bar, 50 µm. Same mouse as in **figure 15** and **25**.

4.7 Histopathological validation

Although the surgical removal of the dura mater during implantation of the cranial window was done four weeks before CAR T cell injection, procedure-related effects on intracerebral CAR T cell behavior cannot be completely ruled out, especially concerning the leptomeningeal position of injected CAR T cells. Therefore, we wanted to validate our results, in another experiment without implantation of a chronic cranial window. Again, 14 days after stereotactic tumor implantation CAR T cells were injected at a distance of 1 mm posterior to the tumor injection site. Although this time, we restricted the therapeutic dose to only $2x10^4$ h1928z CAR T cells or mock CAR T cells (compared to $5x10^4$ in the experiments above). 28 days after T cell injection, the mice were perfused and the brains were analyzed for tumor size and T cell density by immunofluorescence. Similar to the results obtained by TPLSM, immunofluorescence showed development of big PCNSL in mice treated with mock CAR T cells (Figure 27). These tumors show intraventricular dissemination (A, B), contact to the subarachnoid compartment (C), and very low intratumoral mock CAR T cell density (C, D), corroborating the results obtained by TPLSM.

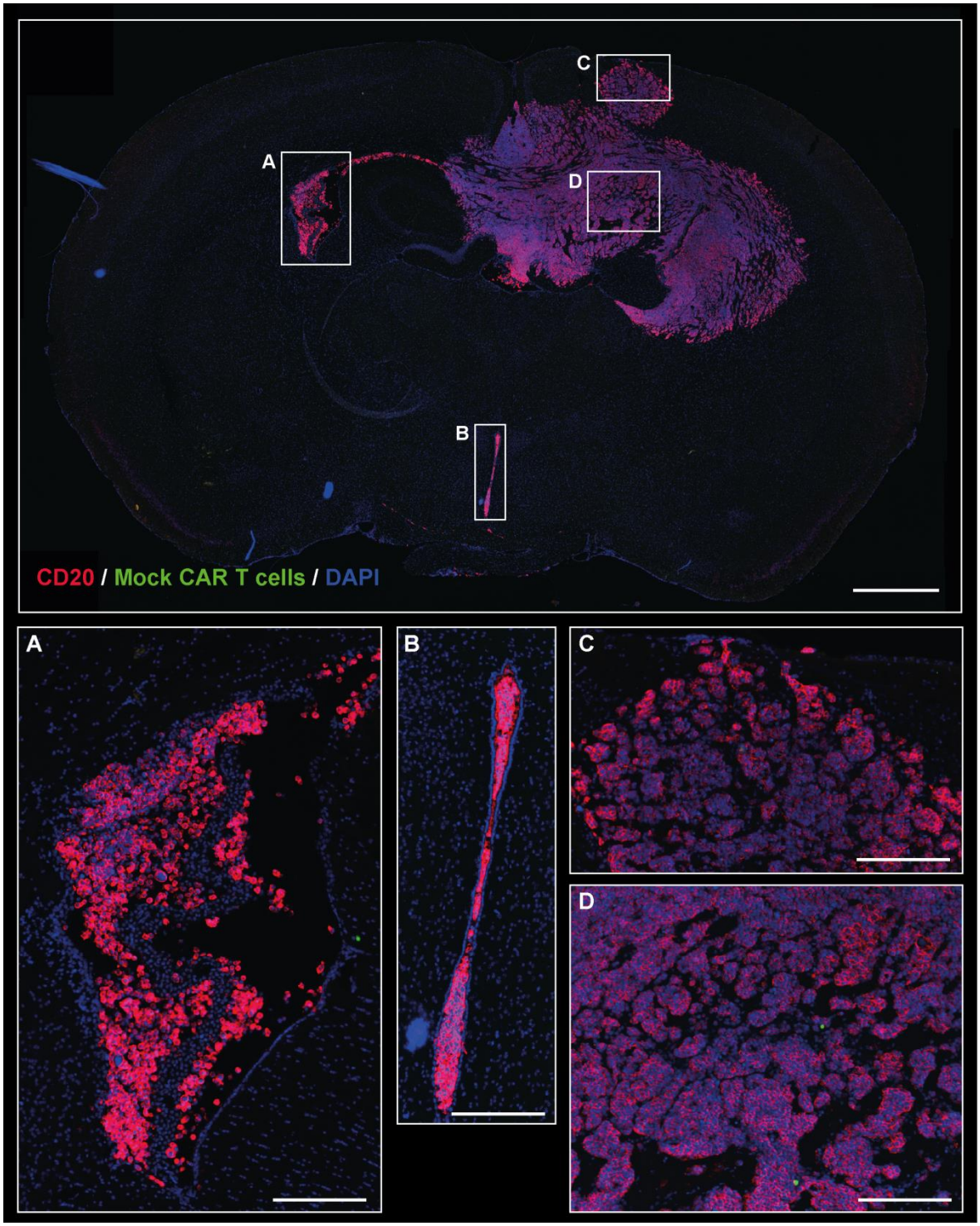

Figure 27 – Immunofluorescence of PCNSL 28 days after mock CAR T cell injection.
Intracortical injection of mock CAR T cells led to development of a big, intraparenchymal PCNSL with intraventricular tumor dissemination and low intratumoral T cell density. 14 days after stereotactic intracortical implantation of 2.5 x 10^5 OCI-LY10tdt cells, mock CAR T cells were injected at a distance of 1 mm posterior to the tumor injection site. 28 days after T cell injection (42 days after tumor injection), a big cortical tumor with intraventricular growth **(A)** and ventricular dissemination **(B)** developed with absent **(C)** or low **(D)** intratumoral mock CAR T cell numbers. Representative immunofluorescence of OCI-LY10tdt cells with CD20 immunostaining (red), eGFP signal (green) and DAPI nuclear staining (blue). Scale bars, 1 mm (big panel) or 200 µm (A, B, C, D).

In contrast, 28 days after injection of h1928z CAR T cells, PCNSL size was smaller (Figure 28), showing dense tumor infiltration by h1928z CAR T cells (B). Interestingly, h1928z CAR T cells additionally showed intraventricular and subependymal dissemination (A, C), another important compartment for cerebral immune surveillance. Also, numerous h1928z CAR T cells were found along the leptomeninges (D), further corroborating the results obtained by TPLSM, where numerous 1928z CAR T cells were found within the subarachnoid space. This extent of h1928z CAR T cell dissemination was quite surprising, considering the thickness of the cryosections of only 15 µm.

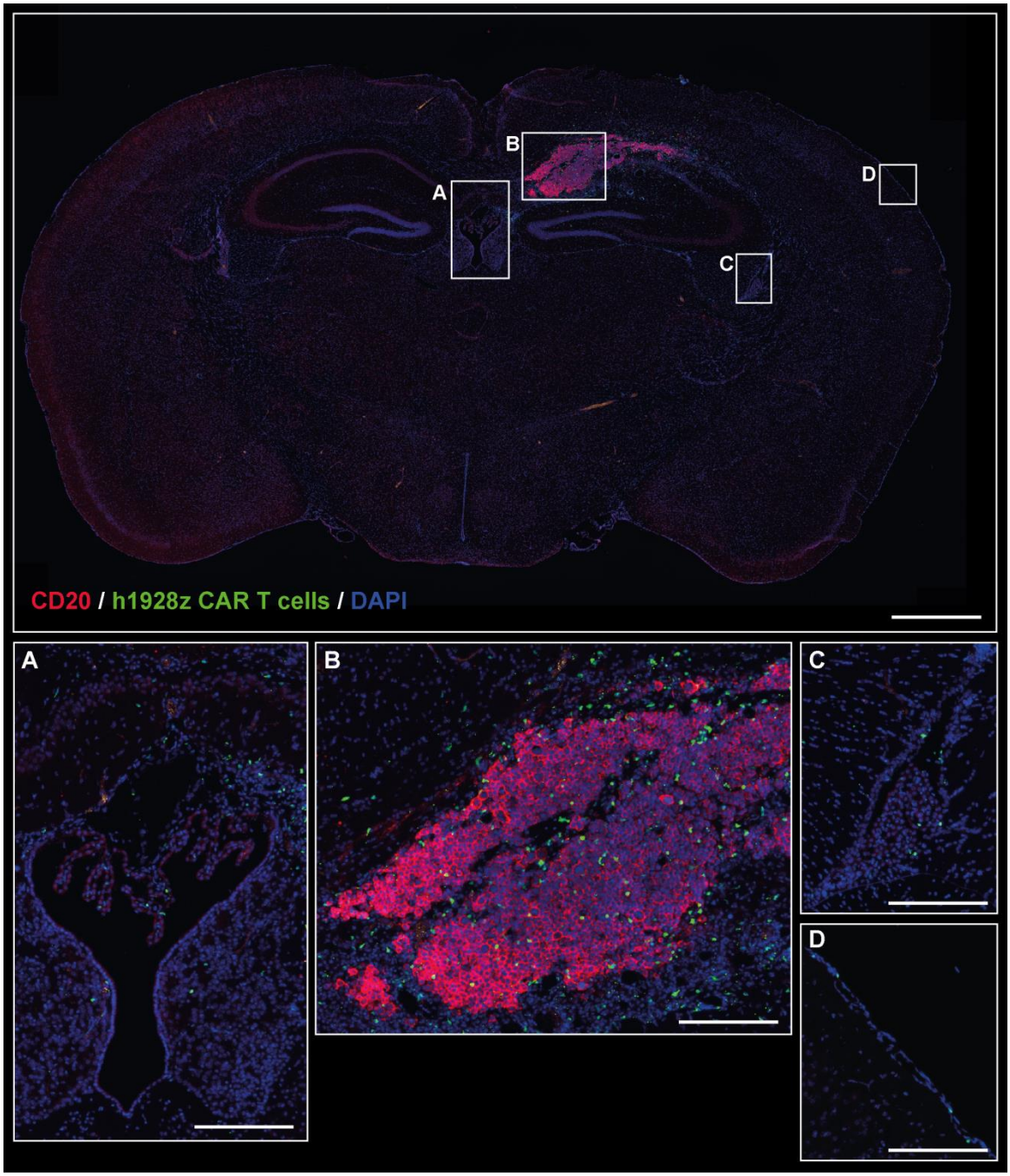

Figure 28 – Immunofluorescence of PCNSL 28 days after h1928z CAR T cell injection.
Intracortical injection of h1928z CAR T cells led to regression of PCNSL with high intratumoral h1928z CAR T cell numbers. 14 days after stereotactic intracortical implantation of 2.5x 10^5 OCI-LY10tdt cells, h1928z CAR T cells were injected at a distance of 1 mm posterior to the tumor injection site. 28 days after T cell injection (42 days after tumor injection), only a small, subcortical tumor developed with a high intraventricular **(A, C)** and intratumoral h1928z CAR T cell density **(B)**. Note the subependymal **(A, C)** and meningeal **(D)** position of patrolling h1928z CAR T cells. Representative immunofluorescence of OCI-LY10tdt cells with CD20 immunostaining (red), eGFP signal (green) and DAPI nuclear staining (blue). Scale bars, 1 mm (big panel) or 200 µm (A, B, C, D).

To quantify tumor volume, we delineated the tumor area for each 15 µm thick cryosection every 495 µm throughout the whole brain. In the mock CAR T cell group, 5 out of 7 mice developed big, cerebral lymphomas, while 2 out of 7 mice had no cerebral tumors (Figure 29, blue). In the h1928z CAR T cell group, only 1 out of 7 mice showed big cerebral lymphoma growth, while 2 of 7 mice showed very small tumors, and 4 of 7 mice showed no intracerebral lymphoma growth (Figure 29, green).

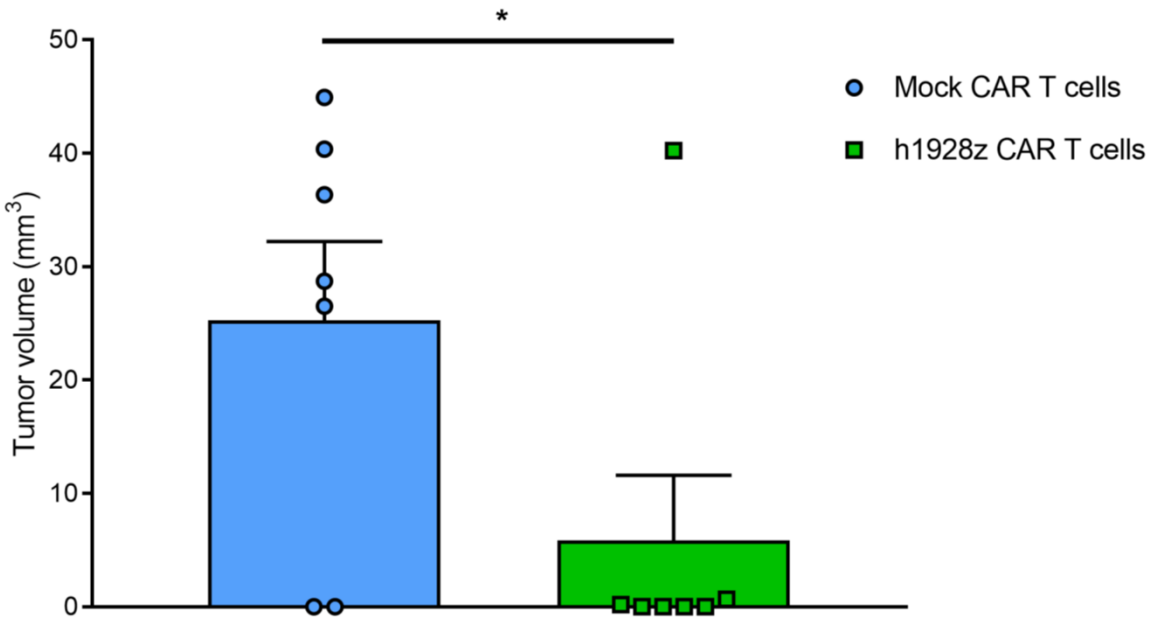

Figure 29 – Tumor volume measured via immunofluorescence.
Treatment with intracranial h1928z CAR T cells reduced intracerebral tumor volume. 14 days after intracranial tumor injection, h1928z CAR T cells or mock CAR T cells were stereotactically injected at a distance of 1 mm posterior to the tumor. 28 days after T cell injection (42 days after tumor implantation), 15 µm thick cryosections every 495µm were immunofluorescently analyzed for tumor area and tumor volume calculated accordingly. Wilcoxon test. *$p < 0.05$. n = 7 mice per group.

Comparing intratumoral CAR T cell numbers in all mice with intracranial PCNSL still present, mice treated with h1928z CAR T showed consistently higher intratumoral CAR T cell density compared to mice treated with mock CAR T cells (Figure 30).

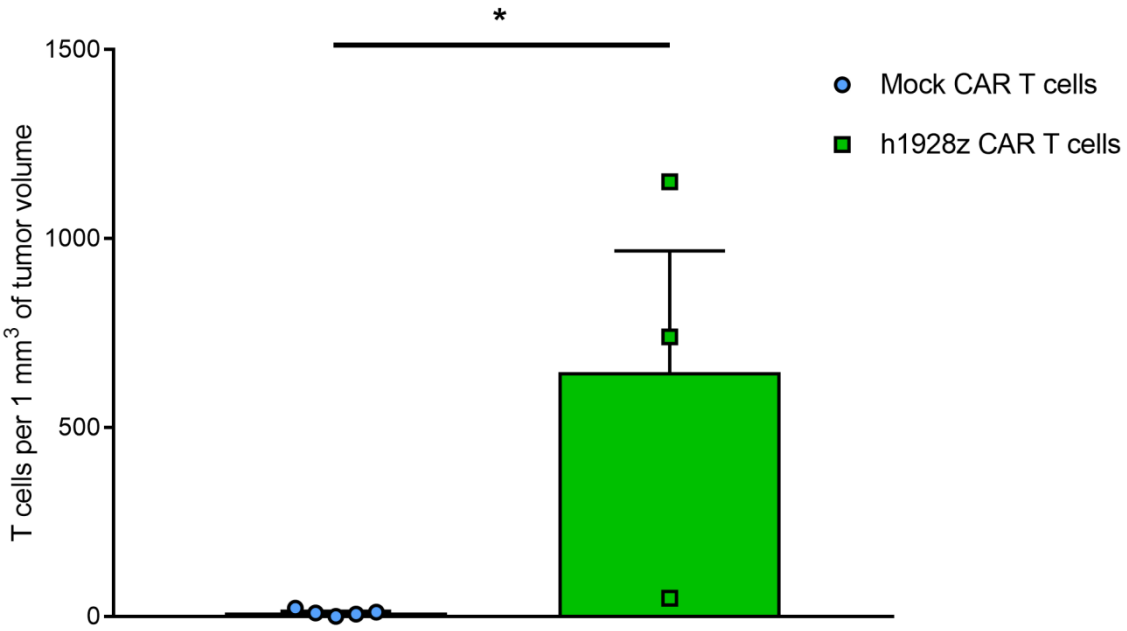

Figure 30 – Intratumoral T cell number.
Intratumoral CAR T cell number was higher in mice treated with h1928z CAR T cells compared to mice treated with mock CAR T cells. All mice with visible intracranial tumor cells (mock CAR T cells, in blue, n = 5 of 7, h1928z CAR T cells in green: n = 3 of 7) were included. Comparison was made using the Mann-Whitney *U* test. $*p < 0.05$.

In mice, tumor growth eventually led to body weight loss, which is a sensitive marker for neurological symptoms in animal models of cerebral cancer. Stereotactic T cell or tumor cell implantation under general anesthesia leads to initial body weight loss, which is usually regained during postoperative reconvalescence. Decreased regain of body weight can therefore be used as a sensitive marker for impaired neurological wellbeing due to tumor growth or due to neurotoxic side effects of adoptive cell therapy.

In our experiment, in which the experimental end point (42 days after tumor implantation) was chosen before the development of neurological symptoms due to tumor growth was expected, body weight of both groups was compared (Figure 31). There was no difference in body weight change after CAR T cell therapy, suggesting that neither tumor growth nor CAR T cell therapy led to the development of neurological symptoms.

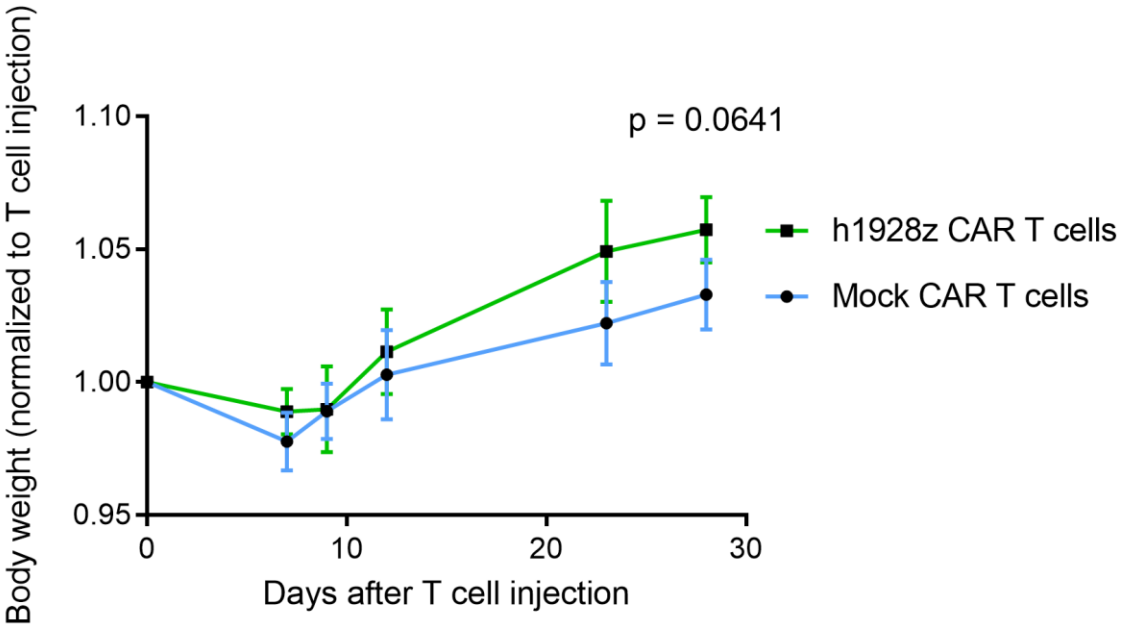

Figure 31 – Body weight after intracranial CAR T cell injection.
Initially after stereotactic CAR T cell injection, mice of both groups had slightly decreased body weight. During 28 days after CAR T cell treatment, no difference in body weight was seen between groups. Mann-Whitney *U* test of body weight at day 28 after T cell injection, normalized to day 0. n = 7 mice per group.

To validate the observation that CAR T cells were able to enter the blood circulation (Figure 26), we sequentially performed blood sampling to quantify intravascular CAR T cells. Already 5 days after stereotactic CAR T cell injection, h1928z CAR T cells were visible in the blood circulation, albeit at low numbers, whereas no mock CAR T cells were found intravascularly (Figure 32). At day 10 after injection, 4 of 5 mice had h1928z CAR T cells present intravascularly, compared to 0 of 5 mock CAR T cells. At day 25, in both groups receiving h1928z CAR T cells and mock CAR T cells intravascular CAR T cells were present. Therefore, h1928z CAR T cells were able to intravasate faster compared to mock CAR T cells.

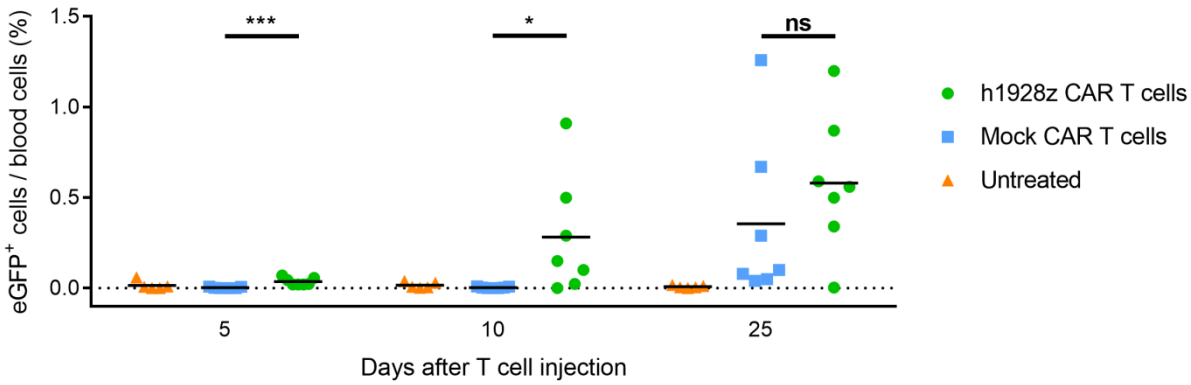

Figure 32 – Flow cytometry of intravascular CAR T cells.
Already 5 days after intracranial CAR T cell injection, intravascular h1928z CAR T cells were present in low numbers. During the next 5 days, this number further increases, and at day 25 also intravascular mock CAR T cells became visible. $eGFP^+$ CAR T cells as a proportion of total blood cells after exclusion of dead cells and $CD19^+$ cells. h1928z CAR T cells and mock CAR T cells: n = 7 per group, untreated: n = 5. Comparison was made using the Mann-Whitney *U* test. **p* < 0.05, ****p* < 0.001. ns = not significant.

As CAR T cells were able to enter into and persist inside the blood stream, one open question remained regarding if these circulating CAR T cells are able to infiltrate and surveil secondary lymphoid organs (e.g. lymph nodes), similar to physiological T cells. Intriguingly, in brain-draining superficial cervical lymph nodes, h1928z CAR T cells were found numerously. Additionally, even in non-draining lymph nodes (inguinal lymph nodes, Figure 33), h1928z CAR T cells were found in high numbers, confirming that h1928z CAR T cells are able to reach distant secondary lymph organs via the blood stream. Mock CAR T cells were present at lower numbers in non-draining lymph nodes, suggesting that lymph node entry is limited without CAR activity.

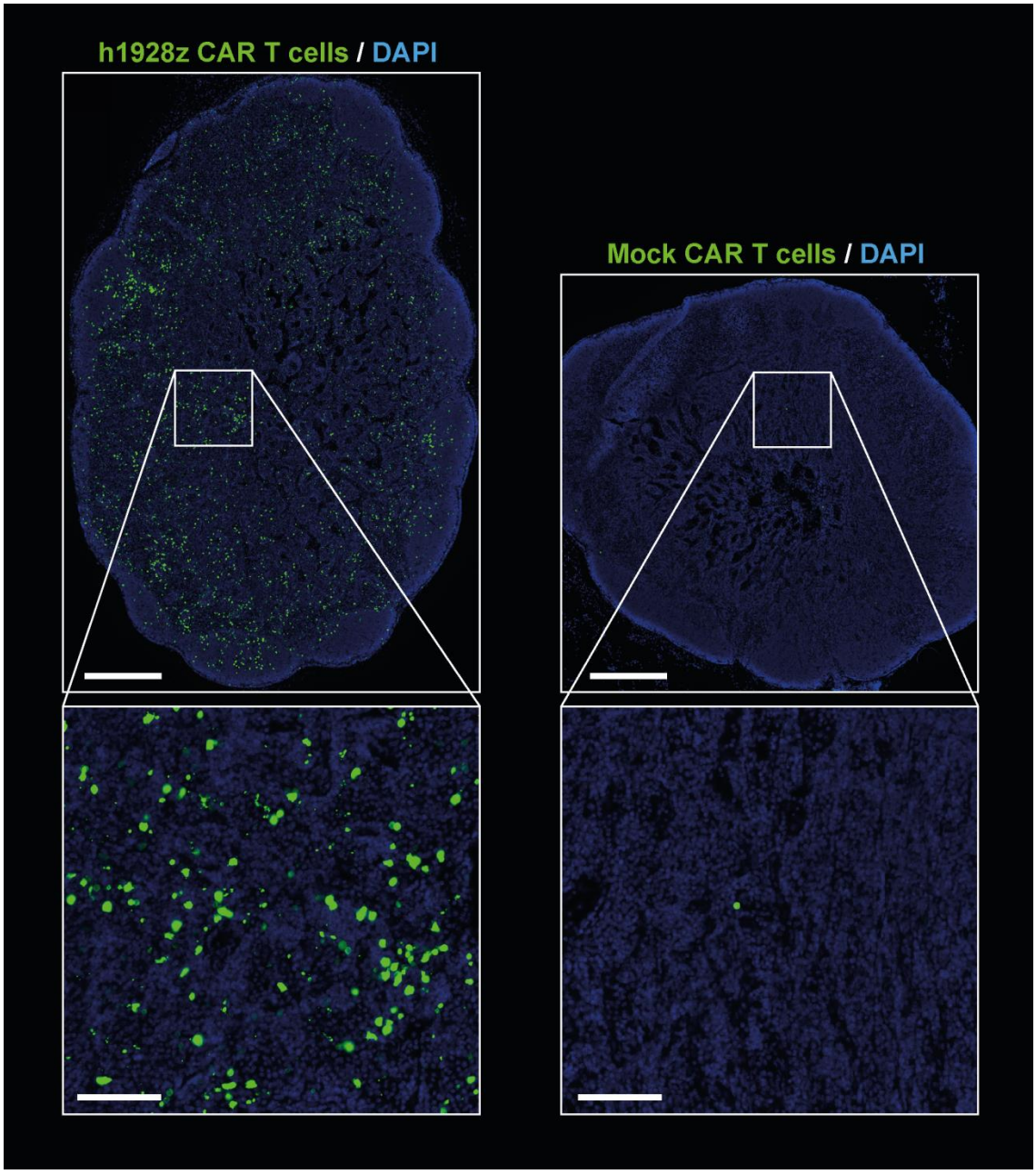

Figure 33 – h1928z CAR T cells invade lymph nodes in high numbers.
28 days after CAR T cell injection, h1928z CAR T cells were found numerously inside the non-draining inguinal lymph nodes. Conversely, mock CAR T cells were only sparsely seen in the non-draining lymph nodes. Representative cryosection after DAPI staining (blue), $eGFP^+$ signal (green). n = 7 per group.

5 Discussion

5.1 Mouse model

Most novel cancer treatments have been developed with the help of preclinical cancer models. Already more than 100 years ago, animal models of cancer and other diseases have successfully been used to deepen our understanding of cancer (Paget 1889; Power 1895), and have since become a mainstay of oncological research. Many cancer treatments in use today are the result of rigorous preclinical *in vivo* experiments. Translating insights and therapeutic successes from preclinical trials to human patients remains challenging (Hackam and Redelmeier 2006; Kaelin 2017), but valid animal models often remain the best chance to improve medical care, especially for rare tumors like PCNSL.

Here, we created a novel mouse model of PCNSL, closely mimicking human PCNSL growth. Human PCNSL shows a highly infiltrative growth pattern, usually characterized as a „whole brain disease“ (Lai, Rosenblum, and DeAngelis 2002). On magnetic resonance imaging (MRI), these lesions typically show close contact to the subarachnoid space (Haldorsen, Espeland, and Larsson 2011; Kuker et al. 2005). Besides this infiltrative growth pattern, perivascular growth of lymphoma cells around preexisting blood vessels is another characteristic feature of this disease, present in 87% of patients (He et al. 2013). In our animal model, stereotactic implantation of human DLBCL cells into the cortex of nude mice leads to the development of intracerebral lesions with infiltrative growth pattern, meningeal dissemination and perivascular growth, similar to human PCNSL (Figure 10). This finding is in line with reports of other rodent models of PCNSL after intracerebral implantation of human lymphoma cells (Kadoch et al. 2009; Montesinos-Rongen et al. 2013). However, our model presents three main advantages compared to already existing animal models of PCNSL.

First, patients with PCNSL most often present with lesions after they become symptomatic, when these tumors already have a diameter of several mm. Lesions of this size already exhibit a peculiar stromal microenvironment, including changes in the expression of immunosuppressive cytokines, lower pH and oxygen pressures, and an impaired blood brain barrier. In preclinical tumor models, many of these features become present only two weeks after orthotopic tumor implantation (Yu et al. 2006), when tumors become exceptionally difficult to eradicate in mice. Therefore, an ideal animal model not

only incorporates histopathological characteristics of human PCSNL, but additionally shows a time window long enough to allow for establishment of big tumors with accordingly altered microenvironment before therapy effects are being validated.

In most preclinical models evaluating therapeutic effects on PCNSL, beneficial results were obtained in experiments starting therapy between 1 (Mineo et al. 2008) and 4 days after tumor implantation (Kadoch et al. 2009). To the best of our knowledge, only two studies exist, in which treatment of PCNSL was beginning more than 14 days after tumor implantation (Jahnke et al. 2009; Muldoon et al. 2011), and these have been conducted in rats. However, only one of them was able to report complete remission of established intracerebral tumors with long term survival of some mice (of more than 60 days). This trial evaluated the effect of the anti-CD20 antibody rituximab, a monoclonal antibody often added to current PCNSL treatment regimens (Batchelor et al. 2011; Fritsch et al. 2011; Birnbaum et al. 2012; Ferreri et al. 2016), illustrating the translational relevance of successful preclinical cancer models.

To the best of our knowledge, this is the first study conducted in mice, in which therapy started 14 days after intracerebral tumor implantation was able to show complete regression of large, established PCNSL.

Second, animal models often use highly immunodeficient non-obese diabetic (NOD) / severe combined immunodeficiency (SCID) models, in which mature T cells, B cells are missing, and NK cell function is impaired, or an even more immunodeficient mouse model, NOD/SCID gamma (NSG) mice. In these mice, mature T cells and B cells are missing, with absent NK cell function and additional deficiencies exist in macrophage/monocyte and dendritic cell function, multiple cytokine signaling pathways and an absent complement cascade (Ishikawa et al. 2005). Obviously, in an animal model mimicking a disease as complex as cancer, the absence of any part of the complex immune environment can have large effects on immunotherapy. For example, parts of the complement cascade have been reported as a contributor to immunotherapy in PCNSL (Kadoch et al. 2014), implicated in CXCL12-induced chemotaxis (Honczarenko et al. 2005) and described as a modulator of the anti-tumor response by suppressing T cell function (Markiewski et al. 2008). Although highly immunodeficient mice like the NOD/SCID or the NSG mouse models usually show more consistent engraftment of human tumors, the high immunodeficiency has a potential impact on immunotherapeutic responses. In our Foxn1$^{nu/nu}$ mouse model, the absence of a functional thymus epithelium leads to the lack of mature, functional T cells, with the remaining functions of B cells and the innate immune system, NK cells, and the complement cascade intact. As there is currently no murine B cell lymphoma cell line available commercially, the Foxn1$^{nu/nu}$

mouse is the least immunodeficient mouse model available to specifically evaluate the function of murine, anti-human CD19 CAR T cells in lymphoma xenografts.

Third, combination of this animal model with a well-tolerated chronic cranial window and TPLSM enabled us to analyze tumor growth repeatedly and in unprecedented detail. Using this model, we were able to analyze CAR T cell function during the initial and later stages of PCNSL regression in the same mice. Herein, we showed the enormous potential of h1928z CAR T cells against PCNSL *in vitro*, *ex vivo* and *in vivo*.

5.2 Tumor infiltration and distribution

In adoptive cell therapy, the first step towards tumor eradication is tumor infiltration, overcoming a multitude of physical and immunological barriers. So far, the most remarkable success of CAR T cells has been achieved in semiliquid hematological malignancies residing in the bone marrow, a niche easily accessible for intravascular T cells. For infiltration of solid tumors, CAR T cells face three additional barriers: migration towards the tumor, penetration into the tumor and combatting the immunosuppressive tumor microenvironment (Yong et al. 2017; Newick et al. 2017; Newick, Moon, and Albelda 2016). Until now, no *in vivo* visualization exists on how CAR T cells enter and overcome these barriers within solid tumors.

T cells are equipped with motility patterns optimized to enhance the probability of finding their cognate antigen. These patterns combine random movement (Brownian-like and Levy-like random walks) with chemotaxis (Krummel, Bartumeus, and Gerard 2016). Upon initial activation in the lymph nodes, T cells upregulate chemokine receptors to scan peripheral tissues to find their antigen, a process at least partly regulated by IL-2 (Boyman and Sprent 2012). In our study, similar to most CAR T cell trials, we pre-activated all CAR T cells *in vitro* with IL-2 before injection. This pre-activation explains the fast migration of allogeneic h1928z CAR T cells, syngeneic h1928z CAR T cells, and mock CAR T cells towards the inflammatory milieu of established intracranial tumors.

In our study, infiltration into the tumor core in high numbers is restricted to functional h1928z CAR T cells, as mock CAR T cells accumulated at the tumor borders and in the subarachnoid space bordering the intracranial PCNSL, underlining the effect of second-generation h1928z CARs on tumor infiltration.

In large, established tumors, immunosuppressive myeloid cells and tumor fibroblasts can contribute to deposition of a fibrotic extracellular matrix, hindering T cell function (Tumeh et al. 2014). Intravital microscopy has recently identified another immunosupressive barrier for successful tumor infiltration, as regulatory T cells (Tregs) were able to form an “immunosuppressive ring” around solid tumor xenografts (Qi et al. 2016). Although we did not analyze the individual contribution of specific immune cell subsets for CAR T cell treatment by TPLSM, other groups have shown that even six-color TPLSM is possible, theoretically enabling discrimination of multiple intratumoral cell types simultaneously (Ricard and Debarbieux 2014). It would be interesting to see future studies unravelling the individual cellular components of the tumor microenvironment, and correlating these with successful tumor regression or therapeutic resistance during CAR T cell therapy.

5.3 Intratumoral T cell velocity

TPLSM has already been used to delineate interactions of immune cells with cancer cells during tumor regression. For example, Boissonnas and colleagues have shown that tumor-antigen specific, $CD8^+$ cytotoxic T lymphocytes (CTLs) are able to infiltrate subcutaneous thymoma in high numbers, leading to elimination of this antigen expressing, solid tumor (Boissonnas et al. 2007). Interestingly, they show that during the early stages of tumor cell killing, infiltrating CTLs have a lower intratumoral velocity. Conversely, in tumors not expressing the cognate antigen, antigen-specific CTLs show higher migratory velocity and neither stop moving nor kill tumor cells, suggesting that lower intratumoral velocity is associated with TCR-mediated tumor cell killing. These findings have later been corroborated by Breart et al. (Breart et al. 2008), who confirmed that tumor apoptosis is primarily initiated through direct, stable contacts between CTLs and tumor cells with minimal bystander effect. But intratumoral velocity during anti-tumor responses is not universally lower across all leukocytes. Deguine and colleagues showed that NK cells are similarly able to accumulate in tumors expressing an NK cell activating ligand (Deguine et al. 2010). However, a striking contrast exists regarding contact stability and intratumoral NK cell velocity compared to intratumoral T cells. Intratumoral NK cells had also higher intratumoral velocity compared to intratumoral NK cells in tumors devoid of this NK-activating ligand, meaning that NK cells become faster during the initial stages of successful tumor eradication, forming dynamic contacts to tumor cells rather than stable contacts as seen in TCR-mediated tumor cell killing.

As illustrating as these experiments have been for analysis of intratumoral cell movements, all of them were limited in one important dimension: in time. In each individual mouse, analysis was restricted to a single time point, as the setup of these experiments was not suitable to keep the mouse alive after imaging.

In our chronic cranial window model, we were able to analyze changes of intratumoral CAR T cell velocity in the same mouse over the course of more than 4 weeks. Indeed, the velocity of intratumoral CAR T cells changed significantly over time. During the first week after injection, CAR T cells showed decreased intratumoral velocities, consistent with the hypothesized function of a CAR: after contact with the tumor surface antigen and the resulting downstream signaling, CAR T cells should become activated and should therefore stop migration to proliferate and exert cytotoxic effects (by releasing cytotoxic molecules, such as perforin and granzyme B (Darcy et al. 2000)), similar to TCR based activation. However, we have shown that in the later periods of tumor growth, h1928z CAR T cells resume higher intratumoral velocities, reaching a similar velocity as contralateral h1928z CAR T cells not in contact with tumor cells. CAR T cells are able to sequentially contact and kill several tumor cells, with more rapid detachment of tumor cells compared to TCR-mediated cytotoxicity (Davenport et al. 2015). Therefore, the increased intratumoral h1928z CAR T cell velocity seen at later time points could be a CAR specific effect, suggesting that CAR T cells form rather short-lived synapses with their target antigen, similar to NK cells (Deguine et al. 2010).

Conversely, another potential reason for higher intratumoral velocities could be loss or mutation of the CAR specific antigen during CAR T cell therapy. CD19-negative relapses after successful anti-CD19 CAR T cell therapy have been described in 10-30% of B-ALL patients, resulting from immune editing leading to downregulation, alternative splicing, or mutation of tumor surface CD19 (Ruella and Maus 2016; Ruella et al. 2016; Sotillo et al. 2015).

Therefore, no conclusion can be drawn if this increase in intratumoral velocity over the first weeks after CAR T cell injection is correlated to enhanced cytotoxic activity, or rather indicative of changes in antigen expression and possible treatment failure. Comparison of different CARs, such as different scFvs or different costimulatory domains (such as 1928z with 1941BBz CARs) could help to validate the role of intratumoral velocity, a property depending on multiple factors, including tumor antigen expression, CAR expression, scFv affinity, downstream signaling, costimulatory signaling as well as tumor-derived immunosuppressive factors.

Mock CAR T cells did not enter the tumor in high numbers, but the few cells that were able to infiltrate the tumor moved faster than h1928z CAR T cells at initial time points, and remained near-stationary at later time points. As these T cells completely depend on their TCR-mediated signaling, this reduced velocity could be due to limited anti-tumor efficacy at early time points after mock CAR T cell injection. The low number of intratumoral T cells and also the slow velocity of mock CAR T cells at later time points could be the result of the immunosuppressive PCNSL microenvironment. Induced by xenoimmunity, also an anergic phenotype could be assumed by these T cells, leading to T cell exhaustion due to tonic TCR signaling (Schmid et al. 2010).

5.4 Persistence

Intratumoral as well as extratumoral persistence has been correlated with favorable outcome after CAR T cell therapy (Porter et al. 2015). Here, we corroborate these results and furthermore show that intracranial as well as intravascular persistence of h1928z CAR T cells is possible for more than 159 days following intracranial injection.

Mock CAR T cells reached their highest intratumoral and intracerebral number at day 8 after injection, and T cell number decreased thereafter. Also allogeneic CAR T cells did not persist for three weeks *in situ*. Therefore, it seems conclusive that therapeutic efficacy is directly correlated to CAR T cell persistence.

Furthermore, we demonstrated that h1928z CAR T cells and mock CAR T cells are able to intravasate into the blood stream, however, h1928z CAR T cells entered the blood circulation at earlier time point than mock CAR T cellss. How T cells leave the brain to enter the vascular circulation is still up to debate. Recently, dural lymphatic vessels have been identified, able to drain interstitial fluid and macromolecules (Aspelund et al. 2015; Louveau et al. 2015). Interestingly, Louveau and colleagues have shown that T cells are able to invade into these Lyve-1+ vessels and that these vessels drain into the deep and superficial cervical lymph nodes, where we also found CAR T cells at high numbers. Although we haven't visualized CAR T cell movement along these lymphatic vessels directly, future studies should evaluate the effect of the CNS lymphatic system on the long term persistence and systemic circulation of these cells.

Another important finding is that after intracerebral h1928z CAR T cell injection, these cells are able to invade even non-draining lymph nodes in high numbers, a feature that has not been described for CAR T cells yet (Doyle 2015). In adaptive immunity, lymph

nodes are the primary organ where naïve T cells survey dendritic cells (DCs) for their cognate antigen (Bousso 2008). Here, T cell-DC interaction involves several receptor-ligand interactions necessary for sustained T cell response. If these immunologically indispensable lymph nodes are similarly active modulators shaping the systemic CAR T cell response is currently unknown. Therefore, the question whether infiltration of secondary lymphoid organs is a necessary step for successful tumor eradication, or just a byproduct of mere intravascular presence of CAR T cells, remains to be determined in future studies.

5.5 Limitations

One limitation of this Foxn1$^{nu/nu}$ model is the possible contribution of xenoimmunity to adoptive cell therapy. This process, also termed the graft-versus-lymphoma effect in humans, describes a process during which allogeneic T cells are able to exert cytotoxic effects on tumor cells after allogeneic marrow transplantation (Jones et al. 1991) or donor lymphocyte infusions (Mandigers et al. 2003). In mice, this effect has already been reported more than 40 years ago (Bortin, Rimm, and Saltzstein 1973). In this famous experiment, irradiated mice were inoculated with lymphoma cells and treated with immunocompetent cells from allogeneic (MHC mismatched) donors, which were able to kill leukemia cells.

To control for this effect, we compared double transduced h1928z CAR T cells (eGFP and an anti-CD19 CAR) with double transduced mock CAR T cells (eGFP and a dysfunctional CAR lacking the extracellular scFv domain). Although we showed that *in vitro*, mock CAR T cells did not exert a cytotoxic effect on human lymphoma cells (Figure 12), this possibility can still play a significant role *in vivo*. Indeed, also mock CAR T cells showed some effect on tumor growth (Figure 24). However, the rate of complete remissions in mice with cranial windows treated with mock transduced CAR T cells (1/5) was rather low compared to the number of complete remissions in the h1928z CAR T cell group (4/6).

By transplanting mature T cells, the defect in T cell mediated immunity of nude mice can be corrected (Wortis, Nehlsen, and Owen 1971), and IL-2 injection can induce cytotoxicity of T cell precursors in athymic mice (Hunig and Bevan 1980). Therefore, both injection of mock transduced T cells and injection of small amounts of IL-2 possibly still present in the cell injection medium could explain the rare tumor regressions in mice treated with mock CAR T cells.

5.6 Clinical relevance

Clinical evidence for the efficacy of intracranial CAR T cell delivery comes from a recently published case report about a patient with recurrent multifocal glioblastoma (Brown et al. 2016), a disease among the most lethal of human cancers. Brown and colleagues have not only shown that repeated, intracranial (i.e. intratumoral and intraventricular) injection of interleukin-13 receptor alpha 2 (IL13Rα2)-specific CAR T cells is feasible, with no apparent high grade toxicity. Most importantly, this route of application led to regression of all intracranial tumor manifestations, including intraspinal lesions, for more than seven months, a result inconceivable with current treatment options. Although intratumoral presence of CAR T cells has also been described in glioblastoma after i.v. administration, so far this intracerebral presence has only been accomplished after administration of extremely high numbers of cells (1-5x10^8), possibly increasing the risk of severe side effects like the cytokine release syndrome (CRS) (O'Rourke et al. 2016). CRS is one of the most severe side effects of this highly potent immunotherapy (Lee et al. 2014; Brudno and Kochenderfer 2016). As CAR T cells are infused into the patient, they infiltrate the tumor in high numbers, where they become activated. Upon activation, these T cells proliferate and, while killing tumor cells, release inflammatory cytokines. In the serum of patients with CRS, higher levels of IL-6, interferon-gamma, tumor necrosis factor, IL-2, IL-2-receptor-alpha, IL-8, and IL-10 have been identified (Brudno and Kochenderfer 2016). The resulting CRS is characterized by fever, pulmonary edema and shock. Importantly, also neurologic toxicity has been described as a potential consequence of anti-CD19 CAR T cell therapy, ranging from mild delirium to seizures, aphasia, tremors, ataxia, or cerebral edema. Several groups have detected CAR T cells in the cerebrospinal fluid after intravenous application (Grupp et al. 2013; Davila et al. 2014; Maude et al. 2014; Lee et al. 2015). Importantly, in patients with neurologic symptoms, the number of intracranial anti-CD19 CAR T cells was elevated compared to patients without neurologic symptoms (Lee et al. 2015). However, the presence of leukemic cells in the CNS has not been identified as a risk factor for the development of neurological symptoms (Maude et al. 2014; Lee et al. 2015). The exact pathophysiology for CAR T cell associated neurotoxicity is still debated, and hypothesized to be related to intracerebral IL-6-levels (Lee et al. 2014).

In our mouse model, we have not seen cytokine release syndrome after intracranial application of h1928z CAR T cells. At a first glance, this finding might seem indicative of the relative safety of this approach. However, mouse models recapitulating CRS have only been seen in mice also expressing the tumor antigen on healthy cells (van der Stegen et al. 2013). Hence, the absence of CRS during anti-human CD19 CAR T cell

therapy has to be rated with caution, as most cancer xenograft models did not anticipate the incidence of this potentially severe side effect in patients.

Another relevant topic for treatment of PCNSL is the route of delivery. T cell entry into the CNS is a tightly regulated process (Engelhardt and Ransohoff 2012). Although low numbers of T cells are known to patrol the CSF and meninges in the healthy CNS, in the absence of inflammation these cells are retained in these CSF drained spaces (e.g. the subarachnoid space), separated from the CNS parenchyma by the glia limitans. In the subarachnoid space, T cells interact with antigen presenting cells (APCs) in search for their cognate antigen. If T cells fail to recognize their antigen presented by APCs, these T cells do not enter the parenchyma, as has been shown in animal models of experimental autoimmune encephalomyelitis (Bartholomaus et al. 2009; Schlager et al. 2016). As CAR T cells exert their function independently of MHC presentation, the proportion of CAR T cells migrating deep into the core of CNS malignancies after i.v. application is expected to be rather low. Furthermore, Adusumilli and colleagues have shown that the regional delivery of tumor-specific CAR T cells to the tumor (in this case, mesothelioma) generates more potent and durable tumor responses compared to i.v. injection, underlining the importance of early CAR T cell tumor infiltration for successful therapy (Adusumilli et al. 2014).

Taken together, these experiments led us to believe that in a mouse model of PCNSL, intracranial injection of CAR T cells would lead to improved tumor infiltration compared to i.v. application. As expected, this approach was successful to delineate tumor specific anti-CD19 CAR T cell behavior inside the brain and PCNSL, allowing us to characterize its therapeutic effects. Another advantage of this route of CAR T cell administration is the lower number needed for successful treatment, thereby possibly limiting the risk for CRS development (O'Rourke et al. 2016; Lee et al. 2014).

In animal models, often high numbers (5-20x10^6) of CAR T cells are injected i.v. to successfully inhibit tumor growth (Brentjens et al. 2003; Kowolik et al. 2006; Brentjens et al. 2007; Tsukahara et al. 2013). At such high numbers of injected CAR T cells, differences between distinct CAR constructs become undistinguishable, as most CAR constructs lead to tumor eradication. Zhao and colleagues have consequently lowered i.v. treatment dose to 1x10^5 cells, thereby reducing efficacy of tumor eradication. This way, comparison of several highly potent CAR constructs became possible (Zhao et al. 2015). Interestingly, in our xenograft model of PCNSL with tumor growth of 14 days before application of h1928z CAR T cells, we see a potent, durable effect after intracranial injection of only 5x10^4 cells. Even more surprising was the fact that also intracranial

injection of $2x10^4$ 1928z CAR T cells led to a sustained anti-tumor response, with intravascular h1928z CAR T cells present in high numbers.

One reason for this high potency could be due to the high efficacy of the 1928z CAR construct. Zhao et al. have shown that 1928z CAR T cells exhibit more potent anti-tumor cytotoxicity, resulting in more rapid tumor cell killing. The 19BBz CAR on the other hand, where the CD28 costimulatory domain is exchanged with the 4-1BB costimulatory domain, show slower tumor elimination, but increased persistence compared to 1928z CARs (Zhao et al. 2015). The reasons for this are still debated, but experiments comparing these two CAR constructs using intravital microscopy could shed light onto this otherwise difficult-to-assess immune response.

Another reason for this high potency could be the regional delivery of CAR T cells compared to the often used intravenous route of application. Adusumilli and colleagues have first shown that intrapleural delivery of mesothelioma-specific CAR T cells vastly outperforms intravenous delivery, requiring 30-fold higher cellular doses for intravenous application to achieve similar therapeutic activity (Adusumilli et al. 2014). This way, even intrapleurally injected CAR T cell dosages of $3x10^4$ cells could control mesothelioma growth.

Based on our results as well as on clinical trials evaluating the safety of intracranially injected CAR T cells (Jackson, Rafiq, and Brentjens 2016), we propose that in future clinical trials evaluating this highly successful second generation anti-CD19 CAR, intracranial, intraventricular, or even intratumoral route of delivery should be preferred.

6 Conclusion

Surprisingly, despite the proven efficacy of CAR T cell therapy in numerous malignancies, many questions regarding the exact dynamics of this highly potent immunotherapy remain unanswered. So far, no study has been able to analyze intratumoral or intracerebral CAR T cell behavior in the brain in detail, including tumor infiltration, tumor cell killing, persistence and proliferation at single-cell resolution.

Here, we have created a novel animal model of PCNSL recapitulating many characteristics of human PCNSL growth. Combining this model with a chronic cranial window, we were able to repeatedly visualize intracranial PCNSL growth over several weeks. Furthermore, we demonstrated that intracranial injection of low numbers of h1928z CAR T cells can lead to complete regression of large, established intracranial tumors. By using *in vivo* and *ex vivo* fluorescence microscopy, we showed that h1928z CAR T cells invaded the solid tumor in high numbers, whereas mock CAR T cells only accumulated at the tumor margin, leading to reduced intratumoral T cell numbers. During the first week after CAR T cell injection, intratumoral h1928z CAR T cells migrated at a lower velocity than mock CAR T cells and stopped tumor progression, suggesting anti-tumor cytotoxicity. In the contralateral brain hemisphere, CAR T cells of both groups moved at a similar velocity. At later time points, h1928z CAR T cells further increased in number, with *in situ* proliferation being visible, whereas intratumoral and contralateral mock CAR T cell numbers decreased continuously. Complete regression of large, established PCNSL was seen in 4 of 6 mice (66.7%). Even after complete regression of tumor cells, h1928z CAR T cells persisted *in situ* for more than 150 days in high numbers. Already 5 days after intracranial injection, h1928z CAR T cells intravasated into the blood circulation and even infiltrated distant, non-draining lymph nodes in high numbers.

These results illustrate the high potential of second generation anti-CD19 CAR T cell therapy in PCNSL. Currently, several trials are recruiting glioblastoma patients to evaluate the efficacy of intracranial CAR T cell application. As toxic side effects of CAR T cell therapy are dose-related and anti-CD19 CAR T cells are the most successfully studied CAR to date, clinical trials evaluating the response to intracranial injection of low numbers of anti-CD19 CAR T cells are highly warranted.

7 Abbreviations

ACT	-	Ammonium chloride-Tris
ADC	-	Apparent diffusion coefficient
AF	-	Alexa Fluor
ALL	-	Acute lymphoblastic leukemia
BBB	-	Blood brain barrier
CAR	-	Chimeric Antigen Receptor
CCD	-	Charge-coupled device
CLL	-	Chronic lymphocytic leukemia
CNS	-	Central nervous system
CRS	-	Cytokine release syndrome
CSF	-	Cerebrospinal fluid
CTL	-	Cytotoxic T lymphocytes
DAPI	-	4’,6-Diamidino-2-phenylindole
DC	-	Dendritic cells
DLBCL	-	Diffuse large B cell lymphoma
DNA	-	Deoxyribonucleic acid
DPBS	-	Dulbecco’s phosphate-buffered saline
DsRed2	-	A red fluorescent protein, derived from *Discosoma sp*.
DWI	-	Diffusion-weighted images
FACS	-	Fluorescence-activated cell sorting
FBS	-	Fetal bovine serum

FELASA	-	Federation of European Laboratory Animal Associations
G418	-	Geneticin
GEM	-	Genetically engineered model
eGFP	-	Enhanced green fluorescent protein
HSCT	-	Hematopoietic stem cell transplantation
i.p.	-	Intraperitoneal
IRES	-	Internal ribosome entry site
i.v.	-	Intravenous
LB	-	Lysogeny broth
LDH	-	Lactate dehydrogenase
MHC	-	Major histocompatibility complex
MMF	-	Medetomidine / midazolam / fentanyl
MRI	-	Magnetic resonance imaging
mRNA	-	Messenger ribonucleic acid
NaCl	-	Sodium chloride solution
NDD	-	Non descanned detector
NHL	-	Non-Hodgkin lymphoma
NOD	-	Non-obese diabetic
OD600	-	Optical density at a wavelength of 600 nm
PCNSL	-	Primary CNS lymphoma
PFA	-	Paraformaldehyde
PlatE	-	Platinum E, a retroviral packaging cell line
PMT	-	Photo multiplier tube
RFP	-	Red fluorescent protein
ROI	-	Region of interest

ROS	-	Reactive oxygen species
rpm	-	Rounds per minute
s.c.	-	Subcutaneous
scFv	-	Single chain variable fragment
SCID	-	Severe combined immunodeficiency
s.e.m.	-	Standard error of the mean
SHG	-	Second harmonic generation
tdTomato	-	Tandem dimer tomato, a red fluorescent protein derived from a monomeric mutant of *DsRed*
TCR	-	T cell receptor
TILs	-	Tumor infiltrating lymphocytes
TPLSM	-	Two-photon laser scanning microscopy
Treg	-	Regulatory T cells

8 List of figures

9 Bibliography

Adusumilli, P. S., L. Cherkassky, J. Villena-Vargas, C. Colovos, E. Servais, J. Plotkin, D. R. Jones, and M. Sadelain. 2014. 'Regional delivery of mesothelin-targeted CAR T cell therapy generates potent and long-lasting CD4-dependent tumor immunity', *Sci Transl Med*, 6: 261ra151.

Aguirre-Ghiso, J. A. 2007. 'Models, mechanisms and clinical evidence for cancer dormancy', *Nat Rev Cancer*, 7: 834-46.

Alieva, M., L. Ritsma, R. J. Giedt, R. Weissleder, and J. van Rheenen. 2014. 'Imaging windows for long-term intravital imaging: General overview and technical insights', *Intravital*, 3: e29917.

Alpdogan, S. O., S. X. Lu, N. Patel, S. McGoldrick, D. Suh, T. Budak-Alpdogan, O. M. Smith, J. Grubin, C. King, G. L. Goldberg, V. M. Hubbard, A. A. Kochman, and M. R. van den Brink. 2008. 'Rapidly proliferating CD44hi peripheral T cells undergo apoptosis and delay posttransplantation T-cell reconstitution after allogeneic bone marrow transplantation', *Blood*, 112: 4755-64.

Aspelund, A., S. Antila, S. T. Proulx, T. V. Karlsen, S. Karaman, M. Detmar, H. Wiig, and K. Alitalo. 2015. 'A dural lymphatic vascular system that drains brain interstitial fluid and macromolecules', *J Exp Med*, 212: 991-9.

Bai, Y., S. Kan, S. Zhou, Y. Wang, J. Xu, J. P. Cooke, J. Wen, and H. Deng. 2015. 'Enhancement of the in vivo persistence and antitumor efficacy of CD19 chimeric antigen receptor T cells through the delivery of modified TERT mRNA', *Cell Discov*, 1: 15040.

Bakker, R., P. Tiesinga, and R. Kotter. 2015. 'The Scalable Brain Atlas: Instant Web-Based Access to Public Brain Atlases and Related Content', *Neuroinformatics*, 13: 353-66.

Bartholomaus, I., N. Kawakami, F. Odoardi, C. Schlager, D. Miljkovic, J. W. Ellwart, W. E. Klinkert, C. Flugel-Koch, T. B. Issekutz, H. Wekerle, and A. Flugel. 2009. 'Effector T cell interactions with meningeal vascular structures in nascent autoimmune CNS lesions', *Nature*, 462: 94-8.

Bataille, B., V. Delwail, E. Menet, P. Vandermarcq, P. Ingrand, M. Wager, G. Guy, and F. Lapierre. 2000. 'Primary intracerebral malignant lymphoma: report of 248 cases', *J Neurosurg*, 92: 261-6.

Batchelor, T., and J. S. Loeffler. 2006. 'Primary CNS lymphoma', *J Clin Oncol*, 24: 1281-8.

Batchelor, T. T., S. A. Grossman, T. Mikkelsen, X. Ye, S. Desideri, and G. J. Lesser. 2011. 'Rituximab monotherapy for patients with recurrent primary CNS lymphoma', *Neurology*, 76: 929-30.

Bellinzona, M., F. Roser, H. Ostertag, R. M. Gaab, and M. Saini. 2005. 'Surgical removal of primary central nervous system lymphomas (PCNSL) presenting as space occupying lesions: a series of 33 cases', *Eur J Surg Oncol*, 31: 100-5.

Birnbaum, T., E. A. Stadler, L. von Baumgarten, and A. Straube. 2012. 'Rituximab significantly improves complete response rate in patients with primary CNS lymphoma', *J Neurooncol*, 109: 285-91.

Boissonnas, A., L. Fetler, I. S. Zeelenberg, S. Hugues, and S. Amigorena. 2007. 'In vivo imaging of cytotoxic T cell infiltration and elimination of a solid tumor', *J Exp Med*, 204: 345-56.

Bortin, M. M., A. A. Rimm, and E. C. Saltzstein. 1973. 'Graft versus leukemia: quantification of adoptive immunotherapy in murine leukemia', *Science*, 179: 811-3.

Bousso, P. 2008. 'T-cell activation by dendritic cells in the lymph node: lessons from the movies', *Nat Rev Immunol*, 8: 675-84.

Boyman, O., and J. Sprent. 2012. 'The role of interleukin-2 during homeostasis and activation of the immune system', *Nat Rev Immunol*, 12: 180-90.

Braaten, K. M., R. A. Betensky, L. de Leval, Y. Okada, F. H. Hochberg, D. N. Louis, N. L. Harris, and T. T. Batchelor. 2003. 'BCL-6 expression predicts improved survival in patients with primary central nervous system lymphoma', *Clin Cancer Res*, 9: 1063-9.

Breart, B., F. Lemaitre, S. Celli, and P. Bousso. 2008. 'Two-photon imaging of intratumoral CD8+ T cell cytotoxic activity during adoptive T cell therapy in mice', *J Clin Invest*, 118: 1390-7.

Brentjens, R. J., M. L. Davila, I. Riviere, J. Park, X. Wang, L. G. Cowell, S. Bartido, J. Stefanski, C. Taylor, M. Olszewska, O. Borquez-Ojeda, J. Qu, T. Wasielewska, Q. He, Y. Bernal, I. V. Rijo, C. Hedvat, R. Kobos, K. Curran, P. Steinherz, J. Jurcic, T. Rosenblat, P. Maslak, M. Frattini, and M. Sadelain. 2013. 'CD19-targeted T cells rapidly induce molecular remissions in adults with chemotherapy-refractory acute lymphoblastic leukemia', *Sci Transl Med*, 5: 177ra38.

Brentjens, R. J., J. B. Latouche, E. Santos, F. Marti, M. C. Gong, C. Lyddane, P. D. King, S. Larson, M. Weiss, I. Riviere, and M. Sadelain. 2003. 'Eradication of systemic B-cell tumors by genetically targeted human T lymphocytes co-stimulated by CD80 and interleukin-15', *Nat Med*, 9: 279-86.

Brentjens, R. J., E. Santos, Y. Nikhamin, R. Yeh, M. Matsushita, K. La Perle, A. Quintas-Cardama, S. M. Larson, and M. Sadelain. 2007. 'Genetically targeted T cells eradicate systemic acute lymphoblastic leukemia xenografts', *Clin Cancer Res*, 13: 5426-35.

Brocker, T., and K. Karjalainen. 1995. 'Signals through T cell receptor-zeta chain alone are insufficient to prime resting T lymphocytes', *J Exp Med*, 181: 1653-9.

Brown, C. E., D. Alizadeh, R. Starr, L. Weng, J. R. Wagner, A. Naranjo, J. R. Ostberg, M. S. Blanchard, J. Kilpatrick, J. Simpson, A. Kurien, S. J. Priceman, X. Wang, T. L. Harshbarger, M. D'Apuzzo, J. A. Ressler, M. C. Jensen, M. E. Barish, M. Chen, J. Portnow, S. J. Forman, and B. Badie. 2016. 'Regression of Glioblastoma after Chimeric Antigen Receptor T-Cell Therapy', *N Engl J Med*, 375: 2561-9.

Brudno, J. N., and J. N. Kochenderfer. 2016. 'Toxicities of chimeric antigen receptor T cells: recognition and management', *Blood*, 127: 3321-30.

Brudno, J. N., R. P. Somerville, V. Shi, J. J. Rose, D. C. Halverson, D. H. Fowler, J. C. Gea-Banacloche, S. Z. Pavletic, D. D. Hickstein, T. L. Lu, S. A. Feldman, A. T. Iwamoto, R. Kurlander, I. Maric, A. Goy, B. G. Hansen, J. S. Wilder, B. Blacklock-Schuver, F. T. Hakim, S. A. Rosenberg, R. E. Gress, and J. N. Kochenderfer. 2016. 'Allogeneic T Cells That Express an Anti-CD19 Chimeric Antigen Receptor Induce Remissions of B-Cell Malignancies That Progress After Allogeneic Hematopoietic Stem-Cell Transplantation Without Causing Graft-Versus-Host Disease', *J Clin Oncol*, 34: 1112-21.

Buhring, U., U. Herrlinger, T. Krings, R. Thiex, M. Weller, and W. Kuker. 2001. 'MRI features of primary central nervous system lymphomas at presentation', *Neurology*, 57: 393-6.

Coley, W. B. 1898. 'The treatment of inoperable sarcoma with the 'mixed toxins of erysipelas and bacillus prodigiosus.: Immediate and final results in one hundred and forty cases', *Journal of the American Medical Association*, XXXI: 456-65.

Cordone, I., S. Masi, M. Carosi, A. Vidiri, F. Marchesi, M. Marino, S. Telera, A. Pasquale, A. Mengarelli, L. Conti, E. Pescarmona, A. Pace, and C. M. Carapella. 2016. 'Brain stereotactic biopsy flow cytometry for central nervous system lymphoma characterization: advantages and pitfalls', *J Exp Clin Cancer Res*, 35: 128.

Couzin-Frankel, J. 2013. 'Breakthrough of the year 2013. Cancer immunotherapy', *Science*, 342: 1432-3.

Darcy, P. K., N. M. Haynes, M. B. Snook, J. A. Trapani, L. Cerruti, S. M. Jane, and M. J. Smyth. 2000. 'Redirected perforin-dependent lysis of colon carcinoma by ex vivo genetically engineered CTL', *J Immunol*, 164: 3705-12.

Davenport, A. J., M. R. Jenkins, R. S. Cross, C. S. Yong, H. M. Prince, D. S. Ritchie, J. A. Trapani, M. H. Kershaw, P. K. Darcy, and P. J. Neeson. 2015. 'CAR-T Cells Inflict Sequential Killing of Multiple Tumor Target Cells', *Cancer Immunol Res*, 3: 483-94.

Davila, M. L., I. Riviere, X. Wang, S. Bartido, J. Park, K. Curran, S. S. Chung, J. Stefanski, O. Borquez-Ojeda, M. Olszewska, J. Qu, T. Wasielewska, Q. He, M. Fink, H.

Shinglot, M. Youssif, M. Satter, Y. Wang, J. Hosey, H. Quintanilla, E. Halton, Y. Bernal, D. C. Bouhassira, M. E. Arcila, M. Gonen, G. J. Roboz, P. Maslak, D. Douer, M. G. Frattini, S. Giralt, M. Sadelain, and R. Brentjens. 2014. 'Efficacy and toxicity management of 19-28z CAR T cell therapy in B cell acute lymphoblastic leukemia', *Sci Transl Med*, 6: 224ra25.

DeAngelis, L. M., W. Seiferheld, S. C. Schold, B. Fisher, C. J. Schultz, and Study Radiation Therapy Oncology Group. 2002. 'Combination chemotherapy and radiotherapy for primary central nervous system lymphoma: Radiation Therapy Oncology Group Study 93-10', *J Clin Oncol*, 20: 4643-8.

DeAngelis, L. M., J. Yahalom, M. H. Heinemann, C. Cirrincione, H. T. Thaler, and G. Krol. 1990. 'Primary CNS lymphoma: combined treatment with chemotherapy and radiotherapy', *Neurology*, 40: 80-6.

Deguine, J., B. Breart, F. Lemaitre, J. P. Di Santo, and P. Bousso. 2010. 'Intravital imaging reveals distinct dynamics for natural killer and CD8(+) T cells during tumor regression', *Immunity*, 33: 632-44.

Denk, W., J. H. Strickler, and W. W. Webb. 1990. 'Two-photon laser scanning fluorescence microscopy', *Science*, 248: 73-6.

Desjardins, P., and D. Conklin. 2010. 'NanoDrop microvolume quantitation of nucleic acids', *J Vis Exp*.

Dixit, R., and R. Cyr. 2003. 'Cell damage and reactive oxygen species production induced by fluorescence microscopy: effect on mitosis and guidelines for non-invasive fluorescence microscopy', *Plant J*, 36: 280-90.

Doyle, C. 2015. 'CAR-T Cells: The Transplants of the Future', *Am Health Drug Benefits*, 8: 14.

Drobizhev, M., N. S. Makarov, S. E. Tillo, T. E. Hughes, and A. Rebane. 2011. 'Two-photon absorption properties of fluorescent proteins', *Nat Methods*, 8: 393-9.

Dudley, M. E., C. A. Gross, R. P. Somerville, Y. Hong, N. P. Schaub, S. F. Rosati, D. E. White, D. Nathan, N. P. Restifo, S. M. Steinberg, J. R. Wunderlich, U. S. Kammula, R. M. Sherry, J. C. Yang, G. Q. Phan, M. S. Hughes, C. M. Laurencot, and S. A. Rosenberg. 2013. 'Randomized selection design trial evaluating CD8+-enriched versus unselected tumor-infiltrating lymphocytes for adoptive cell therapy for patients with melanoma', *J Clin Oncol*, 31: 2152-9.

Ellenbroek, S. I., and J. van Rheenen. 2014. 'Imaging hallmarks of cancer in living mice', *Nat Rev Cancer*, 14: 406-18.

Engelhardt, B., and R. M. Ransohoff. 2012. 'Capture, crawl, cross: the T cell code to breach the blood-brain barriers', *Trends Immunol*, 33: 579-89.

Engelhardt, B., P. Vajkoczy, and R. O. Weller. 2017. 'The movers and shapers in immune privilege of the CNS', *Nat Immunol*, 18: 123-31.

Engels, B., H. Cam, T. Schuler, S. Indraccolo, M. Gladow, C. Baum, T. Blankenstein, and W. Uckert. 2003. 'Retroviral vectors for high-level transgene expression in T lymphocytes', *Hum Gene Ther*, 14: 1155-68.

Eshhar, Z., T. Waks, G. Gross, and D. G. Schindler. 1993. 'Specific activation and targeting of cytotoxic lymphocytes through chimeric single chains consisting of antibody-binding domains and the gamma or zeta subunits of the immunoglobulin and T-cell receptors', *Proc Natl Acad Sci U S A*, 90: 720-4.

Ferreri, A. J., K. Cwynarski, E. Pulczynski, M. Ponzoni, M. Deckert, L. S. Politi, V. Torri, C. P. Fox, P. L. Rosee, E. Schorb, A. Ambrosetti, A. Roth, C. Hemmaway, A. Ferrari, K. M. Linton, R. Ruda, M. Binder, T. Pukrop, M. Balzarotti, A. Fabbri, P. Johnson, J. S. Gorlov, G. Hess, J. Panse, F. Pisani, A. Tucci, S. Stilgenbauer, B. Hertenstein, U. Keller, S. W. Krause, A. Levis, H. J. Schmoll, F. Cavalli, J. Finke, M. Reni, E. Zucca, G. Illerhaus, and Group International Extranodal Lymphoma Study. 2016. 'Chemoimmunotherapy with methotrexate, cytarabine, thiotepa, and rituximab (MATRix regimen) in patients with primary CNS lymphoma: results of the first randomisation of the International Extranodal Lymphoma Study Group-32 (IELSG32) phase 2 trial', *Lancet Haematol*, 3: e217-27.

Ferreri, A. J., M. Reni, M. Foppoli, M. Martelli, G. A. Pangalis, M. Frezzato, M. G. Cabras, A. Fabbri, G. Corazzelli, F. Ilariucci, G. Rossi, R. Soffietti, C. Stelitano, D. Vallisa, F. Zaja, L. Zoppegno, G. M. Aondio, G. Avvisati, M. Balzarotti, A. A. Brandes, J. Fajardo, H. Gomez, A. Guarini, G. Pinotti, L. Rigacci, C. Uhlmann, P. Picozzi, P. Vezzulli, M. Ponzoni, E. Zucca, F. Caligaris-Cappio, F. Cavalli, and Group International Extranodal Lymphoma Study. 2009. 'High-dose cytarabine plus high-dose methotrexate versus high-dose methotrexate alone in patients with primary CNS lymphoma: a randomised phase 2 trial', *Lancet*, 374: 1512-20.

Ferreri, A. J., M. Reni, F. Pasini, A. Calderoni, U. Tirelli, A. Pivnik, G. M. Aondio, F. Ferrarese, H. Gomez, M. Ponzoni, B. Borisch, F. Berger, C. Chassagne, P. Iuzzolino, A. Carbone, J. Weis, E. Pedrinis, T. Motta, A. Jouvet, T. Barbui, F. Cavalli, and J. Y. Blay. 2002. 'A multicenter study of treatment of primary CNS lymphoma', *Neurology*, 58: 1513-20.

Fesnak, A. D., C. H. June, and B. L. Levine. 2016. 'Engineered T cells: the promise and challenges of cancer immunotherapy', *Nat Rev Cancer*, 16: 566-81.

Festing, M. F., and D. G. Altman. 2002. 'Guidelines for the design and statistical analysis of experiments using laboratory animals', *ILAR J*, 43: 244-58.

Fischer, L., A. Korfel, P. Kiewe, M. Neumann, K. Jahnke, and E. Thiel. 2009. 'Systemic high-dose methotrexate plus ifosfamide is highly effective for central nervous system (CNS) involvement of lymphoma', *Ann Hematol*, 88: 133-9.

Fitzsimmons, A., K. Upchurch, and T. Batchelor. 2005. 'Clinical features and diagnosis of primary central nervous system lymphoma', *Hematol Oncol Clin North Am*, 19: 689-703, vii.

Flanagan, S. P. 1966. ''Nude', a new hairless gene with pleiotropic effects in the mouse', *Genet Res*, 8: 295-309.

Fogh, J., J. M. Fogh, and T. Orfeo. 1977. 'One hundred and twenty-seven cultured human tumor cell lines producing tumors in nude mice', *J Natl Cancer Inst*, 59: 221-6.

Frank, J., C. Pignata, A. A. Panteleyev, D. M. Prowse, H. Baden, L. Weiner, L. Gaetaniello, W. Ahmad, N. Pozzi, P. B. Cserhalmi-Friedman, V. M. Aita, H. Uyttendaele, D. Gordon, J. Ott, J. L. Brissette, and A. M. Christiano. 1999. 'Exposing the human nude phenotype', *Nature*, 398: 473-4.

Fraser, E., K. Gruenberg, and J. L. Rubenstein. 2015. 'New approaches in primary central nervous system lymphoma', *Chin Clin Oncol*, 4: 11.

Fritsch, K., B. Kasenda, C. Hader, G. Nikkhah, M. Prinz, V. Haug, S. Haug, G. Ihorst, J. Finke, and G. Illerhaus. 2011. 'Immunochemotherapy with rituximab, methotrexate, procarbazine, and lomustine for primary CNS lymphoma (PCNSL) in the elderly', *Ann Oncol*, 22: 2080-5.

Gavrilovic, I. T., A. Hormigo, J. Yahalom, L. M. DeAngelis, and L. E. Abrey. 2006. 'Long-term follow-up of high-dose methotrexate-based therapy with and without whole brain irradiation for newly diagnosed primary CNS lymphoma', *J Clin Oncol*, 24: 4570-4.

Gong, M. C., J. B. Latouche, A. Krause, W. D. Heston, N. H. Bander, and M. Sadelain. 1999. 'Cancer patient T cells genetically targeted to prostate-specific membrane antigen specifically lyse prostate cancer cells and release cytokines in response to prostate-specific membrane antigen', *Neoplasia*, 1: 123-7.

Grupp, S. A., M. Kalos, D. Barrett, R. Aplenc, D. L. Porter, S. R. Rheingold, D. T. Teachey, A. Chew, B. Hauck, J. F. Wright, M. C. Milone, B. L. Levine, and C. H. June. 2013. 'Chimeric antigen receptor-modified T cells for acute lymphoid leukemia', *N Engl J Med*, 368: 1509-18.

Hackam, D. G., and D. A. Redelmeier. 2006. 'Translation of research evidence from animals to humans', *JAMA*, 296: 1731-2.

Haldorsen, I. S., A. Espeland, and E. M. Larsson. 2011. 'Central nervous system lymphoma: characteristic findings on traditional and advanced imaging', *AJNR Am J Neuroradiol*, 32: 984-92.

He, M., C. Zuo, J. Wang, J. Liu, B. Jiao, J. Zheng, and Z. Cai. 2013. 'Prognostic significance of the aggregative perivascular growth pattern of tumor cells in primary central nervous system diffuse large B-cell lymphoma', *Neuro Oncol*, 15: 727-34.

Helmchen, F., and W. Denk. 2005. 'Deep tissue two-photon microscopy', *Nat Methods*, 2: 932-40.

Herrlinger, U., M. Schabet, M. Bitzer, D. Petersen, and P. Krauseneck. 1999. 'Primary central nervous system lymphoma: from clinical presentation to diagnosis', *J Neurooncol*, 43: 219-26.

Holub, Miroslav. 1992. 'The Nude Mouse', *ILAR Journal*, 34: 1-3.

Honczarenko, M., M. Z. Ratajczak, A. Nicholson-Weller, and L. E. Silberstein. 2005. 'Complement C3a enhances CXCL12 (SDF-1)-mediated chemotaxis of bone marrow hematopoietic cells independently of C3a receptor', *J Immunol*, 175: 3698-706.

Horton, N. G., K. Wang, D. Kobat, C. G. Clark, F. W. Wise, C. B. Schaffer, and C. Xu. 2013. 'In vivo three-photon microscopy of subcortical structures within an intact mouse brain', *Nat Photonics*, 7.

Hunig, T., and M. J. Bevan. 1980. 'Specificity of cytotoxic T cells from athymic mice', *J Exp Med*, 152: 688-702.

Hwu, P., J. C. Yang, R. Cowherd, J. Treisman, G. E. Shafer, Z. Eshhar, and S. A. Rosenberg. 1995. 'In vivo antitumor activity of T cells redirected with chimeric antibody/T-cell receptor genes', *Cancer Res*, 55: 3369-73.

Illerhaus, G., R. Marks, G. Ihorst, R. Guttenberger, C. Ostertag, G. Derigs, N. Frickhofen, F. Feuerhake, B. Volk, and J. Finke. 2006. 'High-dose chemotherapy with autologous stem-cell transplantation and hyperfractionated radiotherapy as first-line treatment of primary CNS lymphoma', *J Clin Oncol*, 24: 3865-70.

Ishikawa, F., M. Yasukawa, B. Lyons, S. Yoshida, T. Miyamoto, G. Yoshimoto, T. Watanabe, K. Akashi, L. D. Shultz, and M. Harada. 2005. 'Development of functional human blood and immune systems in NOD/SCID/IL2 receptor {gamma} chain(null) mice', *Blood*, 106: 1565-73.

Jackson, H. J., S. Rafiq, and R. J. Brentjens. 2016. 'Driving CAR T-cells forward', *Nat Rev Clin Oncol*, 13: 370-83.

Jacoby, E., Y. Yang, H. Qin, C. D. Chien, J. N. Kochenderfer, and T. J. Fry. 2016. 'Murine allogeneic CD19 CAR T cells harbor potent antileukemic activity but have the potential to mediate lethal GVHD', *Blood*, 127: 1361-70.

Jahnke, K., L. L. Muldoon, C. G. Varallyay, S. J. Lewin, R. D. Brown, D. F. Kraemer, C. Soussain, and E. A. Neuwelt. 2009. 'Efficacy and MRI of rituximab and

methotrexate treatment in a nude rat model of CNS lymphoma', *Neuro Oncol*, 11: 503-13.

Jellinger, K., T. H. Radaskiewicz, and F. Slowik. 1975. 'Primary malignant lymphomas of the central nervous system in man', *Acta Neuropathol Suppl*, Suppl 6: 95-102.

Ji, N., J. Freeman, and S. L. Smith. 2016. 'Technologies for imaging neural activity in large volumes', *Nat Neurosci*, 19: 1154-64.

Jones, R. J., R. F. Ambinder, S. Piantadosi, and G. W. Santos. 1991. 'Evidence of a graft-versus-lymphoma effect associated with allogeneic bone marrow transplantation', *Blood*, 77: 649-53.

Kadoch, C., E. B. Dinca, R. Voicu, L. Chen, D. Nguyen, S. Parikh, J. Karrim, M. A. Shuman, C. A. Lowell, P. A. Treseler, C. D. James, and J. L. Rubenstein. 2009. 'Pathologic correlates of primary central nervous system lymphoma defined in an orthotopic xenograft model', *Clin Cancer Res*, 15: 1989-97.

Kadoch, C., J. Li, V. S. Wong, L. Chen, S. Cha, P. Munster, C. A. Lowell, M. A. Shuman, and J. L. Rubenstein. 2014. 'Complement activation and intraventricular rituximab distribution in recurrent central nervous system lymphoma', *Clin Cancer Res*, 20: 1029-41.

Kaelin, W. G., Jr. 2017. 'Common pitfalls in preclinical cancer target validation', *Nat Rev Cancer*, 17: 425-40.

Kasenda, B., E. Schorb, K. Fritsch, J. Finke, and G. Illerhaus. 2012. 'Prognosis after high-dose chemotherapy followed by autologous stem-cell transplantation as first-line treatment in primary CNS lymphoma--a long-term follow-up study', *Ann Oncol*, 23: 2670-5.

Kaufman, W. L., I. Kocman, V. Agrawal, H. P. Rahn, D. Besser, and M. Gossen. 2008. 'Homogeneity and persistence of transgene expression by omitting antibiotic selection in cell line isolation', *Nucleic Acids Res*, 36: e111.

Kienast, Y., L. von Baumgarten, M. Fuhrmann, W. E. Klinkert, R. Goldbrunner, J. Herms, and F. Winkler. 2010. 'Real-time imaging reveals the single steps of brain metastasis formation', *Nat Med*, 16: 116-22.

Kivisakk, P., J. Imitola, S. Rasmussen, W. Elyaman, B. Zhu, R. M. Ransohoff, and S. J. Khoury. 2009. 'Localizing central nervous system immune surveillance: meningeal antigen-presenting cells activate T cells during experimental autoimmune encephalomyelitis', *Ann Neurol*, 65: 457-69.

Kobat, D., M. E. Durst, N. Nishimura, A. W. Wong, C. B. Schaffer, and C. Xu. 2009. 'Deep tissue multiphoton microscopy using longer wavelength excitation', *Opt Express*, 17: 13354-64.

Kochenderfer, J. N., M. E. Dudley, S. A. Feldman, W. H. Wilson, D. E. Spaner, I. Maric, M. Stetler-Stevenson, G. Q. Phan, M. S. Hughes, R. M. Sherry, J. C. Yang, U. S. Kammula, L. Devillier, R. Carpenter, D. A. Nathan, R. A. Morgan, C. Laurencot, and S. A. Rosenberg. 2012. 'B-cell depletion and remissions of malignancy along with cytokine-associated toxicity in a clinical trial of anti-CD19 chimeric-antigen-receptor-transduced T cells', *Blood*, 119: 2709-20.

Kochenderfer, J. N., M. E. Dudley, S. H. Kassim, R. P. Somerville, R. O. Carpenter, M. Stetler-Stevenson, J. C. Yang, G. Q. Phan, M. S. Hughes, R. M. Sherry, M. Raffeld, S. Feldman, L. Lu, Y. F. Li, L. T. Ngo, A. Goy, T. Feldman, D. E. Spaner, M. L. Wang, C. C. Chen, S. M. Kranick, A. Nath, D. A. Nathan, K. E. Morton, M. A. Toomey, and S. A. Rosenberg. 2015. 'Chemotherapy-refractory diffuse large B-cell lymphoma and indolent B-cell malignancies can be effectively treated with autologous T cells expressing an anti-CD19 chimeric antigen receptor', *J Clin Oncol*, 33: 540-9.

Kochenderfer, J. N., Z. Yu, D. Frasheri, N. P. Restifo, and S. A. Rosenberg. 2010. 'Adoptive transfer of syngeneic T cells transduced with a chimeric antigen receptor that recognizes murine CD19 can eradicate lymphoma and normal B cells', *Blood*, 116: 3875-86.

Korfel, A., and U. Schlegel. 2013. 'Diagnosis and treatment of primary CNS lymphoma', *Nat Rev Neurol*, 9: 317-27.

Korfel, A., E. Thiel, P. Martus, R. Mohle, F. Griesinger, M. Rauch, A. Roth, B. Hertenstein, T. Fischer, T. Hundsberger, H. G. Mergenthaler, C. Junghanss, T. Birnbaum, L. Fischer, K. Jahnke, U. Herrlinger, P. Roth, M. Bamberg, T. Pietsch, and M. Weller. 2015. 'Randomized phase III study of whole-brain radiotherapy for primary CNS lymphoma', *Neurology*, 84: 1242-8.

Kowolik, C. M., M. S. Topp, S. Gonzalez, T. Pfeiffer, S. Olivares, N. Gonzalez, D. D. Smith, S. J. Forman, M. C. Jensen, and L. J. Cooper. 2006. 'CD28 costimulation provided through a CD19-specific chimeric antigen receptor enhances in vivo persistence and antitumor efficacy of adoptively transferred T cells', *Cancer Res*, 66: 10995-1004.

Krummel, M. F., F. Bartumeus, and A. Gerard. 2016. 'T cell migration, search strategies and mechanisms', *Nat Rev Immunol*, 16: 193-201.

Kuker, W., T. Nagele, A. Korfel, S. Heckl, E. Thiel, M. Bamberg, M. Weller, and U. Herrlinger. 2005. 'Primary central nervous system lymphomas (PCNSL): MRI features at presentation in 100 patients', *J Neurooncol*, 72: 169-77.

Kuwana, Y., Y. Asakura, N. Utsunomiya, M. Nakanishi, Y. Arata, S. Itoh, F. Nagase, and Y. Kurosawa. 1987. 'Expression of chimeric receptor composed of

immunoglobulin-derived V regions and T-cell receptor-derived C regions', *Biochem Biophys Res Commun*, 149: 960-8.

Lai, R., M. K. Rosenblum, and L. M. DeAngelis. 2002. 'Primary CNS lymphoma: a whole-brain disease?', *Neurology*, 59: 1557-62.

Lee, D. W., R. Gardner, D. L. Porter, C. U. Louis, N. Ahmed, M. Jensen, S. A. Grupp, and C. L. Mackall. 2014. 'Current concepts in the diagnosis and management of cytokine release syndrome', *Blood*, 124: 188-95.

Lee, D. W., J. N. Kochenderfer, M. Stetler-Stevenson, Y. K. Cui, C. Delbrook, S. A. Feldman, T. J. Fry, R. Orentas, M. Sabatino, N. N. Shah, S. M. Steinberg, D. Stroncek, N. Tschernia, C. Yuan, H. Zhang, L. Zhang, S. A. Rosenberg, A. S. Wayne, and C. L. Mackall. 2015. 'T cells expressing CD19 chimeric antigen receptors for acute lymphoblastic leukaemia in children and young adults: a phase 1 dose-escalation trial', *Lancet*, 385: 517-28.

Legrand, C., J. M. Bour, C. Jacob, J. Capiaumont, A. Martial, A. Marc, M. Wudtke, G. Kretzmer, C. Demangel, D. Duval, and et al. 1992. 'Lactate dehydrogenase (LDH) activity of the cultured eukaryotic cells as marker of the number of dead cells in the medium [corrected]', *J Biotechnol*, 25: 231-43.

Louveau, A., I. Smirnov, T. J. Keyes, J. D. Eccles, S. J. Rouhani, J. D. Peske, N. C. Derecki, D. Castle, J. W. Mandell, K. S. Lee, T. H. Harris, and J. Kipnis. 2015. 'Structural and functional features of central nervous system lymphatic vessels', *Nature*, 523: 337-41.

Maher, J., R. J. Brentjens, G. Gunset, I. Riviere, and M. Sadelain. 2002. 'Human T-lymphocyte cytotoxicity and proliferation directed by a single chimeric TCRzeta /CD28 receptor', *Nat Biotechnol*, 20: 70-5.

Mandigers, C. M., L. F. Verdonck, J. P. Meijerink, A. W. Dekker, A. V. Schattenberg, and J. M. Raemaekers. 2003. 'Graft-versus-lymphoma effect of donor lymphocyte infusion in indolent lymphomas relapsed after allogeneic stem cell transplantation', *Bone Marrow Transplant*, 32: 1159-63.

Markiewski, M. M., R. A. DeAngelis, F. Benencia, S. K. Ricklin-Lichtsteiner, A. Koutoulaki, C. Gerard, G. Coukos, and J. D. Lambris. 2008. 'Modulation of the antitumor immune response by complement', *Nat Immunol*, 9: 1225-35.

Maude, S. L., N. Frey, P. A. Shaw, R. Aplenc, D. M. Barrett, N. J. Bunin, A. Chew, V. E. Gonzalez, Z. Zheng, S. F. Lacey, Y. D. Mahnke, J. J. Melenhorst, S. R. Rheingold, A. Shen, D. T. Teachey, B. L. Levine, C. H. June, D. L. Porter, and S. A. Grupp. 2014. 'Chimeric antigen receptor T cells for sustained remissions in leukemia', *N Engl J Med*, 371: 1507-17.

Maus, M. V., S. A. Grupp, D. L. Porter, and C. H. June. 2014. 'Antibody-modified T cells: CARs take the front seat for hematologic malignancies', *Blood*, 123: 2625-35.

Mineo, J. F., A. Scheffer, C. Karkoutly, L. Nouvel, O. Kerdraon, J. Trauet, A. Bordron, J. P. Dessaint, M. Labalette, C. Berthou, and P. Labalette. 2008. 'Using human CD20-transfected murine lymphomatous B cells to evaluate the efficacy of intravitreal and intracerebral rituximab injections in mice', *Invest Ophthalmol Vis Sci*, 49: 4738-45.

Misgeld, T., and M. Kerschensteiner. 2006. 'In vivo imaging of the diseased nervous system', *Nat Rev Neurosci*, 7: 449-63.

Mizuguchi, H., Z. Xu, A. Ishii-Watabe, E. Uchida, and T. Hayakawa. 2000. 'IRES-dependent second gene expression is significantly lower than cap-dependent first gene expression in a bicistronic vector', *Mol Ther*, 1: 376-82.

Montesinos-Rongen, M., M. Sanchez-Ruiz, A. Brunn, K. Hong, S. Bens, S. R. Perales, J. C. Cigudosa, R. Siebert, and M. Deckert. 2013. 'Mechanisms of intracerebral lymphoma growth delineated in a syngeneic mouse model of central nervous system lymphoma', *J Neuropathol Exp Neurol*, 72: 325-36.

Morris, P. G., D. D. Correa, J. Yahalom, J. J. Raizer, D. Schiff, B. Grant, S. Grimm, R. K. Lai, A. S. Reiner, K. Panageas, S. Karimi, R. Curry, G. Shah, L. E. Abrey, L. M. DeAngelis, and A. Omuro. 2013. 'Rituximab, methotrexate, procarbazine, and vincristine followed by consolidation reduced-dose whole-brain radiotherapy and cytarabine in newly diagnosed primary CNS lymphoma: final results and long-term outcome', *J Clin Oncol*, 31: 3971-9.

Muldoon, L. L., S. J. Lewin, E. Dosa, D. F. Kraemer, M. A. Pagel, N. D. Doolittle, and E. A. Neuwelt. 2011. 'Imaging and therapy with rituximab anti-CD20 immunotherapy in an animal model of central nervous system lymphoma', *Clin Cancer Res*, 17: 2207-15.

Murray, K., L. Kun, and J. Cox. 1986. 'Primary malignant lymphoma of the central nervous system. Results of treatment of 11 cases and review of the literature', *J Neurosurg*, 65: 600-7.

Newick, K., E. Moon, and S. M. Albelda. 2016. 'Chimeric antigen receptor T-cell therapy for solid tumors', *Mol Ther Oncolytics*, 3: 16006.

Newick, K., S. O'Brien, E. Moon, and S. M. Albelda. 2017. 'CAR T Cell Therapy for Solid Tumors', *Annu Rev Med*, 68: 139-52.

Nicholson, I. C., K. A. Lenton, D. J. Little, T. Decorso, F. T. Lee, A. M. Scott, H. Zola, and A. W. Hohmann. 1997. 'Construction and characterisation of a functional CD19 specific single chain Fv fragment for immunotherapy of B lineage leukaemia and lymphoma', *Mol Immunol*, 34: 1157-65.

Nicolas-Virelizier, Emmanuelle, Philippe Rey, Francois Ducray, Emmanuel Jouanneau, Pierre Faurie, Amine Belhabri, Marie Pierre Sunyach, Catherine Chassagne-Clement, Philippe Thiesse, Catherine Sebban, Pierre Biron, Jean-Yves Blay, and Herve Ghesquieres. 2013. 'Utility Of Post Therapy Brain Surveillance Imaging In The Detection Of Primary CNS Lymphoma (PCNSL) Relapse', *Blood*, 122: 933-33.

O'Rourke, Donald M., MacLean Nasrallah, Jennifer J. Morrissette, Jan J. Melenhorst, Simon F. Lacey, Keith Mansfield, Maria Martinez-Lage, Arati Suvas Desai, Steven Brem, Eileen Maloney, Suyash Mohan, Sumei Wang, Gaurav Verma, Jean-Marc Navenot, Angela Shen, Zhaohui Zheng, Bruce Levine, Hideho Okada, Carl H. June, and Marcela Valderrama Maus. 2016. 'Pilot study of T cells redirected to EGFRvIII with a chimeric antigen receptor in patients with EGFRvIII+ glioblastoma', *Journal of Clinical Oncology*, 34: 2067-67.

Okabe, M., M. Ikawa, K. Kominami, T. Nakanishi, and Y. Nishimune. 1997. "Green mice' as a source of ubiquitous green cells', *FEBS Lett*, 407: 313-9.

Omuro, A. M., L. S. Ben-Porat, K. S. Panageas, A. K. Kim, D. D. Correa, J. Yahalom, L. M. Deangelis, and L. E. Abrey. 2005. 'Delayed neurotoxicity in primary central nervous system lymphoma', *Arch Neurol*, 62: 1595-600.

Omuro, A. M., L. M. DeAngelis, J. Yahalom, and L. E. Abrey. 2005. 'Chemoradiotherapy for primary CNS lymphoma: an intent-to-treat analysis with complete follow-up', *Neurology*, 64: 69-74.

Osswald, M., E. Jung, F. Sahm, G. Solecki, V. Venkataramani, J. Blaes, S. Weil, H. Horstmann, B. Wiestler, M. Syed, L. Huang, M. Ratliff, K. Karimian Jazi, F. T. Kurz, T. Schmenger, D. Lemke, M. Gommel, M. Pauli, Y. Liao, P. Haring, S. Pusch, V. Herl, C. Steinhauser, D. Krunic, M. Jarahian, H. Miletic, A. S. Berghoff, O. Griesbeck, G. Kalamakis, O. Garaschuk, M. Preusser, S. Weiss, H. Liu, S. Heiland, M. Platten, P. E. Huber, T. Kuner, A. von Deimling, W. Wick, and F. Winkler. 2015. 'Brain tumour cells interconnect to a functional and resistant network', *Nature*, 528: 93-8.

Ostrom, Q. T., H. Gittleman, J. Fulop, M. Liu, R. Blanda, C. Kromer, Y. Wolinsky, C. Kruchko, and J. S. Barnholtz-Sloan. 2015. 'CBTRUS Statistical Report: Primary Brain and Central Nervous System Tumors Diagnosed in the United States in 2008-2012', *Neuro Oncol*, 17 Suppl 4: iv1-iv62.

Ousman, S. S., and P. Kubes. 2012. 'Immune surveillance in the central nervous system', *Nat Neurosci*, 15: 1096-101.

Page, D. B., M. A. Postow, M. K. Callahan, J. P. Allison, and J. D. Wolchok. 2014. 'Immune modulation in cancer with antibodies', *Annu Rev Med*, 65: 185-202.

Paget, S. 1889. 'The distribution of secondary growths in cancer of the breast.', *Lancet*, 133: 571-73.

Pantelouris, E. M. 1968. 'Absence of thymus in a mouse mutant', *Nature*, 217: 370-1.

Paszkiewicz, P. J., S. P. Frassle, S. Srivastava, D. Sommermeyer, M. Hudecek, I. Drexler, M. Sadelain, L. Liu, M. C. Jensen, S. R. Riddell, and D. H. Busch. 2016. 'Targeted antibody-mediated depletion of murine CD19 CAR T cells permanently reverses B cell aplasia', *J Clin Invest*, 126: 4262-72.

Pelletier, J., and N. Sonenberg. 1988. 'Internal initiation of translation of eukaryotic mRNA directed by a sequence derived from poliovirus RNA', *Nature*, 334: 320-5.

Perez-Alvarez, A., A. Araque, and E. D. Martin. 2013. 'Confocal microscopy for astrocyte in vivo imaging: Recycle and reuse in microscopy', *Front Cell Neurosci*, 7: 51.

Porter, D. L., W. T. Hwang, N. V. Frey, S. F. Lacey, P. A. Shaw, A. W. Loren, A. Bagg, K. T. Marcucci, A. Shen, V. Gonzalez, D. Ambrose, S. A. Grupp, A. Chew, Z. Zheng, M. C. Milone, B. L. Levine, J. J. Melenhorst, and C. H. June. 2015. 'Chimeric antigen receptor T cells persist and induce sustained remissions in relapsed refractory chronic lymphocytic leukemia', *Sci Transl Med*, 7: 303ra139.

Porter, D. L., B. L. Levine, M. Kalos, A. Bagg, and C. H. June. 2011. 'Chimeric antigen receptor-modified T cells in chronic lymphoid leukemia', *N Engl J Med*, 365: 725-33.

Power, D. 1895. 'The Infectivity of Cancer: A Retrospect and a Forecast', *Br Med J*, 1: 910-2.

Qi, S., H. Li, L. Lu, Z. Qi, L. Liu, L. Chen, G. Shen, L. Fu, Q. Luo, and Z. Zhang. 2016. 'Long-term intravital imaging of the multicolor-coded tumor microenvironment during combination immunotherapy', *Elife*, 5.

Quentmeier, H., R. M. Amini, M. Berglund, W. G. Dirks, S. Ehrentraut, R. Geffers, R. A. Macleod, S. Nagel, J. Romani, M. Scherr, M. Zaborski, and H. G. Drexler. 2013. 'U-2932: two clones in one cell line, a tool for the study of clonal evolution', *Leukemia*, 27: 1155-64.

Ramamonjisoa, N., and E. Ackerstaff. 2017. 'Characterization of the Tumor Microenvironment and Tumor-Stroma Interaction by Non-invasive Preclinical Imaging', *Front Oncol*, 7: 3.

Ricard, C., and F. C. Debarbieux. 2014. 'Six-color intravital two-photon imaging of brain tumors and their dynamic microenvironment', *Front Cell Neurosci*, 8: 57.

Rizvi, N. A., J. Mazieres, D. Planchard, T. E. Stinchcombe, G. K. Dy, S. J. Antonia, L. Horn, H. Lena, E. Minenza, B. Mennecier, G. A. Otterson, L. T. Campos, D. R. Gandara, B. P. Levy, S. G. Nair, G. Zalcman, J. Wolf, P. J. Souquet, E. Baldini, F. Cappuzzo, C. Chouaid, A. Dowlati, R. Sanborn, A. Lopez-Chavez, C. Grohe, R. M.

Huber, C. T. Harbison, C. Baudelet, B. J. Lestini, and S. S. Ramalingam. 2015. 'Activity and safety of nivolumab, an anti-PD-1 immune checkpoint inhibitor, for patients with advanced, refractory squamous non-small-cell lung cancer (CheckMate 063): a phase 2, single-arm trial', *Lancet Oncol*, 16: 257-65.

Roybal, K. T., L. J. Rupp, L. Morsut, W. J. Walker, K. A. McNally, J. S. Park, and W. A. Lim. 2016. 'Precision Tumor Recognition by T Cells With Combinatorial Antigen-Sensing Circuits', *Cell*, 164: 770-9.

Rubenstein, J. L., N. K. Gupta, G. N. Mannis, A. K. Lamarre, and P. Treseler. 2013. 'How I treat CNS lymphomas', *Blood*, 122: 2318-30.

Rubenstein, J. L., E. D. Hsi, J. L. Johnson, S. H. Jung, M. O. Nakashima, B. Grant, B. D. Cheson, and L. D. Kaplan. 2013. 'Intensive chemotherapy and immunotherapy in patients with newly diagnosed primary CNS lymphoma: CALGB 50202 (Alliance 50202)', *J Clin Oncol*, 31: 3061-8.

Rubenstein, J. L., P. Treseler, and J. M. O'Brien. 2005. 'Pathology and genetics of primary central nervous system and intraocular lymphoma', *Hematol Oncol Clin North Am*, 19: 705-17, vii.

Ruella, M., D. M. Barrett, S. S. Kenderian, O. Shestova, T. J. Hofmann, J. Perazzelli, M. Klichinsky, V. Aikawa, F. Nazimuddin, M. Kozlowski, J. Scholler, S. F. Lacey, J. J. Melenhorst, J. J. Morrissette, D. A. Christian, C. A. Hunter, M. Kalos, D. L. Porter, C. H. June, S. A. Grupp, and S. Gill. 2016. 'Dual CD19 and CD123 targeting prevents antigen-loss relapses after CD19-directed immunotherapies', *J Clin Invest*, 126: 3814-26.

Ruella, M., and M. V. Maus. 2016. 'Catch me if you can: Leukemia Escape after CD19-Directed T Cell Immunotherapies', *Comput Struct Biotechnol J*, 14: 357-62.

Sadelain, M. 2015. 'CAR therapy: the CD19 paradigm', *J Clin Invest*, 125: 3392-400.

Sadelain, M., R. Brentjens, and I. Riviere. 2013. 'The basic principles of chimeric antigen receptor design', *Cancer Discov*, 3: 388-98.

Sagerman, R. H., C. H. Collier, and G. A. King. 1983. 'Radiation therapy of microgliomas', *Radiology*, 149: 567-70.

Santos, E. B., R. Yeh, J. Lee, Y. Nikhamin, B. Punzalan, B. Punzalan, K. La Perle, S. M. Larson, M. Sadelain, and R. J. Brentjens. 2009. 'Sensitive in vivo imaging of T cells using a membrane-bound Gaussia princeps luciferase', *Nat Med*, 15: 338-44.

Savoldo, B., C. A. Ramos, E. Liu, M. P. Mims, M. J. Keating, G. Carrum, R. T. Kamble, C. M. Bollard, A. P. Gee, Z. Mei, H. Liu, B. Grilley, C. M. Rooney, H. E. Heslop, M. K. Brenner, and G. Dotti. 2011. 'CD28 costimulation improves expansion and persistence of chimeric antigen receptor-modified T cells in lymphoma patients', *J Clin Invest*, 121: 1822-6.

Schabet, M. 1999. 'Epidemiology of primary CNS lymphoma', *J Neurooncol*, 43: 199-201.

Scheiff, J. M., A. C. Cordier, and S. Haumont. 1978. 'The thymus of Nu/+ mice', *Anat Embryol (Berl)*, 153: 115-22.

Schlager, C., H. Korner, M. Krueger, S. Vidoli, M. Haberl, D. Mielke, E. Brylla, T. Issekutz, C. Cabanas, P. J. Nelson, T. Ziemssen, V. Rohde, I. Bechmann, D. Lodygin, F. Odoardi, and A. Flugel. 2016. 'Effector T-cell trafficking between the leptomeninges and the cerebrospinal fluid', *Nature*, 530: 349-53.

Schmid, D. A., M. B. Irving, V. Posevitz, M. Hebeisen, A. Posevitz-Fejfar, J. C. Sarria, R. Gomez-Eerland, M. Thome, T. N. Schumacher, P. Romero, D. E. Speiser, V. Zoete, O. Michielin, and N. Rufer. 2010. 'Evidence for a TCR affinity threshold delimiting maximal CD8 T cell function', *J Immunol*, 184: 4936-46.

Schorb, E., B. Kasenda, J. Atta, S. Kaun, A. Morgner, G. Hess, T. Elter, N. von Bubnoff, M. Dreyling, M. Ringhoffer, S. W. Krause, G. Derigs, B. Klimm, D. Niemann, K. Fritsch, J. Finke, and G. Illerhaus. 2013. 'Prognosis of patients with primary central nervous system lymphoma after high-dose chemotherapy followed by autologous stem cell transplantation', *Haematologica*, 98: 765-70.

Scott, A. M., J. D. Wolchok, and L. J. Old. 2012. 'Antibody therapy of cancer', *Nat Rev Cancer*, 12: 278-87.

Shah, G. D., J. Yahalom, D. D. Correa, R. K. Lai, J. J. Raizer, D. Schiff, R. LaRocca, B. Grant, L. M. DeAngelis, and L. E. Abrey. 2007. 'Combined immunochemotherapy with reduced whole-brain radiotherapy for newly diagnosed primary CNS lymphoma', *J Clin Oncol*, 25: 4730-5.

Shiels, M. S., R. M. Pfeiffer, C. Besson, C. A. Clarke, L. M. Morton, L. Nogueira, K. Pawlish, E. L. Yanik, G. Suneja, and E. A. Engels. 2016. 'Trends in primary central nervous system lymphoma incidence and survival in the U.S', *Br J Haematol*, 174: 417-24.

Sotillo, E., D. M. Barrett, K. L. Black, A. Bagashev, D. Oldridge, G. Wu, R. Sussman, C. Lanauze, M. Ruella, M. R. Gazzara, N. M. Martinez, C. T. Harrington, E. Y. Chung, J. Perazzelli, T. J. Hofmann, S. L. Maude, P. Raman, A. Barrera, S. Gill, S. F. Lacey, J. J. Melenhorst, D. Allman, E. Jacoby, T. Fry, C. Mackall, Y. Barash, K. W. Lynch, J. M. Maris, S. A. Grupp, and A. Thomas-Tikhonenko. 2015. 'Convergence of Acquired Mutations and Alternative Splicing of CD19 Enables Resistance to CART-19 Immunotherapy', *Cancer Discov*, 5: 1282-95.

Soussain, C., S. Choquet, E. Fourme, D. Delgadillo, K. Bouabdallah, H. Ghesquieres, G. Damaj, B. Dupriez, J. Vargaftig, A. Gonzalez, C. Houillier, L. Taillandier, K. Hoang-Xuan, and V. Leblond. 2012. 'Intensive chemotherapy with thiotepa, busulfan and cyclophosphamide and hematopoietic stem cell rescue in relapsed or refractory

primary central nervous system lymphoma and intraocular lymphoma: a retrospective study of 79 cases', *Haematologica*, 97: 1751-6.

Thiel, E., A. Korfel, P. Martus, L. Kanz, F. Griesinger, M. Rauch, A. Roth, B. Hertenstein, T. von Toll, T. Hundsberger, H. G. Mergenthaler, M. Leithauser, T. Birnbaum, L. Fischer, K. Jahnke, U. Herrlinger, L. Plasswilm, T. Nagele, T. Pietsch, M. Bamberg, and M. Weller. 2010. 'High-dose methotrexate with or without whole brain radiotherapy for primary CNS lymphoma (G-PCNSL-SG-1): a phase 3, randomised, non-inferiority trial', *Lancet Oncol*, 11: 1036-47.

Tomayko, M. M., and C. P. Reynolds. 1989. 'Determination of subcutaneous tumor size in athymic (nude) mice', *Cancer Chemother Pharmacol*, 24: 148-54.

Torcellan, T., J. Stolp, and T. Chtanova. 2017. 'In Vivo Imaging Sheds Light on Immune Cell Migration and Function in Cancer', *Front Immunol*, 8: 309.

Tsukahara, T., K. Ohmine, C. Yamamoto, R. Uchibori, H. Ido, T. Teruya, M. Urabe, H. Mizukami, A. Kume, M. Nakamura, J. Mineno, K. Takesako, I. Riviere, M. Sadelain, R. Brentjens, and K. Ozawa. 2013. 'CD19 target-engineered T-cells accumulate at tumor lesions in human B-cell lymphoma xenograft mouse models', *Biochem Biophys Res Commun*, 438: 84-9.

Tumeh, P. C., C. L. Harview, J. H. Yearley, I. P. Shintaku, E. J. Taylor, L. Robert, B. Chmielowski, M. Spasic, G. Henry, V. Ciobanu, A. N. West, M. Carmona, C. Kivork, E. Seja, G. Cherry, A. J. Gutierrez, T. R. Grogan, C. Mateus, G. Tomasic, J. A. Glaspy, R. O. Emerson, H. Robins, R. H. Pierce, D. A. Elashoff, C. Robert, and A. Ribas. 2014. 'PD-1 blockade induces responses by inhibiting adaptive immune resistance', *Nature*, 515: 568-71.

van der Stegen, S. J., D. M. Davies, S. Wilkie, J. Foster, J. K. Sosabowski, J. Burnet, L. M. Whilding, R. M. Petrovic, S. Ghaem-Maghami, S. Mather, J. P. Jeannon, A. C. Parente-Pereira, and J. Maher. 2013. 'Preclinical in vivo modeling of cytokine release syndrome induced by ErbB-retargeted human T cells: identifying a window of therapeutic opportunity?', *J Immunol*, 191: 4589-98.

Villano, J. L., M. Koshy, H. Shaikh, T. A. Dolecek, and B. J. McCarthy. 2011. 'Age, gender, and racial differences in incidence and survival in primary CNS lymphoma', *Br J Cancer*, 105: 1414-8.

von Baumgarten, L., D. Brucker, A. Tirniceru, Y. Kienast, S. Grau, S. Burgold, J. Herms, and F. Winkler. 2011. 'Bevacizumab has differential and dose-dependent effects on glioma blood vessels and tumor cells', *Clin Cancer Res*, 17: 6192-205.

Walter, S., T. Weinschenk, A. Stenzl, R. Zdrojowy, A. Pluzanska, C. Szczylik, M. Staehler, W. Brugger, P. Y. Dietrich, R. Mendrzyk, N. Hilf, O. Schoor, J. Fritsche, A. Mahr, D. Maurer, V. Vass, C. Trautwein, P. Lewandrowski, C. Flohr, H. Pohla, J. J.

Stanczak, V. Bronte, S. Mandruzzato, T. Biedermann, G. Pawelec, E. Derhovanessian, H. Yamagishi, T. Miki, F. Hongo, N. Takaha, K. Hirakawa, H. Tanaka, S. Stevanovic, J. Frisch, A. Mayer-Mokler, A. Kirner, H. G. Rammensee, C. Reinhardt, and H. Singh-Jasuja. 2012. 'Multipeptide immune response to cancer vaccine IMA901 after single-dose cyclophosphamide associates with longer patient survival', *Nat Med*, 18: 1254-61.

Wang, X., W. C. Chang, C. W. Wong, D. Colcher, M. Sherman, J. R. Ostberg, S. J. Forman, S. R. Riddell, and M. C. Jensen. 2011. 'A transgene-encoded cell surface polypeptide for selection, in vivo tracking, and ablation of engineered cells', *Blood*, 118: 1255-63.

Weller, M., P. Martus, P. Roth, E. Thiel, A. Korfel, and Pcnsl Study Group German. 2012. 'Surgery for primary CNS lymphoma? Challenging a paradigm', *Neuro Oncol*, 14: 1481-4.

Wortis, H. H., S. Nehlsen, and J. J. Owen. 1971. 'Abnormal development of the thymus in "nude" mice', *J Exp Med*, 134: 681-92.

Yeku, O., X. Li, and R. J. Brentjens. 2017. 'Adoptive T-Cell Therapy for Solid Tumors', *Am Soc Clin Oncol Educ Book*, 37: 193-204.

Yong, C. S. M., V. Dardalhon, C. Devaud, N. Taylor, P. K. Darcy, and M. H. Kershaw. 2017. 'CAR T-cell therapy of solid tumors', *Immunol Cell Biol*, 95: 356-63.

Yu, P., D. A. Rowley, Y. X. Fu, and H. Schreiber. 2006. 'The role of stroma in immune recognition and destruction of well-established solid tumors', *Curr Opin Immunol*, 18: 226-31.

Zal, T., and G. Chodaczek. 2010. 'Intravital imaging of anti-tumor immune response and the tumor microenvironment', *Semin Immunopathol*, 32: 305-17.

Zhang, G., V. Gurtu, and S. R. Kain. 1996. 'An enhanced green fluorescent protein allows sensitive detection of gene transfer in mammalian cells', *Biochem Biophys Res Commun*, 227: 707-11.

Zhao, Z., M. Condomines, S. J. van der Stegen, F. Perna, C. C. Kloss, G. Gunset, J. Plotkin, and M. Sadelain. 2015. 'Structural Design of Engineered Costimulation Determines Tumor Rejection Kinetics and Persistence of CAR T Cells', *Cancer Cell*, 28: 415-28.

Zuklys, S., A. Handel, S. Zhanybekova, F. Govani, M. Keller, S. Maio, C. E. Mayer, H. Y. Teh, K. Hafen, G. Gallone, T. Barthlott, C. P. Ponting, and G. A. Hollander. 2016. 'Foxn1 regulates key target genes essential for T cell development in postnatal thymic epithelial cells', *Nat Immunol*, 17: 1206-15.

10 Publications & conference presentation

Publications

Features of human CD3+ CD20+ T cells.
E. Schuh, K. Berer, **M. Mulazzani**, K. Feil, I. Meinl, H. Lahm, M. Krane, R. Lange, K. Pfannes, M. Subklewe, R. Gürkov, M. Bradl, R. Hohlfeld, T. Kümpfel, E. Meinl, M. Krumbholz. *J Immunol*, 2016

Soluble TACI and soluble BCMA as biomarkers in primary central nervous system lymphoma.
F. Thaler, S. Laurent, M. Huber, **M. Mulazzani**, M. Dreyling, U. Ködel, T. Kümpfel, A. Straube, E. Meinl, L. von Baumgarten. *Neuro Oncol*, 2017

APRIL and BAFF are diagnostic biomarkers in central nervous system lymphoma.
M. Huber, S. Borchard, **M. Mulazzani**, S. Langer, B. Angele, E. Schuh, E. Meinl, M. Dreyling, A. Straube, U. Ködel, L. von Baumgarten. Submitted.

Intravital microscopy reveals complete regression of large, established CNS lymphoma after intracerebral 1928z CAR T cell injection.
M. Mulazzani, S. Fräßle, V. Buchholz, A. Straube, D. Busch, L. von Baumgarten. Manuscript in preparation.

Conference Presentation

Chimeric antigen receptor T cells targeting primary CNS lymphoma: Visualizing the anti-tumor response *in vivo*
M. Mulazzani, S. Fräßle, V. Buchholz, A. Straube, D. Busch, L. von Baumgarten
AACR Special Conference on Tumor Immunology and Immunotherapy; October 20-23, 2016; Boston, USA